



An International ICT R&D Journal Sponsored by ZTE Corporation

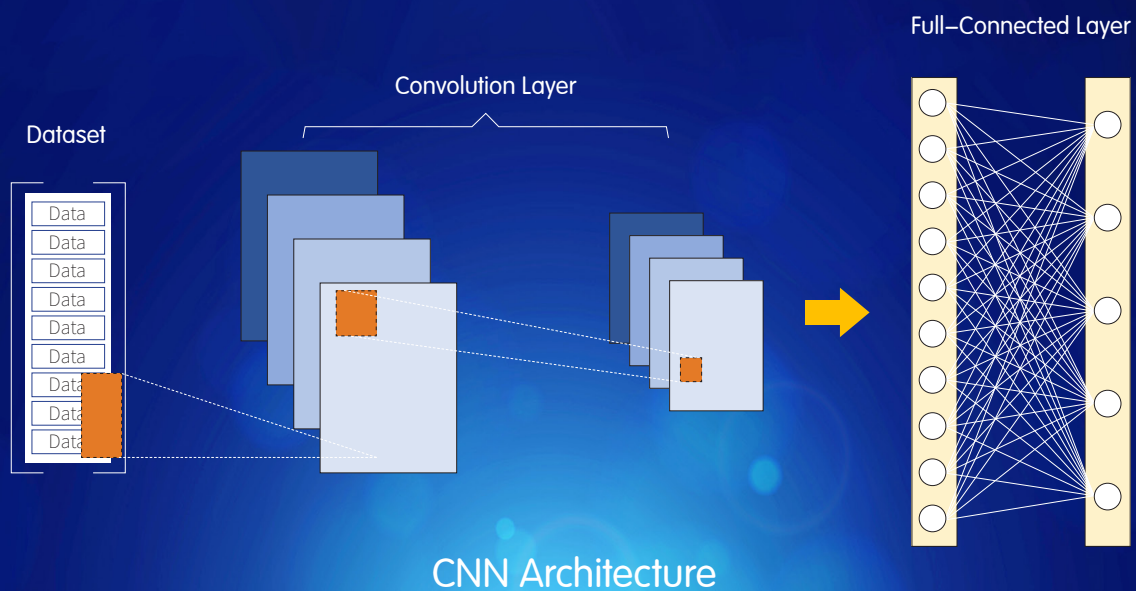
ISSN 1673-5188

CN 34-1294/TN

ZTE COMMUNICATIONS

中兴通讯技术(英文版)

January 2022, Vol. 20 Supplement 1



The 9th Editorial Board of ZTE Communications

Chairman	GAO Wen , Peking University (China)
Vice Chairmen	XU Ziyang , ZTE Corporation (China) XU Chengzhong , University of Macau (China)

Members (Surname in Alphabetical Order)

AI Bo	Beijing Jiaotong University (China)
CAO Jiannong	Hong Kong Polytechnic University (China)
CHEN Chang Wen	The State University of New York at Buffalo (USA)
CHEN Yan	Northwestern University (USA)
CHI Nan	Fudan University (China)
CUI Shuguang	UC Davis (USA) and The Chinese University of Hong Kong, Shenzhen (China)
GAO Wen	Peking University (China)
GAO Yang	Nanjing University (China)
GE Xiaohu	Huazhong University of Science and Technology (China)
HWANG Jenq-Neng	University of Washington (USA)
Victor C. M. LEUNG	The University of British Columbia (Canada)
LI Xiangyang	University of Science and Technology of China (China)
LI Zixue	ZTE Corporation (China)
LIAO Yong	Chongqing University (China)
LIN Xiaodong	ZTE Corporation (China)
LIU Chi	Beijing Institute of Technology (China)
LIU Jian	ZTE Corporation (China)
LIU Yue	Beijing Institute of Technology (China)
MA Jianhua	Hosei University (Japan)
MA Zheng	Southwest Jiaotong University (China)
PAN Yi	Shenzhen Institute of Advanced Technology, Chinese Academy of Sciences (China)
PENG Mugen	Beijing University of Posts and Telecommunications (China)
REN Fuji	Tokushima University (Japan)
REN Kui	Zhejiang University (China)
SHENG Min	Xidian University (China)
SU Zhou	Xi'an Jiaotong University (China)
SUN Huifang	Mitsubishi Electric Research Laboratories (USA)
SUN Zhili	University of Surrey (UK)
TAO Meixia	Shanghai Jiao Tong University (China)
WANG Haiming	Southeast University (China)
WANG Xiang	ZTE Corporation (China)
WANG Xiaodong	Columbia University (USA)
WANG Xiyu	ZTE Corporation (China)
WANG Yongjin	Nanjing University of Posts and Telecommunications (China)
XU Chengzhong	University of Macau (China)
XU Ziyang	ZTE Corporation (China)
YANG Kun	University of Essex (UK)
YUAN Jinhong	University of New South Wales (Australia)
ZENG Wenjun	EIT Institute for Advanced Study (China)
ZHANG Honggang	Zhejiang University (China)
ZHANG Jianhua	Beijing University of Posts and Telecommunications (China)
ZHANG Yueping	Nanyang Technological University (Singapore)
ZHOU Wanlei	City University of Macau (China)
ZHUANG Weihua	University of Waterloo (Canada)

CONTENTS

ZTE COMMUNICATIONS January 2022 Vol. 20 Supplement 1 (Issue 77)

Research Paper

An Improved Parasitic Parameter Extraction Method for InP HEMT 01

An improved parasitic parameter extraction method for InP HEMT is presented. In order to obtain higher accuracy of parasitic parameters, parasitic parameters are extracted in this paper based on traditional analytical method and optimization algorithm to obtain the best parasitic parameters. The validity of the proposed parasitic parameter extraction method has been verified with excellent agreement between the measured and modeled S -parameters up to 40 GHz for InP HEMT. The extraction of parasitic parameters not only provides a foundation for the high-precision extraction of small signal intrinsic parameters of HEMT devices, but also lays a foundation for the high-precision extraction of equivalent circuit model parameters of large signal and noise signals of HEMT devices.

DUAN Lanyan, LU Hongliang, QI Junjun, ZHANG Yuming,
ZHANG Yimen

Auxiliary Fault Location on Commercial Equipment Based on Supervised Machine Learning 07

The authors introduce supervised machine learning to propose a complete process for fault location. Firstly, they use data preprocessing, data annotation, and data augmentation in order to process original collected data to build a high-quality dataset. Then, two machine learning algorithms are applied on the dataset. The evaluation on commercial optical networks shows that this process helps improve the quality of dataset, and two algorithms perform well on fault location.

ZHAO Zipiao, ZHAO Yongli, YAN Boyuan, WANG Dajiang

Design of Raptor-Like Rate Compatible SC-LDPC Codes 16

This paper proposes a family of RL-RC-SC-LDPC codes from RL-RC-LDPC block codes. There are two important keys. One is the perfor-

mance of the base matrix. The other is the edge coupling design. The authors have designed a rate-compatible coupling algorithm, which can improve performance under multiple code rates. The constructed RL-RC-SC-LDPC code property requires a large coupling length L and thus we improved the reciprocal channel approximation (RCA) algorithm and proposed a sliding window RCA algorithm. It can provide lower complexity and latency than RCA algorithm. The code family shows improved thresholds close to the Shannon limit and finite-length performance compared with 5G NR LDPC codes for AWGN channel.

SHI Xiangyi, HAN Tongzhou, TIAN Hai, ZHAO Danfeng

22 Derivative-Based Envelope Design Technique for Wideband Envelope Tracking Power Amplifier with Digital Predistortion

A novel envelope design for an ET PA based on its derivatives is proposed, which can trade well off between bandwidth reduction and tracking accuracy. This paper theoretically analyzes how to choose an envelope design that can track the original envelope closely and reduce its bandwidth, and then demonstrates an example to validate this idea. The GMP model is applied to compensate for the nonlinearity of ET PA with the proposed envelope design. Experiments are carried out on an ET system that is operated with the center frequency of 3.5 GHz and excited by a 20 MHz LTE signal, which show that the proposed envelope design can make a good trade-off between envelope bandwidth and efficiency, and satisfactory linearization performance can be realized.

YI Xueya, CHEN Jixin, CHEN Peng, NING Dongfang, YU Chao

27 End-to-End Chinese Entity Recognition Based on BERT-BiLSTM-ATT-CRF

The authors propose a Chinese named entity recognition method based on the BERT-BiLSTM-ATT-CRF model. Firstly, they use the bidirectional encoder representations from transformers (BERT) pretraining language model to obtain the semantic vector of the word according to the context information of the word; Secondly, the word vectors trained by BERT are input into the BiLSTM-ATT to capture the most important semantic information in the sentence; Finally, the CRF is used to learn the dependence between adjacent tags to obtain the global optimal sen-

Submission of a manuscript implies that the submitted work has not been published before (except as part of a thesis or lecture note or report or in the form of an abstract); that it is not under consideration for publication elsewhere; that its publication has been approved by all co-authors as well as by the authorities at the institute where the work has been carried out; that, if and when the manuscript is accepted for publication, the authors hand over the transferable copyrights of the accepted manuscript to *ZTE Communications*; and that the manuscript or parts thereof will not be published elsewhere in any language without the consent of the copyright holder. Copyrights include, without spatial or timely limitation, the mechanical, electronic and visual reproduction and distribution; electronic storage and retrieval; and all other forms of electronic publication or any other types of publication including all subsidiary rights.

Responsibility for content rests on authors of signed articles and not on the editorial board of *ZTE Communications* or its sponsors.

All rights reserved.

CONTENTS

ZTE COMMUNICATIONS January 2022 Vol. 20 Supplement 1 (Issue 77)

tence level tag sequence. The experimental results show that the proposed model achieves state-of-the-art performance on both MSRA corpus and people's daily corpus, with F1 values of 94.77% and 95.97% respectively.

LI Daiyi, TU Yaofeng, ZHOU Xiangsheng, ZHANG Yangming, MA Zongmin

Intelligent Antenna Attitude Parameters Measurement Based on Deep Learning SSD Model 36

This paper introduces a deep learning model for the antenna attitude parameters measurement, which can be divided into an antenna location phase and a calculation phase of the attitude parameter. In the first phase, an SSD is applied to automatically recognize and discover the antenna from pictures taken by drones. In the second phase, the located antennas' feature lines are extracted and their attitude parameters are then calculated mathematically. Experiments show that the proposed algorithms outperform existing related works in efficiency and accuracy, and therefore can be effectively used in engineering applications.

FAN Guotian, WANG Zhibin

Multi-Task Learning with Dynamic Splitting for Open-Set Wireless Signal Recognition 44

The authors train a MTL network based on the characteristics of wireless signals to improve the performance in new scenes, and provide a dynamic method to decide the splitting ratio per class to get more precise outer samples. To be specific, they make perturbations to the sample from the center of one class toward its adversarial direction and the change point of confidence scores during this process is used as the splitting threshold. They conduct several experiments on one wireless signal dataset collected at 2.4 GHz ISM band by LimeSDR and one open modulation recognition dataset, and the analytical results demonstrate the effectiveness of the proposed method.

XU Yujie, ZHAO Qingchen, XU Xiaodong, QIN Xiaowei, CHEN Jianqiang

Multi-Cell Uplink Interference Management: A Distributed Power Control Method 56

This paper investigates a multi-cell uplink network, where the OFDM protocol is considered to mitigate the intra-cell interference. An opti-

mization problem is formulated to maximize the user supporting ratio for the uplink multi-cell system by optimizing the transmit power. This paper adopts the user supporting ratio as the main performance metric. Since the formulated optimization problem is non-convex, it cannot be solved by using traditional convex-based optimization methods. Thus, a distributed method with low complexity and a small amount of multi-cell interaction is proposed. Numerical results show that a notable performance gain achieved by the proposed scheme is without inter-cell interaction.

HU Huimin, LIU Yuan, GE Yiyang, WEI Ning, XIONG Ke

64 SVM for Constellation Shaped 8QAM PON System

The authors investigate the potential of constellation shaping joint SVM classification. At the transmitter side, the 8QAM constellation is shaped into three designs to mitigate the influence of noise and distortions in the PON channel. On the receiver side, simple multi-class linear SVM classifiers are utilized to replace complex equalization methods. Simulation results show that with the bandwidth of 25 GHz and overall bitrate of 50 Gbit/s, at 10 dBm input optical power of a 20 km SSMF, and under a hard-decision FEC threshold, transmission can be realized by employing Circular (4, 4) shaped 8QAM joint SVM classifier at the maximal power budget of 37.5 dB.

LI Zhongya, CHEN Rui, HUANG Xingang, ZHANG Junwen, NIU Wenqing, LU Qiuyi, CHI Nan

Review

72 General Introduction of Non-Terrestrial Networks for New Radio

In new radio (NR) access technology, the non-terrestrial networks (NTN) is introduced to meet the requirement of anywhere and anytime connections from the world market. With the introduction of NTN, the NR system is able to offer the wide-area coverage and ensure the service availability for users. In this paper, the general aspects of NTN are introduced, including the NTN architecture overview, the impact of NTN on next-generation radio access network (NG-RAN) interface functions, mobility scenarios and other NTN related issues. The current progress in 3rd Generation Partnership Group (3GPP) Release 17 is also provided.

HAN Jiren, GAO Yin

Serial parameters:CN 34-1294/TN*2003*q*16*78*en*P*¥ 20.00*2200*10*2022-S1

Statement

This magazine is a free publication for you. If you do not want to receive it in the future, you can send the "TD unsubscribe" mail to magazine@zte.com.cn. We will not send you this magazine again after receiving your email. Thank you for your support.



An Improved Parasitic Parameter Extraction Method for InP HEMT

Abstract: An improved parasitic parameter extraction method for InP high electron mobility transistor (HEMT) is presented. Parasitic parameter extraction is the first step of model parameter extraction and its accuracy has a great impact on the subsequent internal parameter extraction. It is necessary to accurately determine and effectively eliminate the parasitic effect, so as to avoid the error propagation to the internal circuit parameters. In this paper, in order to obtain higher accuracy of parasitic parameters, parasitic parameters are extracted based on traditional analytical method and optimization algorithm to obtain the best parasitic parameters. The validity of the proposed parasitic parameter extraction method is verified with excellent agreement between the measured and modeled S-parameters up to 40 GHz for InP HEMT. In 0.1 – 40 GHz InP HEMT, the average relative error of the optimization algorithm is about 9% higher than that of the analysis method, which verifies the validity of the parasitic parameter extraction method. The extraction of parasitic parameters not only provides a foundation for the high-precision extraction of small signal intrinsic parameters of HEMT devices, but also lays a foundation for the high-precision extraction of equivalent circuit model parameters of large signal and noise signals of HEMT devices.

Keywords: parasitic parameters; open-short test structure; parameter extraction; HEMT

DUAN Lanyan¹, LU Hongliang²,
QI Junjun², ZHANG Yuming²,
ZHANG Yimen²

(1. ZTE Corporation, Shenzhen 518057, China;
2. Key Laboratory of Wide Band-Gap
Semiconductor Materials and Devices, Xidian
University, Xi'an 710071, China)

DOI: 10.12142/ZTECOM.2022S1001

<http://kns.cnki.net/kcms/detail/34.1294.TN.20220119.1715.004.html>, published online
January 20, 2022

Manuscript received: 2021-05-16

Citation (IEEE Format): L. Y. Duan, H. L. Lu, J. J. Qi, et al., "An improved parasitic parameters extraction method for InP HEMT," *ZTE Communications*, vol. 20, no. S1, pp. 01 – 06, Jan. 2022. doi: 10.12142/ZTECOM.2022S1001.

1 Introduction

Compared to traditional Si-based Complementary Metal Oxide Semiconductor (CMOS) devices, InP high electron mobility transistors (HEMT) have better frequency response characteristics, power density and breakdown voltage, which makes InP HEMT an excellent candidate for many monolithic microwave integrated circuits (MMICs) working at gigahertz frequency ranges^[1-2]. As an important link between transistors and circuits, a small signal model is the basis of all device models. Therefore, the model accuracy depends mostly on the small signal equivalent circuit model which can reflect the physical and electrical properties of the device^[3].

The extraction of parasitic parameters is the first step of small signal model parameter extraction and its accuracy has a great influence on the subsequent extraction of intrinsic pa-

rameters. Commonly used parasitic parameter extraction methods include the open-short test structure method and cold-field effect transistor (FET) method. The former^[4-6] requires a test structure with the same size as the pad on a chip. The latter uses the equivalent circuit model of an HEMT device under the pinch off condition to extract parasitic parameters. The gate voltage is set at the threshold voltage and the drain source bias is set to zero. In Ref. [7], two identical capacitors C_b are used to simulate gate-to-source and gate-to-drain depletion layer capacitances. C_{pd} depends on the channel capacitance. A large C_b will cause a larger value of C_{pd} , and C_{pd} will be obviously overestimated. In order to avoid C_{pd} being overestimated, WHITE et al.^[8] added the third capacitance based on the Dambrin method, which is equal to C_b . The final results show that this method tends to underestimate C_{pd} . All cold-FET methods are based on the assumption that C_{gs} and C_{gd} of symmetrical field effect devices are equal under cold-FET biases. For the general HEMT device, this assumption is obviously not true.

Aiming at the problems of traditional methods, a new meth-

This work was supported by ZTE Industry–University–Institute Cooperation Funds under Grant No. HC-CN-20191121016.

od combining analytical and optimization methods to extract parasitic capacitance and inductance is proposed in this paper. Compared with previous literatures^[7-8], the proposed method has high accuracy and no complicated extraction process. Firstly, parasitic parameters obtained by the analytical method are used as the initial values of the optimization method, then the optimization method is used to optimize and fit the parasitic parameters, and finally the optimal values are obtained. The high precision of the values obtained by the proposed method has been validated by the open-short test structure method.

2 Device Structure and Model Description

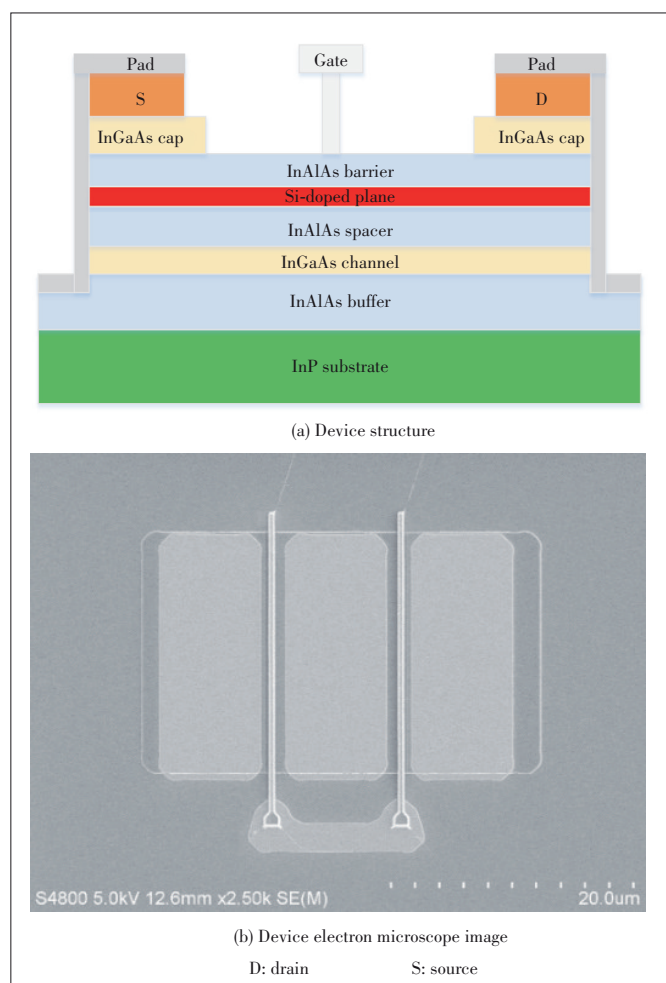
Fig. 1 shows the structure and electron micrographs of an InP HEMT device. The substrate is a semi-insulating InP substrate, and the buffer layer uses $\text{In}_{0.52}\text{Al}_{0.48}\text{As}$ material with a small lattice mismatch with the InP substrate, which is mainly used as a connecting liner. The bottom and the functional layer can prevent impurities from the substrate entering the chan-

nel. The channel layer uses a narrow band gap $\text{In}_{0.53}\text{Ga}_{0.47}\text{As}$ material, and the barrier layer uses an n-type doped $\text{In}_{0.52}\text{Al}_{0.48}\text{As}$ material. The channel and barrier layers will generate two-dimensional electron gas. The band is narrow, so the two-dimensional electron gas will be stored in the potential well at the interface of the channel layer to form a conductive channel. In order to reduce the Coulomb scattering of the channel two-dimensional electron gas by the barrier layer impurities, a thin layer of intrinsic $\text{In}_{0.52}\text{Al}_{0.48}\text{As}$ is added between the channel layer and the barrier layer. The cap layer uses a highly doped narrow band gap InGaAs material, which aims to form a good ohmic contact while reducing the source and drain resistance. A T-shaped gate is used to reduce the gate length and improves frequency characteristics while avoiding the increase of gate parasitic resistance, so that the device has better frequency characteristics.

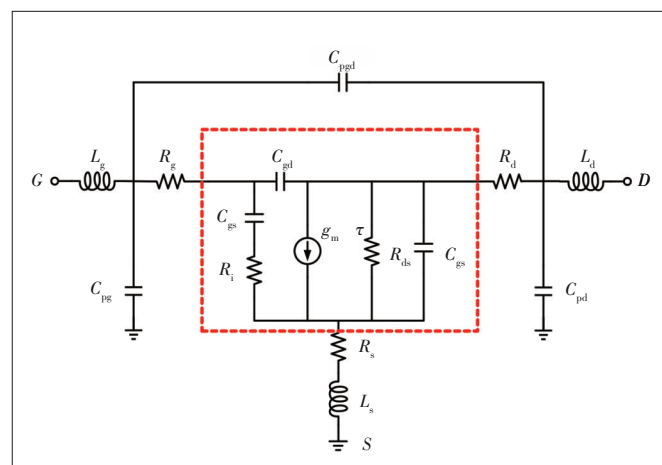
Fig. 2 shows the small signal equivalent circuit topology for this device. This equivalent circuit includes two parts: the inner part contains intrinsic elements and the outer part contains parasitic elements. L_g , L_s and L_d represent the gate, source and drain pad parasitic inductances; R_s and R_d are the source and drain parasitic resistances, and R_g is the gate distributed resistance; C_{pg} , C_{pgd} and C_{pd} are the gate and drain pad parasitic capacitances; C_{gs} , C_{gd} and C_{ds} represent the gate-source, gate-drain, and drain source capacitances, respectively; R_i , R_{gd} and R_{ds} are the charge and output resistances; τ and g_m are the intrinsic delay and intrinsic transconductance, correspondingly. C_{gs} , C_{gd} , C_{ds} , R_i , R_{gd} , R_{ds} , τ and g_m are intrinsic elements which are emphasized by the red dashed frame in Fig. 2. The rest are extrinsic elements which are considered to be bias independent.

3 Extrinsic Model Parameter Extraction and Verification

This modeling and circuit design uses the 0.15 μm InP



▲ Figure 1. Photograph of InP high electron mobility transistor (HEMT) device structure



▲ Figure 2. Small signal equivalent circuit for InP high electron mobility transistors (HEMT)

HEMT process of the Institute of Microelectronics of the Chinese Academy of Sciences, with a gate width of $2 \times 20 \mu\text{m}$. The frequency range of on-wafer S -parameters is from 0.1 to 40 GHz with steps of 0.1 GHz, including an open-short test structure. The whole parasitic parameter extraction process is shown in Fig. 3.

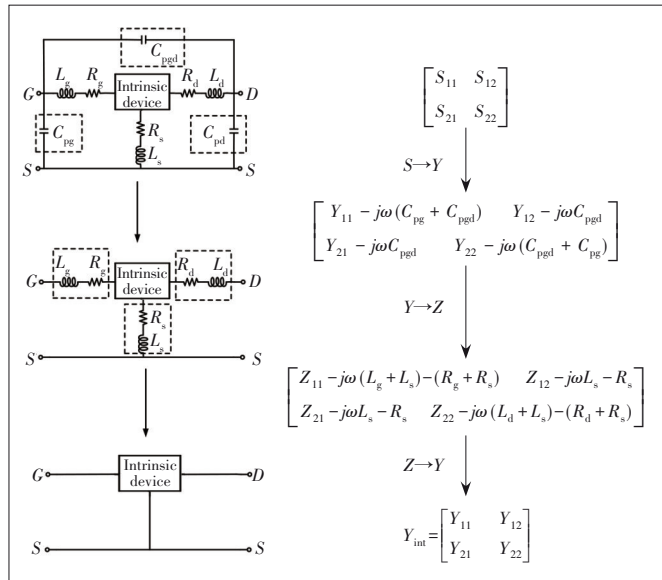
3.1 Parasitic Capacitances

The equivalent topology of dummy open structure^[9] is shown in Fig. 4. This structure can be equivalent to a π -type network, and the parameter Y can be used to solve the parasitic capacitances.

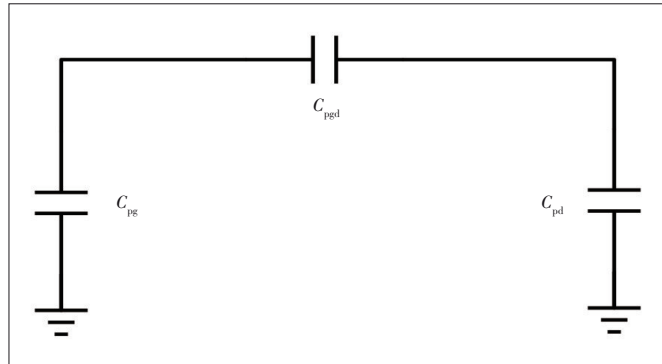
The parasitic capacitance values can be analyzed and characterized by the following formulas:

$$C_{pg} = \frac{1}{\omega} \text{Im}(Y_{11} + Y_{12}), \quad (1)$$

$$C_{pgd} = -\frac{1}{\omega} \text{Im}(Y_{12}), \quad (2)$$



▲ Figure 3. Parasitic parameter extraction process



▲ Figure 4. Equivalent circuit of the open dummy structure

$$C_{pd} = \frac{1}{\omega} \text{Im}(Y_{22} + Y_{12}). \quad (3)$$

According to Eqs. (1 – 3), three capacitance values can be extracted, as shown in Table 1.

3.2 Parasitic Inductances and Resistances

The equivalent topology of dummy short structure^[10–11] is shown in Fig. 5. This structure can be equivalent to a T-type network, and parasitic resistors and inductors in series can be extracted by the Z -parameters after the parasitic capacitances are de-embedded.

The Z -parameters of the equivalent circuit in Fig. 5 are written as

$$Z_{11} = R_g + R_s + j\omega(L_g + L_s), \quad (4)$$

$$Z_{12} = Z_{21} = R_s + j\omega L_s, \quad (5)$$

$$Z_{22} = R_d + R_s + j\omega(L_d + L_s). \quad (6)$$

Usually, the parasitic inductances and resistances can be analyzed and characterized by the following formulas:

$$L_g = \frac{1}{\omega} \text{Im}(Z_{11} - Z_{12}), \quad (7)$$

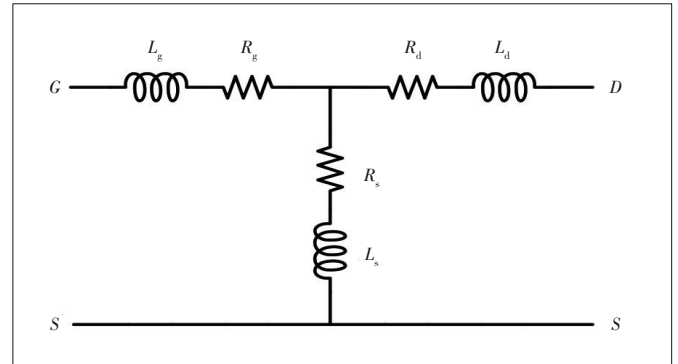
$$L_s = \frac{1}{\omega} \text{Im}(Z_{12}), \quad (8)$$

$$L_d = \frac{1}{\omega} \text{Im}(Z_{22} - Z_{12}), \quad (9)$$

$$R_g = \text{Re}(Z_{11} - Z_{12}), \quad (10)$$

▼ Table 1. Extraction of parasitic capacitance values

C_{pg}/fF	C_{pgd}/fF	C_{pd}/fF
21.497	1.647	20.407



▲ Figure 5. Equivalent circuit of the dummy short structure

$$R_s = \text{Re}(Z_{12}), \quad (11)$$

$$R_d = \text{Re}(Z_{22} - Z_{12}). \quad (12)$$

According to Eqs. (7 – 12), three inductance and resistance values can be extracted, as shown in Table 2.

Fig. 6 shows the simulation results of the extracted parasitic parameter values by dummy short structure and measurement data.

It can be found from Fig. 6 that the parasitic parameters extracted by the short structure that directly uses the Z parameters are not accurate. According to Eqs. (4 – 6), the extraction accuracy of R_s and L_s will directly affect the extraction accuracy of R_g , L_g , R_d and L_d . Fig. 6(c) shows that the real part of Z_{12} is a quantity that varies with frequency. In this case, extract-

ing R_s and L_s will increase the extraction error and further reduce the accuracy of extracting other parasitic parameters, which will lead to unsatisfactory fitting results.

There is a Chinese literature that proposed an algorithm based on feature points to simultaneously extract parasitic inductances and parasitic resistances. The author regards the three resistance and inductance series as three separate parameters, corresponding to Y_g , Y_s , Y_d , namely

$$Y_i = \frac{I}{R_i + j\omega L_i} = \frac{R_i}{R_i^2 + \omega^2 L_i^2} - j \frac{\omega L_i}{R_i^2 + \omega^2 L_i^2} \quad (i = g, s, d). \quad (13)$$

The imaginary part is

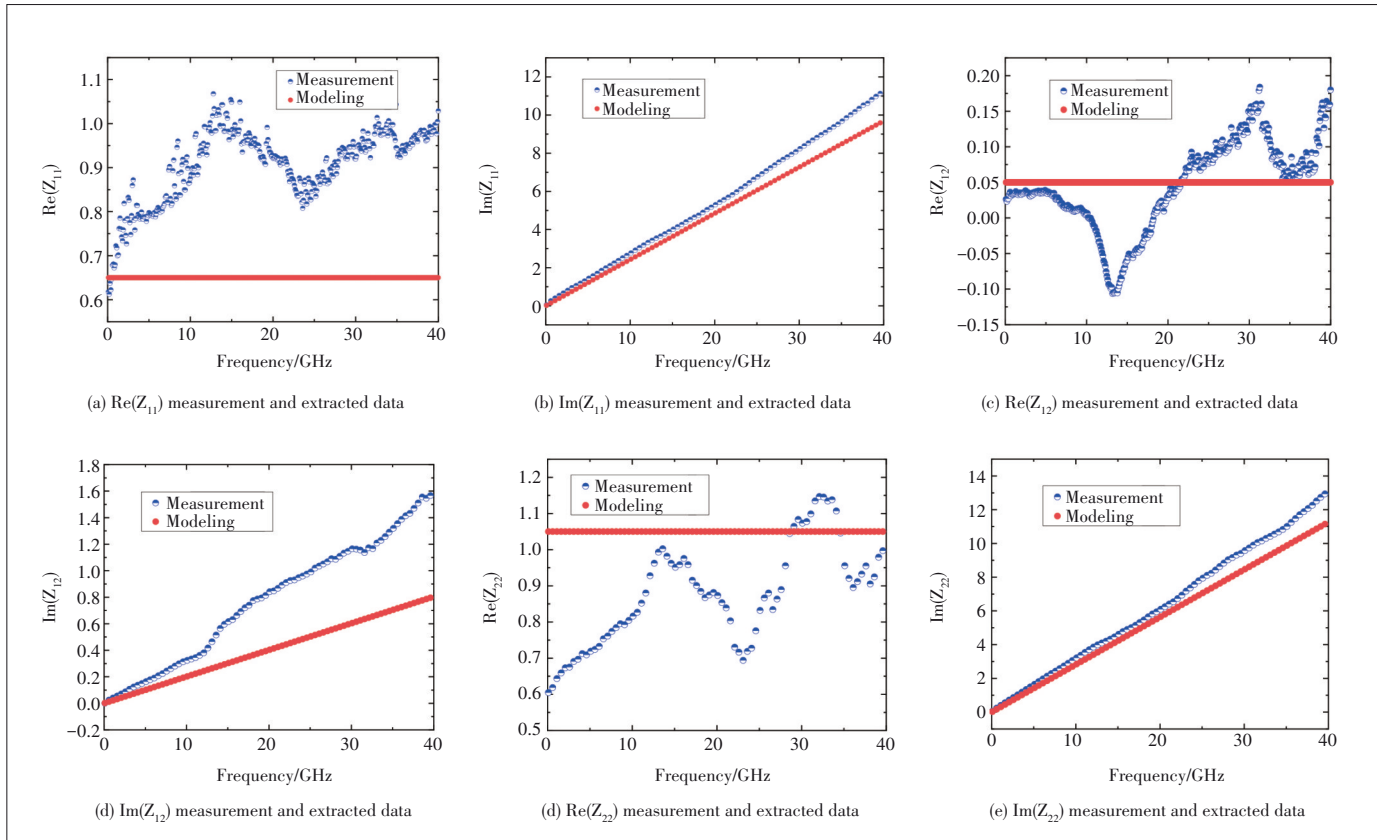
$$\text{imag}(Y_i) = -\frac{L_i}{\frac{R_i^2}{\omega} + \omega L_i^2} \quad (i = g, s, d). \quad (14)$$

From Eqs. (13) and (14), we can see that when $\omega = R/L$, $\text{imag}(Y_i)$ has a minimum value: $-1/(2R)$. Through this point, the inductance and resistance values can be extracted at the same time. The experiments show that the results of this extraction are not unsatisfactory.

Through the comparison of the research results, the open-

▼Table 2. Extraction of parasitic inductance and resistance values

Parasitic Parameter	Value
L_g/pH	35.355
L_s/pH	3.200
L_d/pH	41.599
R_g/Ω	0.600
R_s/Ω	0.050
R_d/Ω	1.000



▲Figure 6. Comparison of parasitic parameters extracted by the dummy short structure and measurement data

short structure combined with the analytical method to solve the parasitic parameters does not get satisfactory results. Based on the open-short structure, we propose a method combining analytical and optimization methods to extract parasitic parameters. We use the parasitic parameter values obtained by the analytical method as the initial values of the optimization method, and then use the optimization method to optimize the parasitic parameters to obtain the final values.

3.3 Extrinsic Parameters Verification

The extraction results of parasitic inductance and parasitic resistance obtained by the combination of the analytical method and optimization method are shown in Table 3.

Fig. 7 shows the comparison between the measured data and the modeled data of the optimization method and analytical method.

▼Table 3. Extraction of extrinsic inductances and resistances

Extrinsic Parameter	Value
L_g/pH	39.467
L_d/pH	5.076
L_s/pH	47.676
R_g/Ω	0.725
R_d/Ω	0.034
R_s/Ω	0.639

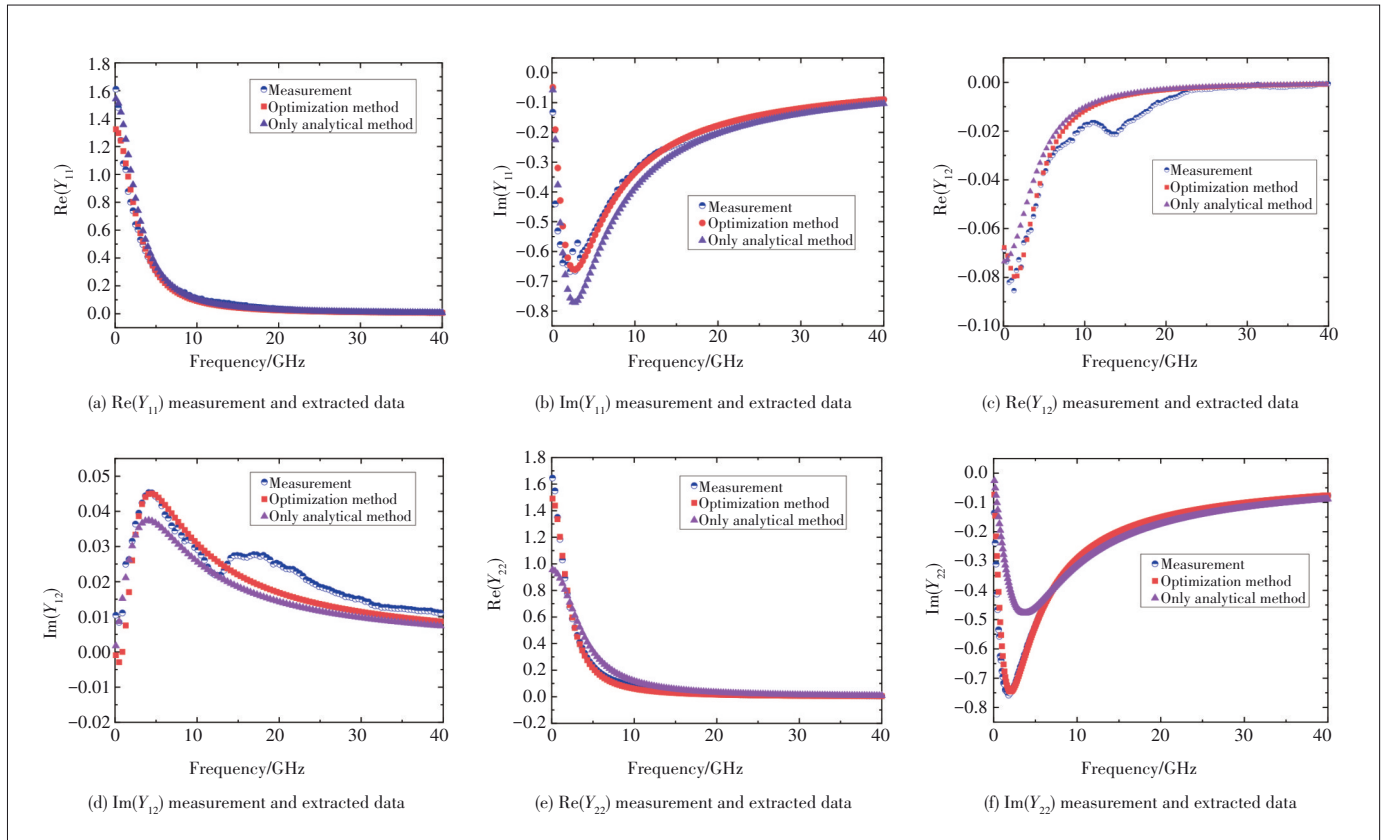
It can be seen from Fig. 7 that the parasitic parameter extraction results obtained by combining the analytical method and the optimization method fit more accurately. To further evaluate the accuracy of S -parameters, the percentage error expression, $\text{Error}(S)$, is defined as follow:

$$\text{Error}(S) = \sum_{i,j=1,2} \frac{|S_{S,ij} - S_{M,ij}|}{0.5 \times |S_{S,ij} + S_{M,ij}|} \times 100\% \quad (15)$$

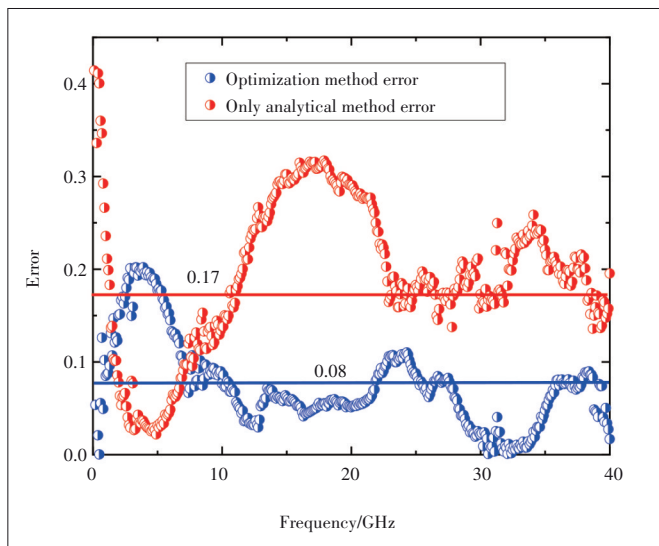
where $S_{S,ij}$ is the simulated S -parameters and $S_{M,ij}$ is the measured data. According to Eq. (15), the errors of the fitting data obtained by the two methods are calculated respectively. Comparing the error calculation results, the average relative error of the final optimization algorithm is about 9% higher than that of the analytical method (blue line in Fig. 8). In Fig. 8, the blue and red solid lines represent the average relative errors of the optimization method and the analytical method respectively, and the blue circle and red circle represent the relative errors of the optimization method and the analytical method in the whole frequency band respectively.

4 Conclusions

In this paper, an improved parasitic parameter extraction



▲Figure 7. Comparison of extracted parasitic parameters by dummy short structure and measurement data



▲ Figure 8. S-parameters fitting errors of the improved extracted method

method for InP HEMT is presented. Based on the open-short structure, we use the analytical method to obtain the parasitic parameters, and then optimize the parasitic parameters by the optimization method to obtain the final values. An excellent agreement between the measured and modeled S-parameters is up to 40 GHz, which verifies the applicability of the proposed modeling methods for InP HEMT.

References

- [1] KULATUNGA T, BELOSTOTSKI L, HASLETT J W. 400-to-800-MHz GaAs pHEMT-based wideband LNA for radio-astronomy antenna-array feed [J]. IEEE microwave and wireless components letters, 2018, 28(10): 909 – 911. DOI: 10.1109/LMWC.2018.2864880
- [2] ALIZADEH A, MEDI A. A broadband integrated class-J power amplifier in GaAs pHEMT technology [J]. IEEE transactions on microwave theory and techniques, 2016, 64(6): 1822 – 1830. DOI: 10.1109/TMTT.2016.2552167
- [3] BERROTH M, BOSCH R. High-frequency equivalent circuit of GaAs FETs for large-signal applications [J]. IEEE transactions on microwave theory and techniques, 1991, 39(2): 224 – 229. DOI: 10.1109/22.102964
- [4] ZHONG Y H, LI K K, LI M K, et al. An improved 16-element small-signal model for InP-based HEMTs [J]. Journal of infrared and millimeter waves, 2018, 37 (2): 163 – 167. DOI:10.11972/j.issn.1001-9014.2018.02.006
- [5] GAO J J. RF and microwave modeling and measurement techniques for field effect transistors [M]. Raleigh, USA: SciTech Publishing Inc, 2010
- [6] COSTA D, LIU W U, HARRIS J S. Direct extraction of the AlGaAs/GaAs het-

- erojunction bipolar transistor small-signal equivalent circuit [J]. IEEE transactions on electron devices, 1991, 38(9): 2018 – 2024. DOI: 10.1109/16.83724
- [7] DAMBRINE G, CAPPY A, HELIODORE F, et al. A new method for determining the FET small-signal equivalent circuit [J]. IEEE transactions on microwave theory and techniques, 1988, 36(7): 1151 – 1159. DOI: 10.1109/22.3650
- [8] WHITE P M, HEALY R M. Improved equivalent circuit for determination of MESFET and HEMT parasitic capacitances from “Coldfet” measurements [J]. IEEE microwave and guided wave letters, 1993, 3(12): 453 – 454. DOI: 10.1109/75.251398
- [9] ZHANG H S, MA P J, LU Y, et al. Extraction method for parasitic capacitances and inductances of HEMT models [J]. Solid-state electronics, 2017, 129: 108 – 113. DOI: 10.1016/j.sse.2016.12.003
- [10] KAUSHIK P K, GOYAL U. Extraction and de-embedding of S-parameters using small-signal modeling for AlGaIn/GaN HEMTs [C]//14th IEEE India Council International Conference. IEEE, 2017: 1 – 6. DOI: 10.1109/INDICON.2017.8488156
- [11] CHUMBES E M, SCHREMER A T, SMART J A, et al. AlGaIn/GaN high electron mobility transistors on Si(111) substrates [J]. IEEE transactions on electron devices, 2001, 48(3): 420 – 426. DOI: 10.1109/16.906430

Biographies

DUAN Lanyan received the M.S degree in circuit and system from Hunan University, China in 2002. She joined ZTE Corporation in 2002. Now, she is a senior technology and quality engineer in ZTE Corporation. Her main research direction is the development of RF material.

LU Hongliang (hllv@mail.xidian.edu.cn) received the M.S. and Ph.D. degrees in microelectronics engineering from Xidian University, China in 2003 and 2007, respectively. Since 2010, she has been a professor with the School of Microelectronics, Xidian University. Her current research interests include modeling and experiments on SiC MESFET and other devices.

QI Junjun is currently pursuing the Ph.D. degree at the School of Microelectronics, Xidian University, China. Her current research interests include model analysis and extraction of small signal equivalent parameters.

ZHANG Yuming received the M.S. degree from Xidian University, China in 1992, and the Ph.D. degree from Xi'an Jiaotong University, China in 1998. Since 2001, he has been a professor with the Microelectronics Institute, Xidian University. His current research interests include design, modeling, fabrication, and electrical characterization of SiC electronic devices for high-temperature and high-power operation. He is a senior member of IEEE.

ZHANG Yimen is a professor with the School of Microelectronics, Xidian University, China. He has also been a visiting scholar with Arizona State University, USA and a senior visiting scholar with Yale University, USA. His current research interests include wideband semiconductor devices, semiconductor devices modeling, TCAD for VLSI, and quantum well devices.



Auxiliary Fault Location on Commercial Equipment Based on Supervised Machine Learning

Abstract: As the fundamental infrastructure of the Internet, the optical network carries a great amount of Internet traffic. There would be great financial losses if some faults happen. Therefore, fault location is very important for the operation and maintenance in optical networks. Due to complex relationships among each network element in topology level, each board in network element level, and each component in board level, the concrete fault location is hard for traditional method. In recent years, machine learning, especially deep learning, has been applied to many complex problems, because machine learning can find potential non-linear mapping from some inputs to the output. In this paper, we introduce supervised machine learning to propose a complete process for fault location. Firstly, we use data preprocessing, data annotation, and data augmentation in order to process original collected data to build a high-quality dataset. Then, two machine learning algorithms (convolutional neural networks and deep neural networks) are applied on the dataset. The evaluation on commercial optical networks shows that this process helps improve the quality of dataset, and two algorithms perform well on fault location.

Keywords: optical network; fault location; supervised machine learning

ZHAO Zipiao¹, ZHAO Yongli¹,
YAN Boyuan¹, WANG Dajiang²

(1. State Key Laboratory of Information Photonics and Optical Communications, Beijing University of Posts and Telecommunications, Beijing 100876, China;

2. ZTE Corporation, Shenzhen 518057, China)

DOI: 10.12142/ZTECOM.2022S1002

<http://kns.cnki.net/kcms/detail/34.1294.TN.20220106.1424.002.html>, published online January 7, 2022

Manuscript received: 2020-04-01

Citation (IEEE Format): Z. P. Zhao, Y. L. Zhao, B. Y. Yan, et al., "Auxiliary fault location on commercial equipment based on supervised machine learning," *ZTE Communications*, vol. 20, no. S1, pp. 07 – 15, Jan. 2022. doi: 10.12142/ZTECOM.2022S1002.

1 Introduction

With the explosive growth of Internet traffic and the emergence of new applications, the requirement for traffic bandwidth increases rapidly. As the fundamental infrastructure of the network, the optical network becomes more and more important because of its super-high transmission speed. Therefore, there should be considerable economic damages in case of optical network failures. In reality, the economic loss is closely related to the network restoration time, which consists of the time to locate the fault, to drive to the place, and to fix the problem. If the fault location is fuzzy and even wrong, the restoration time will be doubled and redoubled. Hence, it's important to find the fault location rapidly and accurately^[1].

Until now, some researchers have studied fault location

from different aspects. Generally, there is no protocol to detect network faults in transparent optical networks, because such protocols will cost more in equipment manufacture and increase the complexity of current protocol stacks. The current fault location technology is inefficient, which depends on the expert knowledge base and traditional fiber link fault location. However, the breakthrough of machine learning in recent years offers the possibility of solving this problem.

Machine learning (ML) is an important subset of artificial intelligence, which builds a mathematical model based on sample data, known as "training data", to make predictions or decisions without being explicitly programmed to perform the task^[2]. The introduction of ML into fault location has become a hot spot. In Ref. [3], a recurrent neural network-based method is used in the fault detection and isolation of the satellite's attitude control subsystem. In Ref. [4], a fault section estimation in electric power systems is handled, where neural networks are employed to model the protection systems, dealing with the uncertainties involved with relay and circuit-breaker operation messages. In Ref. [5], a deep

This work was supported in part by National Natural Science Foundation of China (NSFC) (61822105, 61571058, 61601052) and by ZTE Industry-Academia-Research Cooperation Funds under Grant No. 2018110016001047.

learning (DL) based algorithm is proposed to combine supervised and unsupervised learning, and solve the fault in power systems. Also, there are some research works related to the fault in optical networks^[6]. In Refs. [7 – 9], a Bayesian inference method is used to judge service-triggered failure in optical transport networks and self-diagnosis in fiber to the home (FTTH) gigabit-capable passive optical networks (GPON). In Ref. [10], the previously established lightpaths with already available failure localization and monitoring data are used to estimate the failure localization at the link level for all lightpaths with Kriging method. In Ref. [11], two ML based algorithms are described based on regression, classification, and anomaly detection. The authors propose a bit error ratio (BER) anomaly detection algorithm which takes historical information (like maximum BER, threshold BER at set-up, and monitored BER per lightpath) as input, and detects any abrupt change in BER which might be a result of some failures of components along a lightpath. In Ref. [12], two algorithms for testing optical switching at connection setup time and failure rootcause localization for optical network are proposed using decision tree and support vector machine (SVM) algorithms. And a similar multi-ML algorithm for failure detection and classification is proposed in Refs. [13 – 14], including binary and multi-class SVMs, random forests and neural networks (NN). However, the work mentioned above fails to take full advantage of the huge data collected from optical networks, and is difficult to be deployed into the real commercial environment. In this paper, we study the alarm data preprocessing to improve the quality of the dataset and mine the association rules. Based on the dataset, two fault location algorithms based on the convolutional neural network (CNN) and the deep neural network (DNN) respectively are proposed.

The rest of this paper is organized as follows. In Section 2, the originally collected data are converted into the universal format, and some association rules are studied. Then the mappings between the input and the label are built for an available dataset. Meanwhile, some data augmentation methods are used to expand the size of the dataset. In Section 3, CNN and DNN algorithms are explained and introduced to help solve the fault location problem. In Section 4, based on the original data collected from commercial optical networks, the procedure described in Section 2 and the algorithm are evaluated with the Tensorflow^[15] AI platform. In Section 5, we draw a conclusion.

2 Building Alarm Dataset

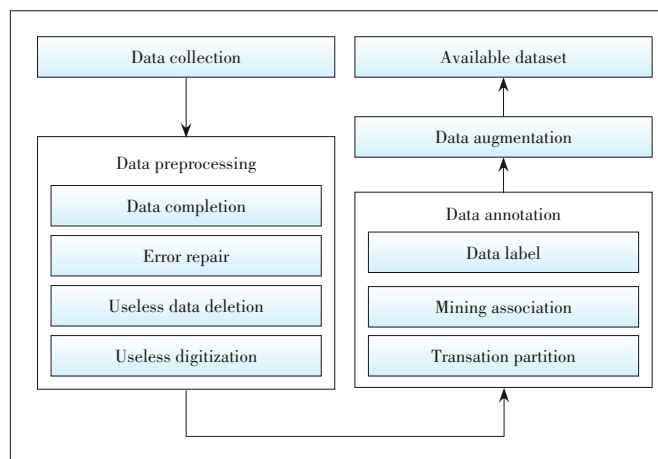
The quality of a dataset has an important influence on the performance of fault location, which determines the performance limit directly and impacts model training indirectly. Therefore, it is essential to build a high-quality dataset based on original data. As Fig. 1 shows, in order to make an

available dataset, data collection, data preprocessing, data annotation, and data augmentation are executed successively.

There are generally four kinds of data in optical equipment: the performance data, the alarm data, the configuration data, and the event report. All these data could be collected from the equipment management system directly. In the phase of data collection, we use a self-optimizing optical network (SOON) platform^[16–17] to gather all data through an open application programming interface (API) of optical equipment.

The original data collected from optical equipment directly are generally dirty^[18], which means that these data include missing data, wrong data, non-standard representations of the same data, etc.^[19]. In a fault location application, we only need to process alarm data, including history alarm data and current alarm data. The history alarm data are the alarms that have been confirmed and cleaned. And the current alarm data summarize the happened alarms that have not been confirmed and cleaned simultaneously. The indices of history alarm data include the alarm level, alarm name, alarm source, network element type, location information, happen time, clean time, and confirm time. And the indices of current alarm data include alarm level, alarm name, alarm source, location information, frequency, time to first alarm, time to last alarm, and clean time. In the phase of data preprocessing, data completion is used to remove the severely defective data records and complement partial missing data records. Error repair is used to detect obvious data errors in format and content, and fix them. Then, useless data deletion is used to remove the useless data records. For example, if the repair for the network failure is delayed for a while, the same alarm data will be triggered again and again. In hundreds of the same alarm records, we only need one of them. Finally, we digitalize all data by mapping the text to a specific integer.

After some steps of data preprocessing, high-quality alarm data are generated. Because the used algorithms are super-



▲ Figure 1. Data preprocessing for collected alarm data

vised, we need to mark data to add a label for each data item. Firstly, we use a sliding window^[20] to convert alarm data records into transactions. We assume that b is the beginning time, w is the length of a time window, and s is the step length between two adjacent transactions. Then the k -th transaction includes the data records in time period $(b+k*s, b+k*s+w]$.

According to different value setups of b , s , and w , we could get multiple original datasets. Considering known algorithms to mine association rules, we select a frequent pattern growth^[21] (FP-growth) algorithm, as it is one of the fastest approaches to a frequent item set mining^[22]. The key idea of FP-growth is partition, which executes a frequent pattern tree (FP-tree) to generate a common frequent pattern through only two times that of data traversal. The process is as follows.

1) Firstly, it scans all stored alarm transactions, calculates the frequency of each transaction as the support degree, and drops those transactions whose support degree is less than the minimal support degree. Then, it sorts all transactions with support degrees in descending order, and stores them in a list L .

2) Secondly, an FP-tree is built. In an FP-tree, the root node is initialized as null. Then, a frequent pattern subtree is created. If the conditional pattern bases of FP-tree are the same, the support value on these nodes is plus 1. If not, then it creates a new node with the support degree as 1.

3) Lastly, it mines FP-tree in a reverse order of list L , creates the conditional pattern base for each item, and combines all bases for the same alarm data to build its FP-tree. This step is repeated until there is no unused conditional pattern base.

The last phase to generate an available dataset is to augment data. In a commercial optical network, the data about network failures are much less than those in the normal state. So, the size of a fault dataset is quite small. Meanwhile, the distribution for events caused by different reasons is uneven. In order to avoid negative effects of small size and maldistribution, data augmentation could be used to expand specific data and keep the distribution balance. In image recognition, an image could be augmented to multiple images through rotation, translation, reversal, clipping, Gaussian noise, etc. In fault location, although there are already several data augmentation methods^[17], we still need to manually expand data depending on artificial expertise under specific scenarios. For example, if we want to expand alarm data caused by clock

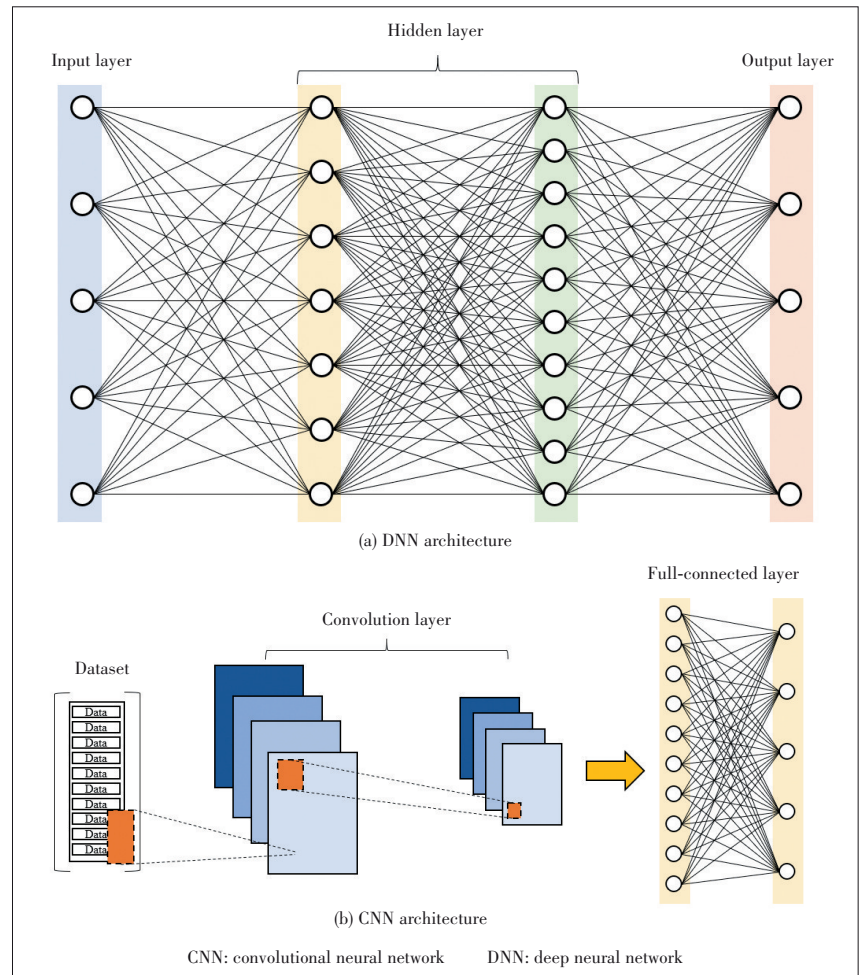
failure, firstly we should abstract all clock topologies that exist in an optical network, and mark where the clock is for each clock topology. For alarm data caused on a specific clock, we could simulate the same failure on other clock to generate new clock alarm data.

3 Auxiliary Fault Location

CNN and DNN are two important tools in supervised machine learning which aim to find an accurate mapping between the input and the output. Based on the available dataset generated in Section 2, these two algorithms are used to find the relationship between the alarm data and the fault location.

3.1 Fault Location with Deep Neural Network

DNN is actually the fully-connected neural network where the number of layers is larger than four. Based on huge labeled training data, DNN can find the proper relationship mapping between the input and the output, especially for those fuzzy and complex mappings. As Fig. 2(a) shows, DNN



▲ Figure 2. CNN and DNN architecture

consists of the input layer, hidden layer, and output layer. Each layer contains multiple neurons, and each neuron could be defined as a non-linear function (Sigmoid^[23], tanh, Rectified Linear Unit^[24], etc.). Compared with the neural network with only 3 layers, DNN owns stronger feature expression. The update of DNN model normally consists of forward and back propagation. The forward propagation calculates the output of each neuron. The back propagation calculates the gradient of each parameter, and updates all parameters according to some learning rate policy, which is normally called gradient descent. The selection of the learning rate policy has an important impact on the performance of the model.

Apart from the learning rate policy, both parameter initialization and the neural network architecture are important. Parameter initialization decides the initial position for an ML model. As we know, gradient descent means that the ML model will search for a second-best solution on the hyper-plane. The initial position at the beginning may lead the model to a relatively poor solution. Gaussian and He are two common initialization methods. The architecture of the neural network contains the numbers of hidden layers and neurons on each layer mainly. More layers and more neurons on each layer will make the DNN's own learning ability powerful, meanwhile, it becomes more difficult to train such a model.

The concepts commonly used in several DNNs are described below:

1) Feature extraction. The purpose of deep learning is to enable the model to automatically extract the potential features of the data and complete the mapping from data to results. The extraction of deep-level valuable features of the data directly affects subsequent learning tasks and is the basis for the entire model training.

2) Multi-layer perceptron. A perceptron is a fully connected neural network structure with one input layer and one output layer through an activation function. Multi-layer perceptrons are fully connected neural networks with hidden layers.

3) Activation function. It is an important component of the artificial neural network (ANN) model. It can help the model to automatically learn and understand complex non-linear functions effectively, and introduce non-linear characteristics into the model.

4) Transfer learning. Transfer learning is to use the trained model and the acquired knowledge to solve the problem in the target domain, and realize the use of a small number of sample sets to train a highly reliable model.

5) Adaptive learning rate. The process of model training is greatly affected by the learning rate. If the set learning rate is large, oscillation will likely occur and the model cannot converge. The model converges slowly, so the adjustment of the learning rate is very important to the training of the model. If the learning rate can change with the training process of the

model, the training process of the model and its result are satisfactory.

6) Gradient descent (GD). A greedy algorithm in the training model process, based on the mathematical idea of differentiation, iterates continuously to find the fastest direction of gradient descent.

7) Error back-propagation (BP). Calculate the difference between the estimated value of the model and the actual value, continuously propagate the difference, continuously adjust the model parameters, update the global parameters, and obtain a high reliability model.

8) Regularization. It is used to solve the problem of over-fitting of model training, prevent the model from over-extracting data features, and balance the results of model training and the goal of smaller parameter values.

3.2 Fault Location with Convolutional Neural Network

CNN was firstly proposed in Ref. [25], which consists of the convolution layer, the pooling layer, and the fully-connected layer, as Fig. 2(b) shows. The calculation in the convolution layer is sparse, different from that in the fully-connected layer. In the convolution layer, multiple convolution kernels are used to execute a convolutional operation on the input data matrix. Then these values are handled by a non-linear function to adjust the nonlinear feature. The pooling layer only summarizes a data matrix into a value through a pooling function, for example, max-pooling that outputs the maximal value, min-pooling that outputs the minimal value, avg-pooling that outputs the average value of all elements, etc. The pooling layer aims to reduce the size of data while remaining the most important feature. After several convolution layers and pooling layers, the output will be converted to a one-dimensional array, as the input of the final fully-connected layer. In the fully-connected layer, the extracted features in different granularities and aspects could be mixed and considered together.

CNN is similar to DNN in many aspects. The mechanism of parameter update in CNN is also the combination of forwarding propagation and back propagation. The former is used to calculate the output of each kernel and each neuron for a specific input, the latter is used to calculate the gradients. In weight initialization, learning rate adjustment, and many other configurations, CNN normally takes the same approach as DNN does. Benefited from the extreme reduction of parameter numbers compared with DNN, CNN can take hundreds and thousands of convolution layers to extract more abstract features. However, although CNN has been proved in image classification and some other domains, due to CNN's black-box attribute, it's hard to prove and explain that CNN could be deployed on any domain problem strictly.

The following shows all the elements related to CNN and how they work in detail.

1) Convolution layer. It uses the convolution kernel to

scroll over the input data set according to the stride to extract the characteristics of the input data. The multi-layer convolution layer can better extract the inherent rich features of the data. Convolutional layers have important characteristics that contribute significantly to the performance of the system, such as sparse weights, but convolution operations may cause the loss of information that may exist on image boundaries. Because they are only captured when the filter slides, they may not have a chance to be seen. A simple and effective way to solve this problem is to use zero padding.

2) Pooling layer. The pooling layer is used to merge semantically similar resources in the output of a specific layer of the network. The pooling layer essentially reduces the input by merging adjacent values, so subsequent layers are represented using a smaller network structure. The most common pooling operation is max pooling, which returns the maximum value from a set of zone values.

3) Non-linearity. The next layer after convolution is non-linear. Non-linearity can be used to regulate or cut off the output produced. This layer is applied to saturate the output or limit the output produced. Sigmoid, Tanh, and ReLU functions are frequently used non-linear functions. Because the Sigmoid and Tanh functions are saturation functions, gradients disappear easily when the network layer is deep, which is suitable for situations where the network layer is not too deep. The gradient of the ReLU function in the positive part is constant, and the gradient of the ReLU function can be zero. It can be used for sparse representation. Therefore, the ReLU function is more widely used when the network level is deeper.

4) Fully connected layer. Each node in the fully connected layer is directly connected to each node in the previous and the next layer. The main disadvantage of the fully connected layer is that it contains many parameters and needs complex calculations in the training example. Therefore, we try to eliminate the number of nodes and connections, and use local connections to meet the requirements of reducing the number of nodes and connections. For example, Lenet and Alexnet are designed as a network of depth and breadth while maintaining computational complexity.

4 Simulation and Results

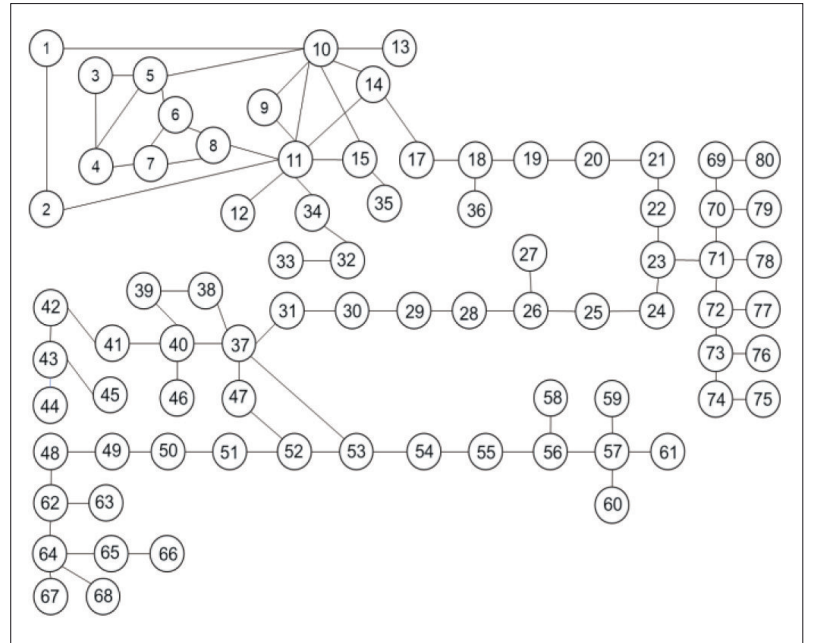
To evaluate the quality of the dataset we built, we introduce some other algorithms as the benchmark. And to compare the performance of CNN and DNN in the fault location, we also execute these algorithms on our dataset. The original data is collected from the commercial optical network as shown in Fig. 3.

4.1 Dataset

Table 1 shows the result of the FP-growth algorithm, which contains six transactions calculated from alarm data. The capital letter means specific alarm type, and the value in parentheses is the support degree. In the sliding window phase, we set w as 10 s, and s as 4 s to get the transaction set, as the second column shows in Table 1. Then the minimal support degree is set as 3, and the remaining transactions after filtering is shown in the third column of Table 1. After the FP-tree is built, we could get the conditional pattern base of the alarm data frequent item as follows.

- $A \rightarrow \{\}:5$
- $B \rightarrow \{A\}:1, \{A, C, D\}:1, \{C, E\}:1$
- $C \rightarrow \{A\}:3, \{\}:1$
- $D \rightarrow \{A, C\}:3$
- $E \rightarrow \{A, C, D, E\}:2, \{C\}:1$
- $F \rightarrow \{A, C, D, E\}:2, \{A, C, D, B\}:1$

In this paper, we introduce several classical association rule mining algorithms like MINWAL(w), Apriori, and BEPMWA, to compare the time performance of FP-growth as Figs. 4(a) and 4(b) shows. Also, we add a distributed version of FP-Growth, called FP-Growth-Distributed. Fig. 4(a)

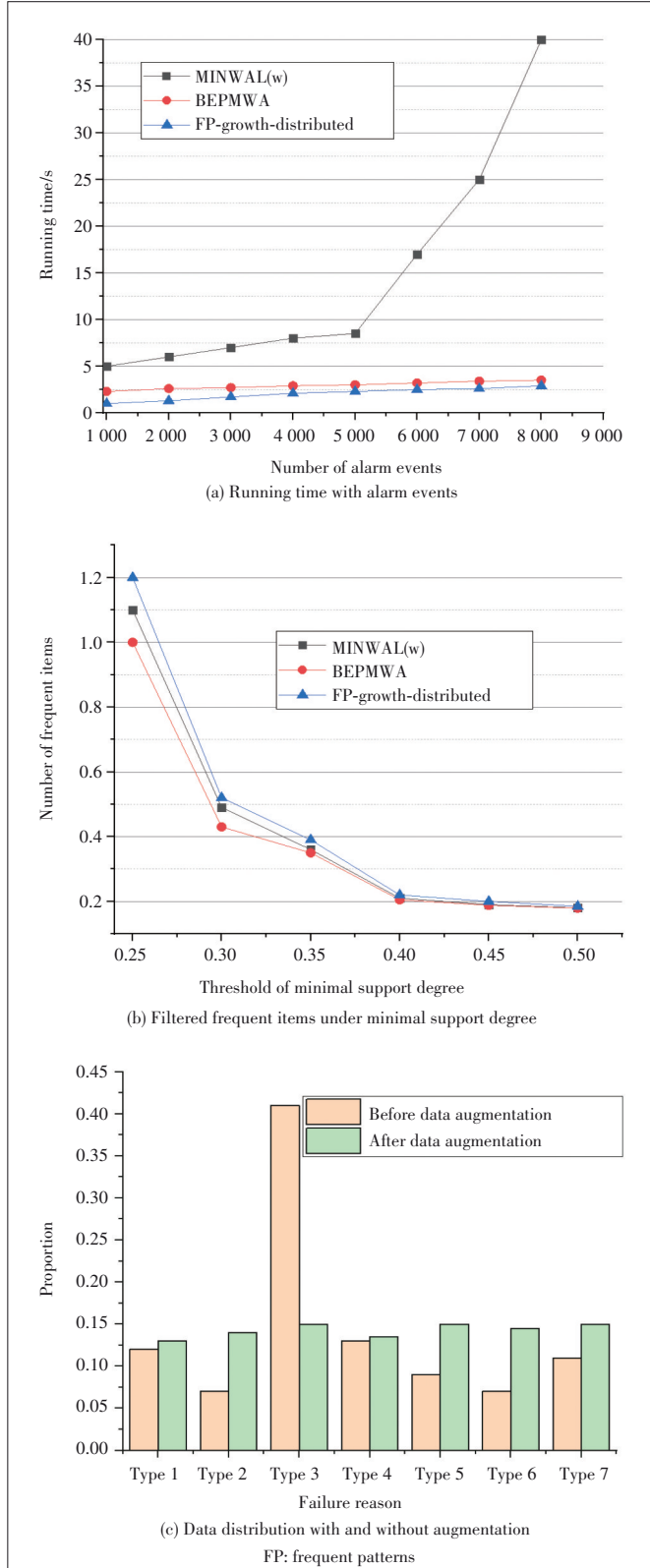


▲ Figure 3. Commercial optical network for evaluation

▼ Table 1. Frequent item using FP-growth

Transaction ID	Included Alarm Data	Filtered Alarm Data
001	B, A, H, J, P	A(5), B(3)
002	A, D, C, W, U, V, F, E	A(5), C(4), D(3), F(3), E(3)
003	A	A(5)
004	B, C, N, O, E	C(4), B(3)
005	D, B, C, A, Q, F, P	A(5), C(4), B(3), D(3), F(3)
006	D, A, C, G, Q, E, F, M	A(5), C(4), D(3), E(3), F(3)

shows the treatment efficiency for alarm events. The time cost of MINWAL(w) increases rapidly, but the time cost of



▲ Figure 4. Results of building an available dataset

other algorithms remains a linear growth. MINWAL(w) always consumes the most time, and FP-Growth-Distributed always has the highest efficiency. Fig. 4(b) shows the size of filtered frequent items with different thresholds of the minimal support degree. All algorithms generate about the same size of frequent items when the minimal support degree increases, which means they perform similarly on the frequent item selection. However, when the minimal support degree is small, FP-Growth-Distributed performs better. Then, as mentioned in Section 2, the data augmentation method is executed manually. Fig. 4(c) shows the size comparison before and after data augmentation. Data augmentation balances the distribution of transaction caused by different failure reasons.

4.2 Performance Evaluation

After the process of the previous subsection, an available dataset is built. The input is transaction, and the output is the fault type. In this paper, 8 fault types are introduced, including no fault, fiber interruption, board failure, clock failure, control board failure, power failure, base environment degradation, and line loss. So the size of the output is 8.

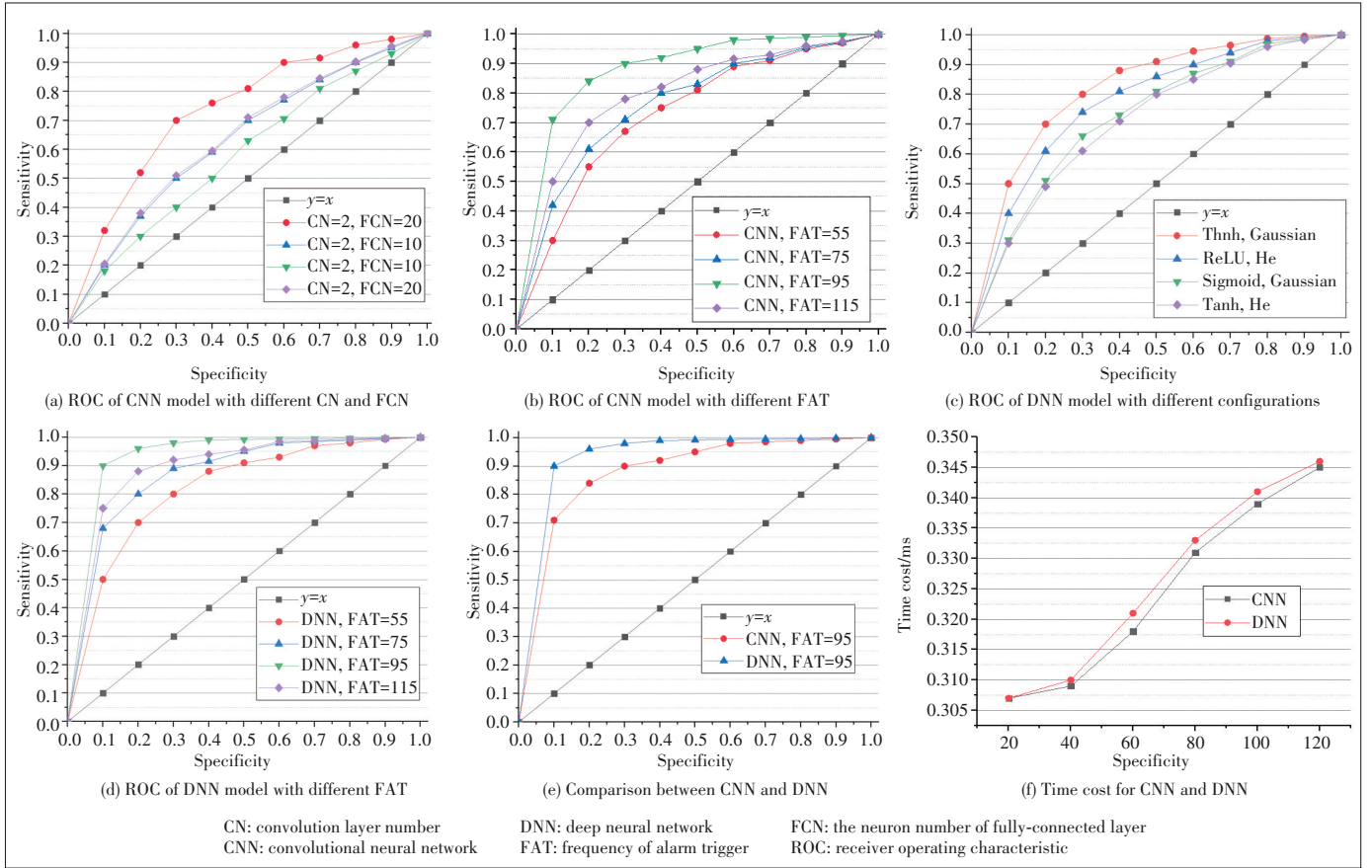
In the evaluation for classification task, TP indicates that network failure happens, and the output of ML algorithm is correct. FP indicates that network failure doesn't happen, but the output makes a mis-judgement. FN indicates that network failure happens, but the output makes a mis-judgement. And TN indicates that network failure doesn't happen, and the output is correct. Then the sensitivity and specificity are described as in Eqs. (1) and (2). We make x-axis as the specificity, and y-axis as the sensitivity to draw receiver operating characteristic (ROC) curves for CNN and DNN in Figs. 5(a) and (b). The area surrounded by line $x=y$ and an arc shows the performance. The performance is better when the area is bigger.

$$\text{Sensitivity} = \frac{TP}{TP + FN} \quad (1)$$

$$\text{Specificity} = \frac{TN}{TN + FP} \quad (2)$$

In Fig. 5(a), CN means the number of convolution layers, and FCN means the neuron number of fully-connected layers. In several different configurations, CNN performs the best when CN is 2 and FCN is 20. Based on such optimal parameter combination, Fig. 5(b) shows the influence of frequency of alarm trigger (FAT). This CNN model reaches its best performance while FAT equals 95.

In Fig. 5(c), we set the learning rate as the adjustable learning rate, and the number of hidden layers is 5. Tanh, ReLU, and Sigmoid are the activation functions in a neuron. Gaussian and He are parameter initialization methods. Ac-



▲ Figure 5. Evaluation results for CNN and DNN model

cording to some advanced hyper-parameter filters, we skip many parameter combinations, and only 4 kinds of them remain in Fig. 5(c). In all DNN models, the parameter combination with ALR, Layers=5, Tanh, and Gaussian performs the best. Based on such optimal parameter combination, Fig. 5 (d) shows the influence of FAT on this best DNN model. Same with Fig. 5(b), this DNN model reaches its best performance while FAT equals 95.

Fig. 5(e) compares the performance of the best CNN model and the best DNN model where FAT equals 95. When the specificity is specified, the sensitivity of DNN is larger than that of CNN, which indicates that the DNN algorithm could perform better than CNN on the fault location dataset. On the other side, in Fig. 5(f), we evaluate the time cost of CNN and DNN under different FATs. DNN costs more time than CNN does, however, the millisecond level is enough for the commercial requirement.

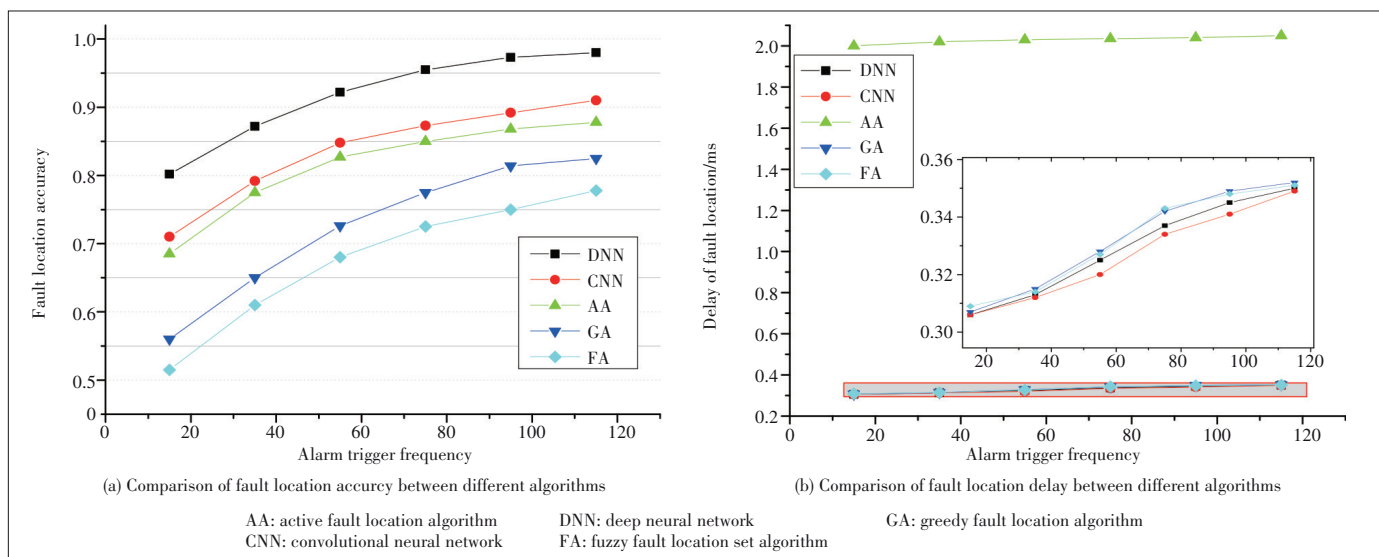
Figs. 6(a) and 6(b) are comparisons of different fault location algorithms in terms of fault location accuracy and location delay. DNN stands for fault location based on deep neural network, CNN represents fault location based on convolutional neural network, AA stands for active fault location algorithm, GA stands for greedy fault location algorithm, and FA is a fuzzy fault location set algorithm^[26-27]. From Fig. 6

(a), it can be seen that the fault location based on deep learning is inferior to existing methods in terms of location accuracy. Compared with other fault location algorithms, fault location algorithms based on DNN and CNN have higher accuracy. Comparing with the fault location based on DNN and CNN, we find that the former has higher accuracy.

As shown in Fig. 6(b), compared with traditional fault location algorithms, the location delay of fault location based on DNN is more timely. The fault location delay based on CNN is the second only to the fault location based on DNN. The time difference between the DNN and CNN is not much. The specific reason is that the structural level of the fault location model based DNN is deeper than that of CNN, so the fault location speed has a delay of about 0.1 ms.

5 Conclusions

In this paper, based on huge original data collected from commercial equipment, we propose a standard process flow to build a high-quality dataset. Then the supervised machine learning algorithms CNN and DNN are introduced to analyze the fault reason as an auxiliary for fault location. The evaluation shows that when a dataset is built, this method can effectively improve the quality of the dataset, and DNN is more



▲ Figure 6. Comparison of fault location accuracy and fault location delay between different algorithms

suitable than CNN in application.

References

- [1] RAFIQUE D, VELASCO L. Machine learning for network automation: overview, architecture, and applications [J]. *Journal of optical communications and networking*, 2018, 10(10): D126. DOI: 10.1364/jocn.10.00d126
- [2] BISHOP C M. *Pattern Recognition and Machine Learning* [M]. New York, USA: Springer, 2006
- [3] TALEBI H A, KHORASANI K, TAFAZOLI S. A recurrent neural-network-based sensor and actuator fault detection and isolation for nonlinear systems with application to the satellite's attitude control subsystem [J]. *IEEE transactions on neural networks*, 2009, 20(1): 45 - 60. DOI: 10.1109/TNN.2008.2004373
- [4] CARDOSO G, ROLIM J G, ZURN H H. Identifying the primary fault section after contingencies in bulk power systems [J]. *IEEE transactions on power delivery*, 2008, 23(3): 1335 - 1342. DOI: 10.1109/TPWRD.2008.916743
- [5] FANG H Z, SHI H, DONG Y F, et al. Spacecraft power system fault diagnosis based on DNN [C]//*Prognostics and System Health Management Conference*. IEEE, 2017: 1 - 5. DOI: 10.1109/PHM.2017.8079271
- [6] MUSUMECI F, ROTTONDI C, NAG A, et al. An overview on application of machine learning techniques in optical networks [J]. *IEEE communications surveys & tutorials*, 2019, 21(2): 1383 - 1408. DOI: 10.1109/COMST.2018.2880039
- [7] RUIZ M, FRESI F, VELA A P, et al. Service-triggered failure identification/localization through monitoring of multiple parameters [C]//*The 42nd European Conference on Optical Communication*. ECOC, 2016: 1 - 3
- [8] TEMBO S R, VATON S, COURANT J L, et al. A tutorial on the EM algorithm for Bayesian networks: Application to self-diagnosis of GPON-FTTH networks [C]//*2016 International Wireless Communications and Mobile Computing Conference*. IEEE, 2016: 369 - 376. DOI: 10.1109/IWCMC.2016.7577086
- [9] GOSSELIN S, COURANT J L, TEMBO S R, et al. Application of probabilistic modeling and machine learning to the diagnosis of FTTH GPON networks [C]//*2017 International Conference on Optical Network Design and Modeling*. IEEE, 2017: 1 - 3. DOI: 10.23919/ONDM.2017.7958529
- [10] CHRISTODOULOPOULOS K, SAMBO N, VARVARIGOS E. Exploiting network kriging for fault localization [C]//*Optical Fiber Communication Conference*. OSA, 2016: 1 - 3. DOI: 10.1364/ofc.2016.w1b.5
- [11] VELA A P, RUIZ M, FRESI F, et al. BER degradation detection and failure identification in elastic optical networks [J]. *Journal of lightwave technology*, 2017, 35(21): 4595 - 4604. DOI: 10.1109/JLT.2017.2747223
- [12] VELA A P, SHARIATI B, RUIZ M, et al. Soft failure localization during commissioning testing and lightpath operation [J]. *IEEE/OSA journal of optical communications and networking*, 2018, 10(1): A27 - A36. DOI: 10.1364/JOCN.10.000A27
- [13] SHAHKARAMI S, MUSUMECI F, CUGINI F, et al. Machine-learning-based soft-failure detection and identification in optical networks [C]//*Optical Fiber Communication Conference*. OSA, 2018: 1 - 3. DOI: 10.1364/ofc.2018.m3a.5
- [14] RAFIQUE D, SZYRKOWIEC T, AUTENRIETH A, et al. Analytics-driven fault discovery and diagnosis for cognitive root cause analysis [C]//*Optical Fiber Communication Conference*. OSA, 2018: 1 - 3. DOI: 10.1364/ofc.2018.w4f.6
- [15] ABADI M, BARHAM P, CHEN J, et al. TensorFlow: a system for large-scale machine learning [C]//*The 12th USENIX Conference on Operating Systems Design and Implementation*. USENIX, 2016: 256 - 283
- [16] ZHAO Y L, YAN B Y, LIU D M, et al. SOON: self-optimizing optical networks with machine learning [J]. *Optics express*, 2018, 26(22): 28713. DOI: 10.1364/oe.26.028713
- [17] ZHAO Y L, YAN B Y, LI Z T, et al. Coordination between control layer AI and on-board AI in optical transport networks [J]. *Journal of optical communications and networking*, 2019, 12(1): A49. DOI: 10.1364/jocn.12.000A49
- [18] YAN B Y, ZHAO Y L, RAHMAN S, et al. Dirty-data-based alarm prediction in self-optimizing large-scale optical networks [J]. *Optics express*, 2019, 27(8): 10631. DOI: 10.1364/oe.27.010631
- [19] KIM W, CHOI B, HONG E, et al. A taxonomy of dirty data [J]. *Data mining & knowledge discovery*, 2003, 7(1): 81-99. DOI: 10.1023/A:1021564703268
- [20] WANG B J, ZHAN Y. A survey and performance evaluation on sliding window for data stream [C]//*The 3rd International Conference on Communication Software and Networks*. IEEE, 2011: 654 - 657. DOI: 10.1109/ICC-SN.2011.6014977
- [21] HAN J W, PEI J, YIN Y W. Mining frequent patterns without candidate generation [C]//*The 2000 ACM SIGMOD International Conference on Management of Data*. ACM, 2000. DOI: 10.1145/342009.335372.
- [22] BORGELT C. An implementation of the FP-growth algorithm [C]//*The 1st International Workshop on Open Source Data Mining Frequent Pattern Mining Implementations*. ACM, 2005. DOI: 10.1145/1133905.1133907
- [23] HAN J, MORAGA C. The Influence of the Sigmoid Function Parameters on the Speed of Backpropagation Learning [C]//*From Natural to Artificial Neural Computation*, International Workshop on Artificial Neural Networks. IEEE: 1995.

- [24] NAIR V, HINTON G E. Rectified linear units improve restricted boltzmann machines vinod nair [C]//International Conference on International Conference on Machine Learning. IEEE, 2010
- [25] KRIZHEVSKY A, SUTSKEVER I, HINTON G E. ImageNet classification with deep convolutional neural networks [J]. Communications of the ACM, 2017, 60(6): 84 – 90. DOI: 10.1145/3065386
- [26] HUANG Y, SUN S Y, DUAN X S, et al. A study on deep neural networks framework [C]//The IEEE Advanced Information Management, Communicates, Electronic and Automation Control Conference. IEEE, 2016: 1519 – 1522. DOI: 10.1109/IMCEC.2016.7867471
- [27] LAUZON F Q. An introduction to deep learning [C]//The 11th International Conference on Information Science, Signal Processing and their Applications (ISSPA). IEEE, 2012: 1438 – 1439. DOI: 10.1109/ISSPA.2012.6310529

Biographies

ZHAO Zipiao received the B.S. degree in communication engineering from Hebei University of Engineering, China in 2017. She is currently a Ph.D. candidate of Beijing University of Posts and Telecommunications (BUPT), China. Her research focuses on software defined optical networks and machine learning in optical networks.

ZHAO Yongli (yonglizhao@bupt.edu.cn) received the B.S. degree in commu-

nication engineering and Ph.D. degree in electromagnetic field and microwave technology from Beijing University of Posts and Telecommunications (BUPT), China in 2005 and 2010, respectively. He is currently a professor of the Institute of Information Photonics and Optical Communications, BUPT. From Jan. 2016 to Jan. 2017, he was a visiting associate professor with UC Davis, USA. He has published more than 300 papers in international journals and conference. Since 2015, he has become a senior member of IEEE. His research focuses on software defined optical networking, elastic optical networks, datacenter networking, and optical network security.

YAN Boyuan received the B.S. degree in communication engineering from Beijing University of Posts and Telecommunications (BUPT), China in 2015. He is currently pursuing his Ph.D. degree with BUPT. His research interests include software defined optical networking, service function chaining, and network resource allocation with machine learning.

WANG Dajiang received B.S. and M.S. degrees in mechanical and electronic engineering from East China University of Science and Technology, China, and Shanghai University, China in 1996 and 2001 respectively. By far, he has been working with ZTE Corporation for more than 17 years and persistently doing the job related to OTN intelligent management and control. Now he is the Director of Intelligent Optical Network Product Planning in ZTE and mainly responsible for researching autonomous network architecture and solution on OTN. In total, as the chief author, he has issued more than 60 patents in the fields of WASON, SDON, and AN, most of which had been authorized by CNIPA and USPTO and commercialized in ZTE OTN products. Meanwhile, cooperating with other experts in the field, he has also published more than 20 papers in international influential journals and conferences.



Design of Raptor-Like Rate Compatible SC-LDPC Codes

Abstract: This paper proposes a family of raptor-like rate-compatible spatially coupled low-density parity-check (RL-RC-SC-LDPC) codes from RL-RC-LDPC block codes. There are two important keys. One is the performance of the base matrix. RL-LDPC codes have been adopted in the technical specification of 5G new radio (5G-NR). We use the 5G NR LDPC code as the base matrix. The other is the edge coupling design. In this regard, we have designed a rate-compatible coupling algorithm, which can improve performance under multiple code rates. The constructed RL-RC-SC-LDPC code property requires a large coupling length L and thus we improved the reciprocal channel approximation (RCA) algorithm and proposed a sliding window RCA algorithm. It can provide lower complexity and latency than RCA algorithm. The code family shows improved thresholds close to the Shannon limit and finite-length performance compared with 5G NR LDPC codes for the additive white Gaussian noise (AWGN) channel.

Keywords: SC-LDPC code; 5G NR LDPC code; rate-compatibility; threshold; sliding window RCA algorithm

SHI Xiangyi, HAN Tongzhou, TIAN Hai, ZHAO Danfeng

(College of Information and Communication Engineering, Harbin Engineering University, Harbin 150001, China)

DOI: 10.12142/ZTECOM.2022S1003

<http://kns.cnki.net/kcms/detail/34.1294.TN.20220114.1011.002.html>, published online January 17, 2022

Manuscript received: 2021-06-08

Citation (IEEE Format): X. Y. Shi, T. Z. Han, H. Tian, et al., "Design of raptor-like rate compatible SC-LDPC codes," *ZTE Communications*, vol. 20, no. S1, pp. 16 – 21, Jan. 2022. doi: 10.12142/ZTECOM.2022S1003.

1 Introduction

5G has already been deployed and commercialized on a large scale worldwide. However, with a new round of global technology industry upgrading, the total amount of data that needs to be transmitted is increasing, and new wireless communication technologies still need to be studied to adapt to new application scenarios and higher demands. As one of the most important technologies in physical wireless communication, channel coding is of great significance to improving system reliability^[1].

Spatially coupled low density parity check (SC-LDPC) codes have received widespread attention due to their threshold saturation^[2]. Threshold saturation is the belief propagation (BP) threshold of SC-LDPC codes that approaches the maximum a posteriori (MAP) threshold of their underlying block codes if coupling chain length $L \rightarrow \infty$ ^[3]. There are many results on the optimization of SC-LDPC codes. Ref. [4] introduces a procedure for constructing QC-SC-LDPC codes with a girth of at least eight, and the design leads to improved decod-

ing performance, particularly in the error floor compared with random constructions. Ref. [5] designs time-invariant spatially coupled low-density parity-check (SC-LDPC) codes with a small constraint length and low error floor. This is achieved by eliminating some of the dominant trapping sets (TSs) of the codes.

RC-SC-LDPC codes can adapt to the changing conditions of time-varying channels while allowing transceivers to employ only one encoder/decoder. There are two ways of constructing RC-SC-LDPC codes. One is puncturing^[6]. In a rate-compatible puncturing scheme, the transmitter punctures coded symbols, and as a result of having fewer transmitted code symbols, the code rate is increased. The other is the extension^[7] by selecting a code with a high rate, and constructing a lower code rate by adding check bits. The code with a high bit rate is nested in a lower code. In addition to using the extension and puncturing alone to achieve SC-LDPC code rate compatibility, combining the two methods to design code rate compatibility makes it easier to cover more code rates while ensuring the performance of each code rate.

The raptor-like structure is convenient to achieve rate compatibility, and it has better performance at a low code rate^[8-9]. RL-LDPC codes have been adopted in the technical specifica-

This work is supported in part by ZTE Industry-Academia-Research Cooperation Funds under Grant No. KY10800190067.

tion of 5G new radio due to their excellent performance^[10]. Base matrix performance is one of the key factors affecting the performance of SC-LDPC codes. Thus, we construct RL-RC-SC-LDPC codes by coupling RL-RC-LDPC LDPC codes.

The structure of this paper is as follows. Section 2 introduces the code structure of RL-RC-SC-LDPC codes. In Section 3, the rate-compatible coupling algorithm is described. Then we describe our improved sliding window reciprocal channel approximation (RCA) algorithm based on the RCA algorithm in Section 4. In Section 5, we use the 5G NR LDPC code as the base matrix structure of the SC-LDPC code as an example to analyze the rate-compatible coupling algorithm we proposed. Finally, the conclusions are drawn in Section 6.

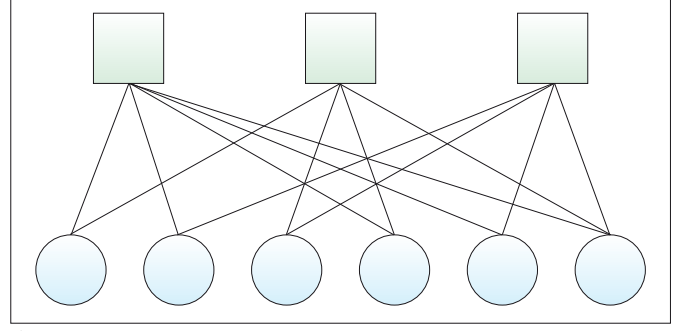
2 RL-RC-SC-LDPC Codes

SC-LDPC codes have a chain structure and are characterized by the following parity check matrix in Eq. (1). It has two characteristics: the coupling chain length L and the coupling depth m_s . L and m_s affect the code rate of SC-LDPC codes. The parity check matrix H_{SC} consists of multiple sub-matrices, and each column contains $m_s + 1$ sub-matrices. The size of the sub-matrix H_0, H_1, \dots, H_{m_s} is the same with $m \times n$, and the size of H_{SC} is $(m_s + L)m \times nL$. If the sub-matrix of each column is the same, it is a time-invariant SC-LDPC code but not time-varying at the same time. Compared with time-varying SC-LDPC codes, time-invariant SC-LDPC codes show a substantial reduction in memory requirements.

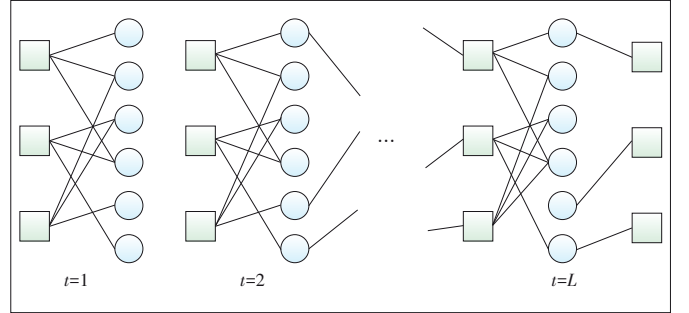
$$H_{SC} = \begin{bmatrix} H_0 & & & & \\ H_1 & H_0 & & & \\ \vdots & H_1 & H_0 & & \\ H_{m_s} & \vdots & H_1 & \ddots & \\ & H_{m_s} & \vdots & \ddots & H_0 \\ & & H_{m_s} & \ddots & H_1 \\ & & & \ddots & \vdots \\ & & & & H_{m_s} \end{bmatrix}_{(m_s + L)m \times nL} \quad (1)$$

SC-LDPC codes can also be represented by Tanner graphs. It is easier to illustrate the coupling process of SC-LDPC codes through Tanner graphs. Take a (2, 4) regular LDPC code as an example, as shown in Fig. 1. The coupling process is to select some variable nodes on the Tanner graph not coupled at the current moment to connect the check nodes on the subsequent m_s Tanner graphs. The generated SC-LDPC code of coupling chain length L is shown in Fig. 2.

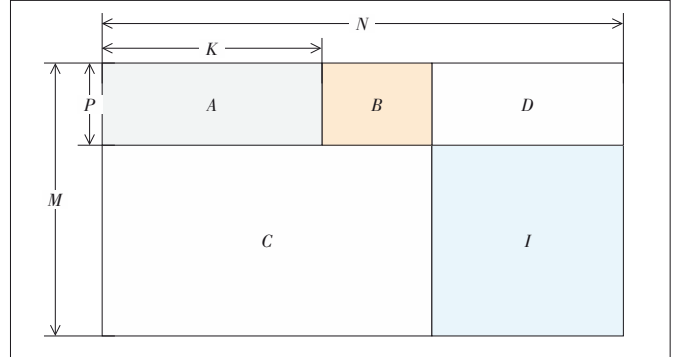
An example of RL-RC-LDPC codes is shown in Fig. 3. The base matrix consists of 5 sub-matrices, namely A , B , C , D and I . The parity check matrix can be constructed from a much smaller sub-matrices A and B , and the other three sub-matrices



▲ Figure 1. (2, 4) regular low density parity check (LDPC) code



▲ Figure 2. (2, 4, L) spatially coupled low-density parity-check (SC-LDPC) code



▲ Figure 3. Raptor-like rate-compatible low-density parity-check (RL-RC-LDPC) codes

ces are extensions. Matrix A corresponds to the information bit, and the size is $P \times K$. Matrix B corresponds to the check digit, which is a square matrix with a double diagonal structure and the size is $P \times P$. Matrix D is an zero matrix, and the size is $P \times (M - P)$. Matrix C is an extended matrix to achieve rate compatibility, the size of which is $(M - P) \times (K + P)$. Matrix I is the identity matrix, and the size is $(M - P) \times (M - P)$. One of the most important features of RL-LDPC codes is that the matrix has a lot of degree-one variable nodes, which are connected to the corresponding check node one by one.

3 Rate-Compatible Coupling Algorithm

The coupling matrix of the RL-RC-SC-LDPC code is generated by coupling the base matrix of the RL-RC-LDPC code.

We designed the coupled matrix sequentially from the parity-check matrix for high code rates to the parity-check matrix for low code rates. In the complete code-rate compatible parity-check matrix, the low code-rate parity-check matrix is obtained by extending the high code-rate parity-check matrix. Therefore, we only couple the extended matrices to construct the low code rate SC-LDPC codes. The coupling relationship in the coupling matrix corresponding to the low code rate includes the coupling relationship in the coupling matrix corresponding to the high code rate. A matrix of RL-RC-LDPC codes is shown in Fig. 4(a). For the matrix $H_k (k = 1, 2, \dots, n)$, H_1 is the highest rate sub-matrix, and H_2, \dots, H_n is the expansion matrix. In the process of edge coupling, we only select the edge for coupling in the matrix $H_k (k = 1, 2, \dots, n)$. We set H_{k0} , H_{k1} and H_k to satisfy the following form:

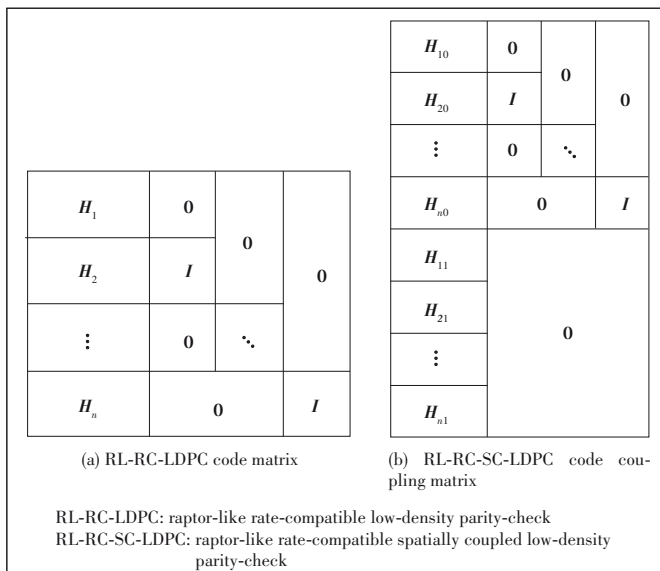
$$H_k = H_{k0} + H_{k1} (k = 1, 2, \dots, n). \quad (2)$$

Eq. (2) means all edges in H_{k0} and H_{k1} originate from H_k . This is set up to maximize performance through coupling without changing the degree distribution.

The complete RL-RC-SC-LDPC code coupling matrix is generated when the parity-check matrix for the lowest code rate is coupled as shown in Fig. 4(b).

Code-rate compatible coupling algorithms need to ensure a good coupling relationship at all code rates. Better coupling at each code rate means better performance benefits at each code rate. Thus, the selection of the side for coupling is more strict. The constraints on the edges selected for coupling are as follows:

- 1) Edges do not couple special structures in H_k ;
- 2) Avoid all zero columns and all zero rows in H_{k0} ;
- 3) According to the check node degree distribution in H_k ,



▲ Figure 4. RL-RC-LDPC code matrix and constructed RL-RC-SC-LDPC code coupling matrix

avoid the edges of check nodes with relatively small coupling degrees.

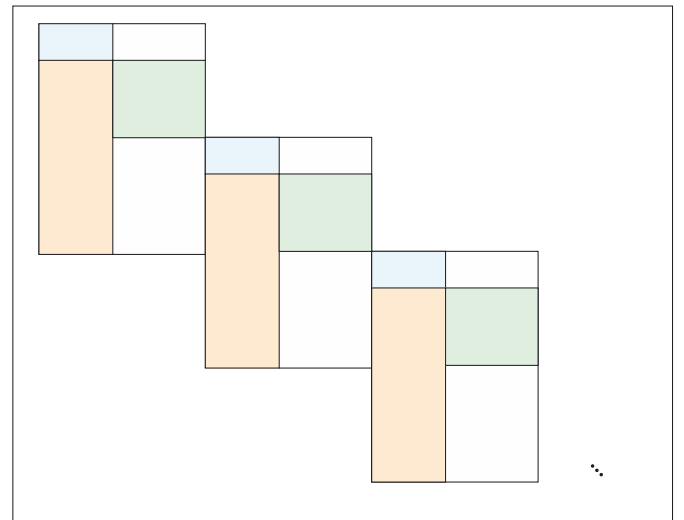
4) Under constraint 3), the edge selection is coupled row by row in H_k , and only one edge is selected in the selected row.

Next, the effect of constraint conditions in the rate-compatible coupling algorithm is explained. To reduce coding complexity, the Raptor-like structure is often used in combination with a double diagonal structure. The double diagonal structure is the key to encoding and in order to encode correctly, the integrity of the double diagonal structure needs to be ensured. It is worth noting that constraint 1) is only for the matrix with the highest rate, and there is no double diagonal structure in other extension matrices. Constraint 2) avoids all-zero columns and all-zero rows in H_{k0} , since their appearance will greatly affect decoding performance. Constraint 3) is to ensure that the selected number of edges is moderate, which will not cause too much error propagation, and will not weaken the coupling relationship. The performance of SC-LDPC will deteriorate if the coupling relationship is weakened. The row-by-row edge selection in constraint 4) is to connect more variable nodes with the next check node in the SC-LDPC code coupling chain under the above constraints, and increase the coupling relationship in the coupling chain to ensure that useful information is transmitted in the coupling chain, thereby improving the performance of the SC-LDPC code.

Finally, the coupling matrix can be expanded by the method of the cyclic permutation matrix, and the expanded coupling matrix can be copied by L and placed according to the definition of SC-LDPC code. Then an SC-LDPC code with coupling chain length L can be generated, the matrix of which is shown in Fig. 5.

4 Sliding Window RCA Algorithm

The RCA algorithm is described in Ref. [11]. Refs. [12 – 13]



▲ Figure 5. Raptor-like rate-compatible spatially coupled low-density parity-check (RL-RC-SC-LDPC) codes

prove that the deviation of RCA from the accurate density evolution threshold is less than 0.01 dB. The RCA algorithm can accurately calculate the threshold of a matrix containing a large number of variable nodes with degree 1. The SC-LDPC code can be considered as an LDPC code with a special structure from the overall check matrix, so the RCA algorithm can also be used to calculate the SC-LDPC code threshold. However, when using the RCA algorithm, due to the special coupling chain structure of the SC-LDPC code, the check matrix is relatively large, and its structural advantages cannot be highlighted. Based on the RCA algorithm, we proposed a sliding window RCA algorithm. The sliding window RCA algorithm can accurately calculate the SC-LDPC code threshold in the case of large L .

Set the signal-to-noise ratio to s_e . e is the edge connecting the variable node and the check node. q_e is the variable node passing information to the check node through edge e . r_e is the check node passing information to the variable node through edge e . E_v is a set of edges connected to variable node v . E_c is a set of edges connected to check node c . For a variable node of degree 1, its value will always be determined by the signal-to-noise ratio of the input channel, independent of the number of iterations. In this case, the overall reliability $Q_v^{(n)}$ of the variable node needs to replace the reliability of the edge. Let T be the stop threshold and f_{RCA} be a binary-valued function. When s_e is higher than the decoding threshold, the value is 1, otherwise, it is 0. Set the sub-matrix size of the constructed SC-LDPC code to $a \times b$. The size of the window is W , and the current sliding times is w . The maximum number of iterations is set to N .

The sliding window RCA algorithm is as follows:

Algorithm 1. sliding window RCA algorithm

1. **if** $w=1$
 - for edges e connected to punctured variable nodes in a sliding window, set $q_e^{(0)} = 0$. For all other edges, set $q_e^{(0)} = s_e$;
- else**
 - edges connecting the 1st to the b -th variable node in the window are initialized to $Q_v^{(n)}$ after the previous window converges. From $b+1$ to Wb variable nodes in the window and edges connected to punctured variable nodes in the sliding window, set $q_e^{(0)} = 0$, for other edges, set $q_e^{(0)} = s_e$.
- end**
2. **for** the number of iterations n ,
 - compute (q_e^n, r_e^n) in the sliding window

$$r_e^{(n)} = \sum_{i \in E_c \setminus e} R(q_i^{(n-1)})$$

$$q_e^{(n)} = q_e^{(0)} + \sum_{i \in E_v \setminus e} R(r_i^{(n)})$$

3. Calculate $Q_v^{(n)}$ for each iteration in the sliding window

$$Q_v^{(n)} = Q_v^{(0)} + \sum_{e \in E_v} R(r_e^{(n)})$$

$$Q_v^{(0)} = \begin{cases} 0 & \text{if } v \text{ is punctured} \\ s_c & \text{otherwise} \end{cases}$$
4. Set the minimum value of $Q^*(n)$ to $Q_v^{(n)}$. At each iteration,
 - if** $w=1$,
 - Count the $Q^*(n)$ of 1 to b variable nodes in the sliding window.
 - else**
 - Count the $Q^*(n)$ of $b+1$ to $2b$ variable nodes in the sliding window.
 - end**
5. **if** $Q^*(n) > T$
 - $f_{RCA} = 1$, slide to the next window until the last window;
 - else**
 - $f_{RCA} = 0$, the number of iterations is increased by 1 until the maximum number of iterations N is reached.
 - end**
- end**

5 Simulation Results

5.1 Comparison with 5G NR LDPC Code Threshold

We use BG_1 in the 5G NR LDPC code as the base matrix to construct the SC-LDPC code and compare the threshold of the 5G NR LDPC code. The coupling chain length L of the constructed SC-LDPC code is 100, using RA termination^[14], corresponding to the base matrix rate 1/3, 2/5, 1/2, 2/3, 3/4, 5/6, and 8/9. The rate losses are 0.002 3, 0.002 5, 0.002 7, 0.002 6, 0.002 4, 0.002 1, and 0.001 8. When using the sliding window RCA algorithm, set the window size to 10, and the iteration number in each window is 250. The threshold results are shown in Table 1.

The coupling chain length L is 100, and a repeat-accumu-

▼ **Table 1.** Threshold results corresponding to the base matrix rate 1/3, 2/5, 1/2, 2/3, 3/4, 5/6, and 8/9

Rate	SC-LDPC Code Threshold/dB	5G NR LDPC Code Threshold/dB	Gap/dB
1/3	-0.338 6	-0.218 8	-0.119 8
2/5	-0.073 1	0.099 4	-0.172 5
1/2	0.353 9	0.450 3	-0.096 4
2/3	1.238 0	1.370 9	-0.132 9
3/4	1.681 4	1.797 0	-0.115 6
5/6	2.350 7	2.439 4	-0.088 7
8/9	3.073 9	3.145 2	-0.071 3

NR: new radio

SC-LDPC: spatially coupled low density parity check

late (RA) method is used to terminate. When the window size is 10, the iteration number in each window is 250. The SC-LDPC code coupling matrix threshold is calculated with \mathbf{BG}_2 as the base matrix and the information bit K_b is 10, corresponding to the base matrix rate 1/5, 1/3, 2/5, 1/2, and 2/3. The rate losses are 0.001 7, 0.002 4, 0.002 7, 0.003, and 0.003 1. The thresholds compared with 5G NR LDPC codes are as follows.

The threshold results for each code rate in Tables 1 and 2 show that the thresholds for the RL-RC-SC-LDPC codes constructed in this paper are closer to the Shannon limit than those for the 5G NR LDPC codes. It is worth noting that this is the threshold value calculated when L is 100. If L continues to be increased, the threshold can approach the Shannon limit further.

5.2. Performance Compared with 5G NR LDPC Codes

In this section, we evaluate the performance of the proposed RL-RC-SC-LDPC codes over the additive white Gaussian noise (AWGN) channel using binary phase shift keying (BPSK) modulation. For decoding, we use sliding window decoding^[15]. When the window size is 2, BP decoding is used in the window, and the number of iterations is 30. 5G NR LDPC code decoding adopts BP decoding and BPSK modulation over the AWGN channel. The number of iterations is 60. We use the SC-LDPC code constructed by the base matrix of the 5G NR LDPC code, which ensures that the number of edges of the 5G NR LDPC code is the same as the number of edges of the coupling matrix of the constructed SC-LDPC code. We set the number of iterations for BP decoding of 5G NR LDPC codes to be the product of the number of iterations in the SC-LDPC code window and the size of the window. This ensures that SC-LDPC codes and 5G NR LDPC codes have the same decoding complexity. We constructed a sub-matrix with an information bit length of 512 bits, which compares performance with 5G NR LDPC codes under 8 rates. The coupling chain length L of the constructed SC-LDPC code is 100, using RA termination.

Fig. 6 shows the bit error ratio (BER) and frame error ratio (FER) simulation curves of the SC-LDPC code with a sub-matrix information bit length of 512 bits and code rates of 1/5, 1/3, 2/5, and 1/2. When the BER is 10^{-5} , it is at least about 0.5 dB better than the 5G NR LDPC code with the same information bit length and rate. When the FER is 10^{-4} , the 5G NR LDPC code with the same information bit length and the same code

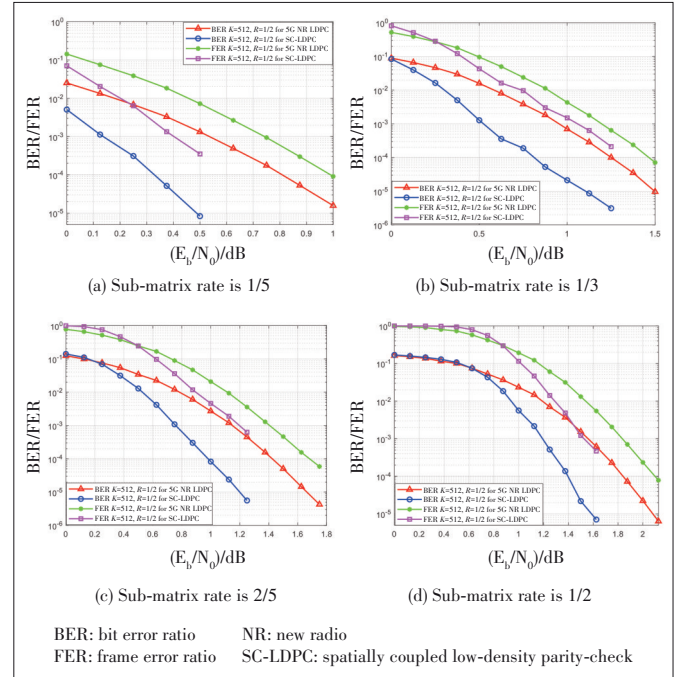
▼ Table 2. Threshold results corresponding to the base matrix rate 1/5, 1/3, 2/5, 1/2, and 2/3

Rate	SC-LDPC Code Threshold/dB	5G NR LDPC Code Threshold/dB	Gap/dB
1/5	-0.724 0	-0.690 3	-0.033 7
1/3	-0.321 1	-0.268 8	-0.052 3
2/5	-0.051 2	0.029 4	-0.080 6
1/2	0.376 3	0.470 3	-0.094 0
2/3	1.261 1	1.310 9	-0.049 8

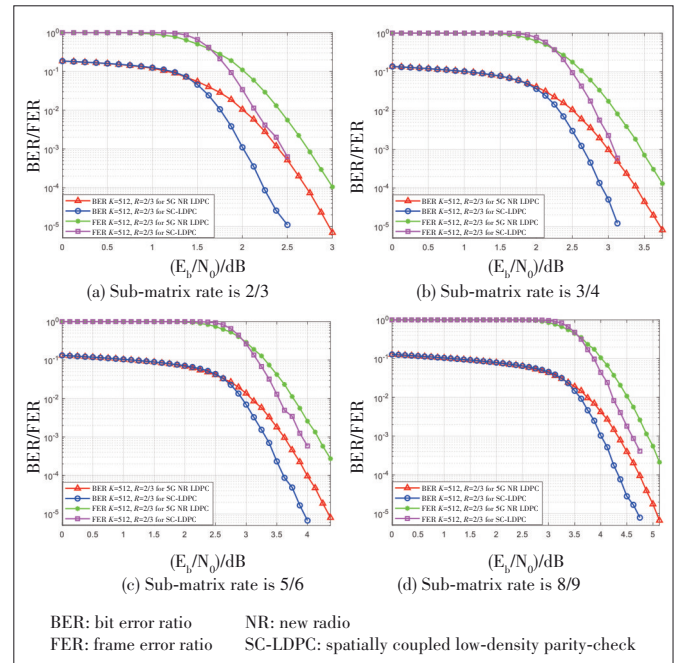
NR: new radio SC-LDPC: spatially coupled low density parity check

rate is at least 0.1 dB and at most 0.3 dB.

Fig. 7 shows the BER and FER simulation curves of the SC-LDPC code with a sub-matrix information bit length of 512 bits and code rates of 2/3, 3/4, 5/6 and 8/9. When the BER is 10^{-5} , the 5G NR LDPC code with the same information bit length and the same code rate is at least 0.1 dB and at most 0.4 dB. When the FER is 10^{-4} , the 5G NR LDPC code with the same information bit length and the same code rate is at least 0.1 dB and at most 0.3 dB.



▲ Figure 6. Performance comparison under 4 rates of 1/5, 1/3, 2/5, and 1/2



▲ Figure 7. Performance comparison under 4 rates of 2/3, 3/4, 5/6, and 8/9

The analysis above shows that the RL-RC-SC-LDPC code proposed in this paper has a significant performance gain compared with the 5G NR LDPC code, indicating that the rate-compatible coupling algorithm proposed in this paper has certain advantages.

6 Conclusions

In this paper, we propose a family of RL-RC-SC-LDPC codes from RL-RC-LDPC block codes. We have designed a rate-compatible coupling algorithm, which can improve performance under multiple code rates. We use the 5G NR LDPC code as the base matrix, and construct the RL-RC-SC-LDPC code through the coupling algorithm proposed in this paper. The simulation results show that the performance of the SC-LDPC code we designed can surpass the 5G NR LDPC code under the same parameters. To calculate the RL-RC-SC-LDPC code threshold with a large L , we improve the RCA algorithm and propose a sliding window RCA algorithm. The code family shows improved thresholds close to the Shannon limit to 5G NR LDPC codes for the AWGN channel.

References

- [1] VENUGOPAL T, RADHIKA S. A survey on channel coding in wireless networks [C]//2020 International Conference on Communication and Signal Processing (ICCSP). IEEE, 2020: 0784 - 0789. DOI: 10.1109/ICCSP48568.2020.9182213
- [2] KUDEKAR S, RICHARDSON T J, URBANKE R L. Threshold saturation via spatial coupling: Why convolutional LDPC ensembles perform so well over the BEC [J]. IEEE transactions on information theory, 2011, 57(2): 803 - 834. DOI: 10.1109/TIT.2010.2095072
- [3] SCHLÜTER M, HASSAN N U, FETTWEIS G P. On the construction of protograph based SC-LDPC codes for windowed decoding [C]//IEEE Wireless Communications and Networking Conference (WCNC). IEEE, 2018: 1 - 6. DOI: 10.1109/WCNC.2018.8377289
- [4] MO S Y, CHEN L, COSTELLO D J, et al. Designing protograph-based quasi-cyclic spatially coupled LDPC codes with large girth [J]. IEEE transactions on communications, 2020, 68(9): 5326 - 5337. DOI: 10.1109/TCOMM.2020.3001029
- [5] NASERI S, BANIHASHEMI A H. Spatially coupled LDPC codes with small constraint length and low error floor [J]. IEEE communications letters, 2020, 24(2): 254 - 258. DOI: 10.1109/LCOMM.2019.2955450
- [6] LIU K K, EL-KHAMY M, LEE J. Finite-length algebraic spatially-coupled quasi-cyclic LDPC codes [J]. IEEE journal on selected areas in communications, 2016, 34(2): 329 - 344. DOI: 10.1109/JSAC.2015.2504273
- [7] HOU W, LU S, CHENG J. Rate-compatible spatially coupled LDPC codes via repeat-accumulation extension [C]//The 8th International Symposium on Turbo Codes and Iterative Information Processing (ISTC). IEEE, 2014: 87 - 91. DOI: 10.1109/ISTC.2014.6955091
- [8] ZHANG Y S, PENG K W, CHEN Z M, et al. Progressive matrix growth algorithm for constructing rate-compatible length-scalable raptor-like quasi-cyclic LDPC codes [J]. IEEE transactions on broadcasting, 2018, 64(4): 816 - 829. DOI: 10.1109/TBC.2017.2781137
- [9] CHEN T Y, DIVSALAR D, WANG J D, et al. Protograph-based raptor-like LDPC codes for rate compatibility with short blocklengths [C]//IEEE Global Telecommunications Conference. IEEE, 2011: 1 - 6. DOI: 10.1109/GLOCOM.2011.6134051
- [10] LI H A, BAI B M, MU X J, et al. Algebra-assisted construction of quasi-cyclic LDPC codes for 5G new radio [J]. IEEE access, 2018, 6: 50229 - 50244. DOI: 10.1109/ACCESS.2018.2868963
- [11] CHEN T Y, VAKILINIA K, DIVSALAR D, et al. Protograph-based raptor-like LDPC codes [J]. IEEE transactions on communications, 2015, 63(5): 1522 - 1532. DOI: 10.1109/TCOMM.2015.2404842
- [12] CHUNG S Y. On the construction of some capacity-approaching coding schemes [D]. Cambridge, USA: Massachusetts Institute of Technology, 2000
- [13] DIVSALAR D, DOLINAR S, JONES C R, et al. Capacity-approaching protograph codes [J]. IEEE journal on selected areas in communications, 2009, 27(6): 876 - 888. DOI: 10.1109/JSAC.2009.090806
- [14] MA J Y, SI Z W, HE Z Q. An efficient structure for terminating spatially coupled LDPC codes [C]//IEEE China Summit and International Conference on Signal and Information Processing (ChinaSIP). IEEE, 2015: 968 - 971. DOI: 10.1109/ChinaSIP.2015.7230548
- [15] PAPALEO M, IYENGAR A R, SIEGEL P H, et al. Windowed erasure decoding of LDPC Convolutional Codes [C]//2010 IEEE Information Theory Workshop on Information Theory. IEEE, 2010: 1 - 5. DOI: 10.1109/ITW-KSPS.2010.5503166

Biographies

SHI Xiangyi (shixiangyi@hrbeu.edu.cn) received his B.E. degree in electronic information science and technology from Shanxi University, China in 2018. He is currently pursuing his M.E. with College of Information & Communication Engineering, Harbin Engineering University, China. His research interests include channel coding for wireless communications

HAN Tongzhou received his B.E. degree in communication engineering from Shandong University, China in 2014. He is currently pursuing the Ph.D. degree in information and communication engineering with Harbin Engineering University, China. His research interests include wireless communication, channel coding, and massive MIMO networks.

TIAN Hai received his B.E. degree in communication engineering from Harbin Engineering University, China in 2014. He is currently pursuing his Ph.D. degree with College of Information & Communication Engineering, Harbin Engineering University. His research interests include channel coding for wireless communications and joint source channel coding (JSCC) schemes for deep space communication.

ZHAO Danfeng received his Ph.D. degree in communication systems from Harbin Engineering University, China in 2006. He is currently a professor at Harbin Engineering University. His research interests include network coding, underwater acoustic sensor networks, high performance coding, and modulation.



Derivative-Based Envelope Design Technique for Wideband Envelope Tracking Power Amplifier with Digital Predistortion

Abstract: A novel envelope design for an envelope tracking (ET) power amplifier (PA) based on its derivatives is proposed, which can trade well off between bandwidth reduction and tracking accuracy. This paper theoretically analyzes how to choose an envelope design that can track the original envelope closely and reduce its bandwidth, and then demonstrates an example to validate this idea. The generalized memory polynomial (GMP) model is applied to compensate for the nonlinearity of ET PA with the proposed envelope design. Experiments are carried out on an ET system that is operated with the center frequency of 3.5 GHz and excited by a 20 MHz LTE signal, which show that the proposed envelope design can make a good trade-off between envelope bandwidth and efficiency, and satisfactory linearization performance can be realized.

Keywords: bandwidth reduction; envelope tracking; shaping function; supply modulator

YI Xueya¹, CHEN Jixin¹, CHEN Peng¹,
NING Dongfang², YU Chao¹

(1. State Key Laboratory of Millimeter Waves,
Southeast University, Nanjing 210096, China;
2. ZTE Corporation, Shenzhen 518057, China)

DOI: 10.12142/ZTECOM.2022S1004

<http://kns.cnki.net/kcms/detail/34.1294.TN.20220113.1631.002.html>, published online
January 14, 2021

Manuscript received: 2021-05-12

Citation (IEEE Format): X. Y. Yi, J. X. Chen, P. Chen, et al., "Derivative-based envelope design technique for wideband envelope tracking power amplifier with digital predistortion," *ZTE Communications*, vol. 20, no. S1, pp. 22 - 26, Jan. 2022. doi: 10.12142/ZTECOM.2022S1004.

1 Introduction

In the fifth-generation communication systems (5G), complex modulated signals with high peak-to-average power ratio (PAPR) and wide bandwidth (BW) are applied to increase the spectrum utilization and data transmission rate^[1-2]. However, a high PAPR leads to more challenges in efficiency and linearity. The envelope tracking (ET) technique is a promising candidate to improve the efficiency of the power amplifier (PA)^[3-4].

In ET architecture, the supply modulator adjusts the drain voltage of the PA for signals according to input power, by which the PA is always working at a saturated state. Unfortunately, the envelope of the radio frequency (RF) signal cannot be directly used as the input of the supply modulator. On the one hand, the envelope of the RF signal usually has a bandwidth of four times to eight times the original modulated band-

width, placing high challenges on the design of the supply modulator. Thus the bandwidth reduction of the envelope is required. On the other hand, since the PA cannot operate when the drain voltage is below the knee voltage, the envelope signal needs to be mapped to a voltage value for the PA^[5]. Therefore, a proper envelope design should be applied before the envelope of the RF signal enters the supply modulator.

Several techniques for reducing the bandwidth of the envelope signal have been proposed to meet the requirements of the supply modulator. A method to limit the slew rate of the envelope was discussed in Ref. [6], and low-pass filters were applied in Refs. [7 - 8] to narrow the bandwidth of the envelope. In real applications, these methods need memory blocks and then introduce additional information to the original envelope, which places more challenges on digital predistortion. Several shaping functions also track the envelope closely and reduce its bandwidth to a constant without memory blocks. N6 was applied in Refs. [5, 7, 9 - 10] to make a good trade-off between linearity and efficiency of ET PA. Besides, the Wilson function^[11-12] and power envelope tracking (PET)^[13] technique can also reduce the envelope bandwidth to a certain value at a cost of efficiency degradation.

This work was supported in part by the National Natural Science Foundation of China (NSFC) under Grant No. 62022025, in part by the Natural Science Foundation of Jiangsu Province under Grant No. BK20200065, and in part by ZTE Industry-University-Institute Cooperation Funds under Grant No. HC-CN-20191121016.

Taking considerations on both bandwidth reduction and shaping function, this paper proposes a novel technique to establish envelope design based on the derivatives of envelope functions, by which a trade-off can be made between the bandwidth and the tracking accuracy of the envelope. An example is demonstrated to verify the proposed idea. Furthermore, the corresponding digital predistortion is employed to compensate for the nonlinearity of the envelope tracking power amplifier with this method.

2 Envelope Analysis

The efficiency of ET PA is usually the product of the efficiency of the supply modulator and that of PA. However, an envelope with a bandwidth wider than the one of the supply modulator degrades the efficiency of the supply modulator. Generally, the closer the shaping function tracks the original envelope, the higher the efficiency of the PA is. Therefore, an envelope design always has two characteristics: 1) It can effectively reduce the bandwidth of envelope; 2) it tracks the envelope closely.

1) Reducing the bandwidth of the envelope

An envelope design $f(|x|)$ can be expressed in Taylor expansion at zero as follows.

$$f(|x|) = f(0) + f'(0) \cdot |x| + \frac{f''(0)}{2} \cdot |x|^2 + \dots + \frac{f^n(n)}{n!} \cdot |x|^n, \quad n = \infty. \quad (1)$$

Here, x represents the baseband signal whose bandwidth is B_{RF} . The bandwidth of $|x|$ is theoretically infinite because of the absolute sign. And $|x|^2$ can be expressed as

$$|x|^2 = x \cdot x^*, \quad (2)$$

whose bandwidth is $B_{RF}^{[13]}$. Therefore, the odd order of the envelope is infinite, while the even order of the envelope is finite. It can be inferred that it is a necessary condition for $f(|x|)$ that $f'(0)$ equals zero to effectively reduce the bandwidth of the original envelope.

2) Tracking the envelope closely

The de-trough envelope can convert the original envelope above the knee voltage and simultaneously track it most closely. But the non-smoothness of de-trough function curve derivative widens the bandwidth of envelope and brings strong nonlinearity. Therefore, a smooth envelope design is desirable, whose curve is close to the de-trough function. It can also be inferred that if a function is close to the de-trough function, its derivative is also close to that of the de-trough function.

In summary, a smooth envelope design is desired, whose derivative at zeros equals zero and whose derivative is close to that of the de-trough function. In the next section, the pro-

posed envelope design will be analyzed based on its derivatives and followed by an example.

3 Proposed Method

3.1 Envelope Design with Monotonous Derivative

In Fig. 1, the red solid lines are an objective monotonous envelope design and its derivative, and the blue dotted lines represent the de-trough function and its derivative. It should be noted that the $f(|x|)$ and $|x|$ in Fig. 1(a) represent the normalized drain voltage and original envelope in the envelope tracking application, respectively. There are two points of intersection (also tendency) of $f(|x|)$ and the de-trough function, which are at $(0, V_{min})$ and $(1, 1)$. In such a situation, the envelope design can be deduced by:

$$f(0) = V_{min}; f'(0) = 0; f(1) = 1; f'(1) = 1. \quad (3)$$

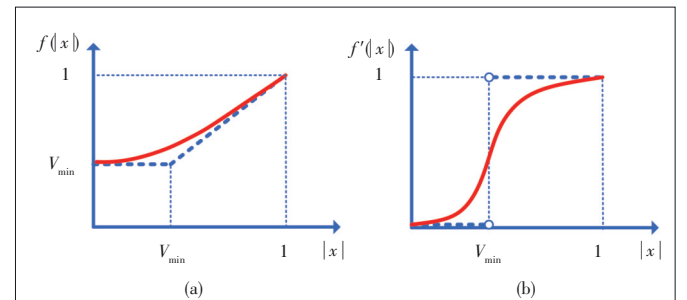
From the aspect of the envelope bandwidth, when the derivative of the envelope design equals that of the de-trough function, the envelope design equals the de-trough function, which converts the bandwidth of envelope to infinite. When the derivative is a straight line from $(0, 0)$ to $(1, 1)$, it can be deduced that

$$f'(|x|) = |x| \Rightarrow f(|x|) = \int |x| d|x| = 0.5 \cdot |x|^2 + c \Rightarrow BW = B_{RF}. \quad (4)$$

It can reduce the envelope bandwidth to B_{RF} . Therefore, the envelope design with monotonous derivative can realize the envelope bandwidth from B_{RF} to infinite, theoretically.

From the aspect of the tracking accuracy, when the normalized V_{min} is less than 0.5, this envelope design brings poor tracking accuracy if the derivative curvature is small, because the following inequality holds if the last three equations in Eq. (3) are satisfied. To validate this method, an example is demonstrated in the next section.

$$f(0) = 1 - \int_0^1 f'(|x|) d|x| > V_{min}. \quad (5)$$



▲ Figure 1. Proposed envelope design with monotonous derivative: (a) envelope design; (b) monotonous derivative

3.2 Example for Validation

The trend of the sigmoid function is consistent with that of the derivative of the de-trough function. Therefore, the sigmoid function can be applied as the origin of the derivative of objective function, which can be expressed as

$$f'(|x|) = \frac{1}{a + e^{-s \cdot |x| - d}} + b. \quad (6)$$

Then, its indefinite integral, which is also the objective envelope design, is

$$f(|x|) = \left(\frac{1}{a} + b\right) \cdot |x| + \frac{1}{a \cdot s} \cdot \ln(a + e^{-s \cdot |x| - d}) + c. \quad (7)$$

There are five degrees of freedom in Eq. (7), but only four equations in Eq. (3). Thus, a unique envelope design $f(|x|)$ can be derived for different values of s that controls the curvature of $f'(|x|)$. In the rest of this paper, Eq. (7) will be mentioned as the S function. It should be noted that the S function equals the de-trough function when $s=\infty$.

Although the normalized V_{\min} differs from the performance of the supply modulator, it is generally less than 0.5 in order to maintain high efficiency. In order to verify the proposed envelope design, we apply it to map the envelope of an LTE signal with 20 MHz bandwidth to 12 – 28 V.

Figs. 2(a) and 2(b) show the S function and its derivative for $s=3$ and $s=10$ when the envelope swings from 12 V to 28 V, respectively. Figs. 2(c) and 2(d) present the time domain wave-

form and normalized power spectral density (PSD) of the proposed envelope while $s=3$ and $s=10$. In this paper, the effective bandwidth is defined as the frequency where the PSD falls below -50 dBc from the main lobe. Table 1 presents the bandwidth and normalized mean square error (NMSE) of the proposed envelope for different values of s and traditional envelopes. It can be seen that the S function can make a good trade-off between bandwidth and tracking accuracy when the bandwidth is greater than $1.6 \times B_{RF}$. Compared with Wilson, second-order PET and N6 envelopes, the S envelope can reach similar tracking accuracy under the same envelope bandwidth. According to Eq. (5), if $s < 3$, the bandwidth of the proposed envelope will be further reduced, but the tracking accuracy will be degraded a lot because $f(0) > V_{\min}$.

4 Digital Predistortion

The proposed envelope design contains the information of the original envelope and does not introduce additional information. Therefore, this envelope tracking power amplifier can be described by a single-input single-output (SISO) behavioral model. To compensate the nonlinearity, the generalized memory polynomial (GMP)^[14] is applied in this paper, which can be written as

$$y_{GMP}(n) = \sum_{k=0}^{K_a-1} \sum_{l=0}^{L_a-1} a_{kl} x(n-1) |(n-1)|^k + \sum_{k=1}^{K_b} \sum_{l=0}^{L_b-1} \sum_{m=1}^{M_b} b_{klm} x(n-1) |(n-l-m)|^k + \sum_{k=1}^{K_c} \sum_{l=0}^{L_c-1} \sum_{m=1}^{M_c} c_{klm} x(n-1) |(n-l+m)|^k, \quad (8)$$

where $x(n)$ represents the input signal; K_a and L_a are the nonlinearity order and memory depth for aligned signals and envelope; K_b and L_b are the nonlinearity order, memory depth for signal and lagging envelopes; K_c and L_c are the nonlinearity order, memory depth for signals and leading envelopes; M_b and M_c are the maximum depth of the lagging and leading cross-terms, respectively.

5 Experimental Results

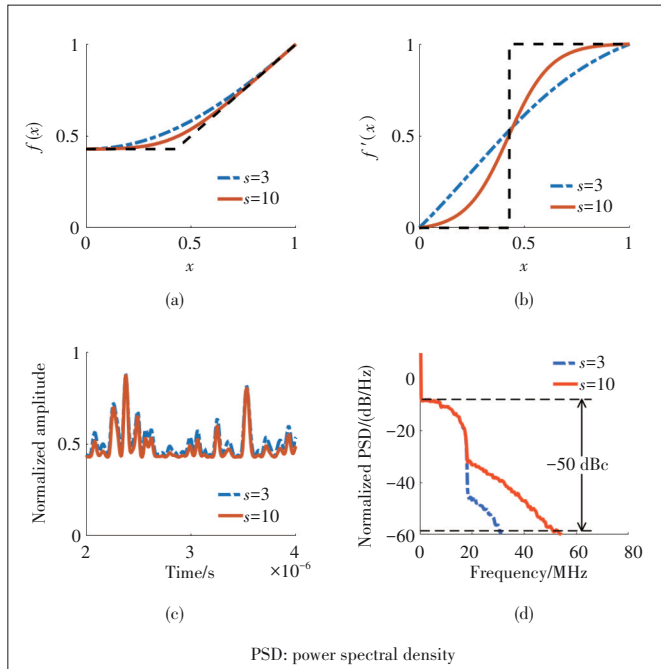
5.1 Test Bench

The proposed shaping functions and corresponding digital predistortion were demonstrated in the test bench, as shown in

▼ Table 1. Bandwidth and NMSE of the S envelope and traditional envelopes

Parameter	S Envelope				Traditional Envelopes		
	$s=3$	$s=5$	$s=10$	$s=16$	Wilson	2.ord.PET	N6
BW	1.6×	2.1×	2.6×	3.0×	1.6×	1.6×	3.0×
NMSE/dB	-6.8	-7.0	-7.7	-7.9	-6.6	-6.7	-7.9

BW: bandwidth NMSE: normalized mean square error

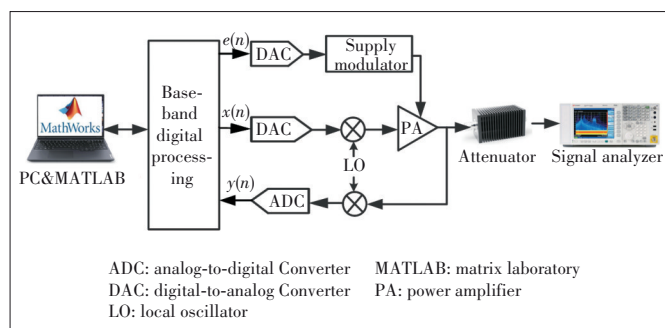


▲ Figure 2. Example of the proposed envelope design: (a) envelope design; (b) derivative of the S function for $s=3$ and $s=10$; (c) time domain waveforms; (d) normalized power spectral density of the S envelope

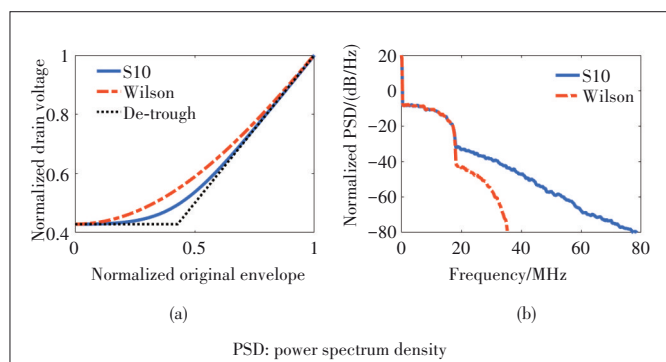
Fig. 3. Restricted by the bandwidth and swing range of the supply modulator, the test signal is a 20 MHz LTE signal, and the envelope swings from 12 V to 28 V. The average PA output is at 37.2 dBm in this experiment. Firstly, a 20 MHz LTE signal with the PAPR of 7.6 dB and its shaped envelope were generated by the MATLAB in PC, then downloaded into the baseband digital processing module. This baseband digital signal was converted to an analog signal and up-converted to 3.5 GHz, and then fed into the input port of ET PA. Meanwhile, the envelope signal went through the digital-to-analog converter (DAC), linearly amplified by the supply modulator, and then fed into the drain of PA. The output of PA was down-converted to baseband and converted to a digital signal, and then used to model PA in PC. In this experiment, the S function with $s=10$ was applied to map the envelope to 12 - 28 V, which will be mentioned as S10 function.

5.2 Validation for Proposed Method

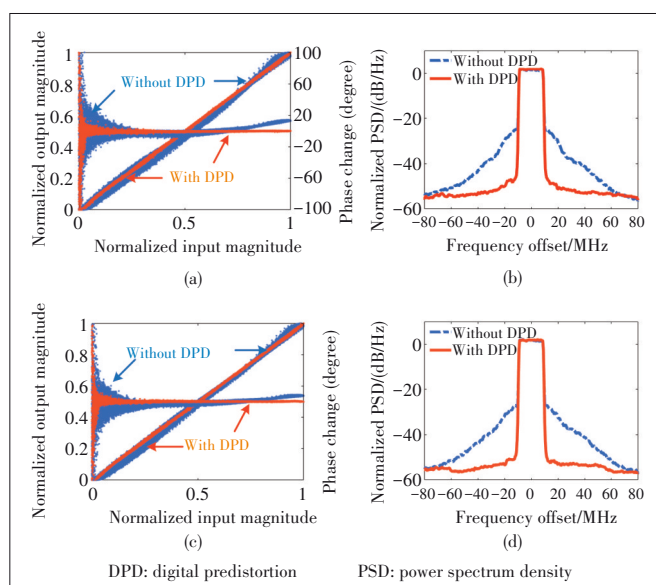
Because the envelope swing rang is 12 – 28 V, the normalized V_{\min} is 12/28. It can be deduced from Eqs. (3) and (7) that a , b , c and d of the S function are 0.98, -0.01 , 0 and -4.21 when $s=10$. In this experiment, the S10 function is compared with the Wilson function. As shown from Figs. 4(a) and 4(b), the S10 envelope tracks more closely than the Wilson envelope, while it has wider bandwidth. Figs. 5(a) and 5(b) present the amplitude-modulation to amplitude-modulation (AM/AM) curve, amplitude-modulation to phase-modulation (AM/PM)



▲ **Figure 3. Test bench setup**



▲ Figure 4. Experiment for validation: (a) plot of samples of the S10 and Wilson envelopes versus the original envelope; (b) normalized power spectrum density of the S10 and Wilson envelopes



▲ **Figure 5. Comparison experiment: (a) amplitude-modulation to amplitude-modulation (AM/AM) and amplitude-modulation to phase-modulation (AM/PM) curves; (b) normalized PSD without and with DPD under S10 function; (c) AM/AM and AM/PM curves; (d) normalized PSD without and with DPD under Wilson function**

curve and the measured normalized output power spectra density without and with digital predistortion (DPD) for the S10. While Figs. 5(c) and 5(d) show these for the Wilson. It can also be seen from Table 2 that the ET system with the S10 has higher efficiency and stronger nonlinearity than the Wilson, and the GMP model can effectively compensate for its nonlinearity. For the S10, the adjacent channel leakage ratios (ACLRs) and NMSE can be reduced to $-51.2/-51.8$ dBc and -38.5 dB, respectively. For Wilson, these values can be reduced to $-54.0/-54.3$ dBc and -40.5 dB.

6 Conclusions

In this paper, a novel envelope design based on the derivatives is theoretically analyzed and validated. The analysis shows that the envelope design with monotonous derivatives is valid within a wide range of envelope bandwidth. This method provides more flexibility for the choice of envelope designs under different requirements of the supply modulator. The corresponding digital predistortion is also validated to compensate for the PA nonlinearity. In the era of 5G and beyond, the pro-

▼ Table 2. Efficiency and nonlinearity performance of the measured ET system

Shaping Function	Efficiency/%	Without DPD		With DPD	
		ACLRs/dBc (± 20 MHz)	NMSE/dB	ACLRs/dBc (± 20 MHz)	NMSE/dB
S10	43.8	-31.3/-31.6	-21.2	-51.2/-51.8	-38.5
Wilson	42	-33.3/-33.5	-23.6	-54.0/-54.3	-40.5

ACLR: adjacent channel leakage ratio
 DPD: digital predistortion

ET: envelope tracking
NMSE: normalized mean square error

posed approach provides a promising solution for wideband ET applications.

References

- [1] GILBERT P L, MONTOTORO G, VEGAS D, et al. Digital predistorters go multidimensional: DPD for concurrent multiband envelope tracking and outphasing power amplifiers [J]. *IEEE microwave magazine*, 2019, 20(5): 50 – 61. DOI: 10.1109/mm.2019.2898021
- [2] MA J G. RF Front-End Designs of MIMO Systems for 5G and Beyond [J]. *ZTE technology journal*, 2020, 26(4): 50-576. DOI: 10.12142/ZTETJ.202004012
- [3] ASBECK P, POPOVIC Z. ET comes of age: envelope tracking for higher-efficiency power amplifiers [J]. *IEEE microwave magazine*, 2016, 17(3): 16 – 25. DOI: 10.1109/mm.2015.2505699
- [4] WU R L, LI Y, LIE Y C. Design technologies for silicon-based high-efficiency RF power amplifiers: a brief overview [J]. *ZTE communications*, 2011, 9(3): 28 – 35
- [5] KWAN A, YOUNES M, DARRAGI R, et al. On track for efficiency: concurrent multiband envelope-tracking power amplifiers [J]. *IEEE microwave magazine*, 2016, 17(5): 46 – 59. DOI: 10.1109/mm.2016.2525118
- [6] MONTOTORO G, GILBERT P L, BERTRAN E, et al. A method for real-time generation of slew-rate limited envelopes in envelope tracking transmitters [C]// *IEEE International Microwave Workshop Series on RF Front-ends for Software Defined and Cognitive Radio Solutions (IMWS)*. IEEE, 2010. DOI: 10.1109/IMWS.2010.5441005
- [7] JEONG J, KIMBALL D F, KWAK M, et al. Wideband envelope tracking power amplifiers with reduced bandwidth power supply waveforms and adaptive Digital predistortion techniques [J]. *IEEE transactions on microwave theory and techniques*, 2009, 57(12): 3307 – 3314. DOI: 10.1109/tmtt.2009.2033298
- [8] YI X Y, CHEN J X, LI H T, et al. Integrated bandwidth reduction and shaping technique for wideband millimeter wave envelope tracking power amplifier with digital predistortion [C]// *International Wireless Symposium (IWS)*. IEEE, 2020. DOI: 10.1109/IWS49314.2020.9360052
- [9] KWAN A K, YOUNES M, HAMMI O, et al. Linearization of a highly nonlinear envelope tracking power amplifier targeting maximum efficiency [J]. *IEEE microwave and wireless components letters*, 2017, 27(1): 82 – 84. DOI: 10.1109/lmwc.2016.2629983
- [10] HAMMI O, KHALIFA M O, ABDELHAFIZ A, et al. A dual-input two-box model for digital predistortion of envelope tracking power amplifiers [J]. *IEEE microwave and wireless components letters*, 2016, 23(5): 361 – 363. DOI: 10.1109/Lmwc.2016.2548984
- [11] GILOVANNELLI N, VLASITS T, CIDRONALI A, et al. Efficiency and linearity enhancements with envelope shaping control in wideband envelope tracking GaAs PA [C]// *International Workshop on Integrated Nonlinear Microwave and Millimetre-Wave Circuits (INMMIC)*. IEEE, 2011. DOI: 10.1109/INMMIC.2011.5773331
- [12] WANG Z C. *Envelope tracking power amplifiers for wireless communications* [M]. London, England: Artech House, 2014: 216 – 224
- [13] OLAVSBRAATEN M, GECAN D. Bandwidth reduction for supply modulated RF PAs using power envelope tracking [J]. *IEEE microwave and wireless components letters*, 2017, 27(4): 374 – 376. DOI: 10.1109/lmwc.2017.2679046
- [14] MORGAN D R, MA Z X, KIM J, et al. A generalized memory polynomial model for digital predistortion of RF power amplifiers [J]. *IEEE transactions on signal processing*, 2006, 54(10): 3582 – 3860. DOI: 10.1109/tsp.2006.879264

Biographies

YI Xueya received the B.E. degree in electronic and information engineering from Xidian University, China in 2018. She is currently pursuing the M.E. degree in electromagnetic fields and microwave technology at the State Key Laboratory of Millimeter Waves, Southeast University, China. Her current research interests include bandwidth reduction and shaping of envelope and digital predistortion for wideband envelope tracking power amplifiers.

CHEN Jixin received the B.S. degree in radio engineering from Southeast University, China in 1998, and the M.S. and Ph.D. degrees from Southeast University in 2002 and 2006, respectively, all in electromagnetic field and microwave technique. Since 1998, he has been with the State Key Laboratory of Millimeter Waves, Southeast University. He is currently a professor with the School of Information Science and Engineering and Director of the Department of Electromagnetic Field and Microwave Engineering. His research interests include microwave and millimeter-wave circuit design and monolithic microwave integrated circuit (MMIC) design. Dr. CHEN is the winner of 2016 Keysight Early Career Professor Award and 2016 National Natural Science Prize Second Prize. He has served as TPC Chair of RFT2019, and TPC Co-Chair of HSC2012 and UCM2012.

CHEN Peng received the B.E. degree in communication engineering and the M.E. degree in electronic engineering from Harbin Institute of Technology, China in 2010 and 2012, respectively, and the Ph.D. degree in electronic engineering from University College Dublin, Ireland in 2016. From 2017 to 2020, he was a research associate with Centre for High Frequency Engineering, Cardiff University, UK. Since 2020, he has been with the State Key Laboratory of Millimeter Waves and is currently a lecturer with the School of Information Science and Engineering, Southeast University, China. His current research interests include the design and optimization of high-efficiency power amplifiers.

NING Dongfang received the M.S. and Ph.D. degrees in control science and engineering from Northwestern Polytechnical University, China in 2016 and 2019. He is currently a senior RF algorithm architect in ZTE Corporation, working in nonlinear system behavioral modeling and linearization for wireless and RF systems.

YU Chao (chao.yu@seu.edu.cn) received the B.E. degree in information engineering, the M.E. degree in electromagnetic fields and microwave technology from Southeast University (SEU), China in 2007 and 2010, respectively, and the Ph.D. degree in electronic engineering from University College Dublin, Ireland in 2014. He is currently a professor with the State Key Laboratory of Millimeter Waves, School of Information Science and Engineering, SEU. His research interest includes microwave and millimeter wave power amplifier modeling and linearization, and 5G massive MIMO RF system design.



End-to-End Chinese Entity Recognition Based on BERT-BiLSTM-ATT-CRF

Abstract: Traditional named entity recognition methods need professional domain knowledge and a large amount of human participation to extract features, as well as the Chinese named entity recognition method based on a neural network model, which brings the problem that vector representation is too singular in the process of character vector representation. To solve the above problem, we propose a Chinese named entity recognition method based on the BERT-BiLSTM-ATT-CRF model. Firstly, we use the bidirectional encoder representations from transformers (BERT) pre-training language model to obtain the semantic vector of the word according to the context information of the word; Secondly, the word vectors trained by BERT are input into the bidirectional long-term and short-term memory network embedded with attention mechanism (BiLSTM-ATT) to capture the most important semantic information in the sentence; Finally, the conditional random field (CRF) is used to learn the dependence between adjacent tags to obtain the global optimal sentence level tag sequence. The experimental results show that the proposed model achieves state-of-the-art performance on both Microsoft Research Asia (MSRA) corpus and people's daily corpus, with F1 values of 94.77% and 95.97% respectively.

Keywords: named entity recognition (NER); feature extraction; BERT model; BiLSTM; attention mechanism; CRF

LI Daiyi¹, TU Yaofeng², ZHOU Xiangsheng², ZHANG Yangming², MA Zongmin¹

(1. Nanjing University of Aeronautics and Astronautics, Nanjing 211106, China;
2. ZTE Corporation, Shenzhen 518057, China)

DOI: 10.12142/ZTECOM.2022S1005

<http://kns.cnki.net/kcms/detail/34.1294.tn.20220119.1630.002.html>, published online January 20, 2022

Manuscript received: 2021-01-13

Citation (IEEE Format): D. Y. Li, Y. F. Tu, X. S. Zhou, et al., "End-to-end chinese entity recognition based on BERT-BiLSTM-ATT-CRF," *ZTE Communications*, vol. 20, no. S1, pp. 27 – 35, Jan. 2022. doi: 10.12142/ZTECOM.2022S1005.

1 Introduction

Named entity recognition (NER) is one of the key technologies in natural language text data processing. Its main function is to identify specific types of entities from unstructured text data, such as person names, place names, organization names and domain-specific words. At present, NER is widely used in information extraction, knowledge graph construction, machine translation and intelligent question answering. The best performance of traditional methods is based on statistical models, such as hidden Markov models (HMM), support vector machines (SVM) and conditional random fields (CRF). However, these methods need professional domain knowledge and a large number of human participations to extract features, which increases the difficulty of named entity recognition in a specific domain. In recent

years, the state-of-the-art English NER models are mainly constructed by combining deep learning and CRF. For example, the method of combining long short-term memory (LSTM) with CRF performs well in NER tasks^[1-5].

Compared with English NER, the difficulties of Chinese NER mainly include the following aspects: 1) Chinese words have stronger polysemy, and the same words may have different meanings in different contexts; 2) English text contains space, initial letter upper and other identifiers to determine the entity boundary, while Chinese text does not have similar entity boundary identifiers, which increases the difficulty of entity boundary identification; 3) Chinese NER tasks usually need to be combined with Chinese word segmentation and shallow parsing, and the accuracy of these methods directly affects the effectiveness and stability of the entity recognition model. In view of the above problems, many researchers have applied the deep learning method to the research of Chinese NER, because the feature extraction of text data through deep learning not only avoids the tedious manual feature extraction, but also increases the generalization ability of the model. HAMMERTON et al.^[6]

This work was supported by ZTE Industry-University-Institute Cooperation Funds under Grant No. HC-CN-20190910009, and in part by the National Natural Science Foundation of China under Grant No. 61772269.

constructed the basic framework of LSTM-CRF entity recognition model. On this basis, CHIU et al.^[7] added a convolutional neural network (CNN) data preprocessing layer to the front end of the LSTM model, and obtained the F1 value of 88.83% on comll-2003 corpus; LI et al.^[8] constructed the CNN-bidirectional long-term and short-term memory network (BiLSTM)-CRF named entity recognition model, and achieved significant results on the Biocreative II GM and JNLPBA2004 corpora; LUO et al.^[9] embedded the attention mechanism (ATT) on the basis of the BiLSTM-CRF model, and obtained the F1 value of 91.14% on the Biocreative IV corpus; WU et al.^[10] jointly trained the word segmentation and the CNN-BiLSTM-CRF model to enhance the recognition ability of the model for entity boundary, thereby improving the performance of the model's entity recognition; QIN et al.^[11] constructed a CNN-BiLSTM-CRF named entity recognition model combined with feature templates, and used artificial feature templates to extract local features of text, which achieved good results on large-scale network security data; ZHANG et al.^[12] proposed an LSTM model based on a lattice structure, which makes full use of word and word sequence information to improve the performance of the entity recognition model; WANG et al.^[13] used segmental neural network structure to extract text features and obtained the F1 value of 92.05% on the Microsoft Research Asia (MSRA) corpus; LIU et al.^[14] embedded the attention mechanism on the basis of the dense connection (DC)-BiLSTM-CRF model, and obtained the F1 value of 92.05% on the MSRA corpus; LIU et al.^[15] constructed a word-character (WC)-BiLSTM-CRF model, which added word information to the beginning or end of the whole character to enhance semantic information, and obtained the F1 value of 93.74% on the MSRA corpus.

However, there are differences between Chinese characters and words. The above methods focus on the feature extraction of characters and words, but ignore the polysemy problem in Chinese. In order to solve this problem, DEVLIN et al.^[16] constructed encoder representations from transformers (BERT) pre-training language model to obtain the semantic vector of words, which enhanced the generalization ability of the word vector model, enriched the syntax and grammatical information in the sentence, and effectively solved the problem of polysemy representation of a word. For example, in the sentence “道可道, 非常道 (The Dao/way that can be told is not the usual Dao/way),” the two “Dao” characters have different meanings, but in Word2vec^[17] and Glove^[18], the vector representations of the two “Dao” characters are the same, which is inconsistent with the objective facts. The BERT model can obtain the semantic vector of words according to context information, represent the polysemy of words, and enhance the semantic representation of sentences. In order to automatically extract the depth features of Chinese text and solve the problem of characterizing the polysemy representation, this paper constructs a Chinese NER model based on the BERT-BiLSTM-

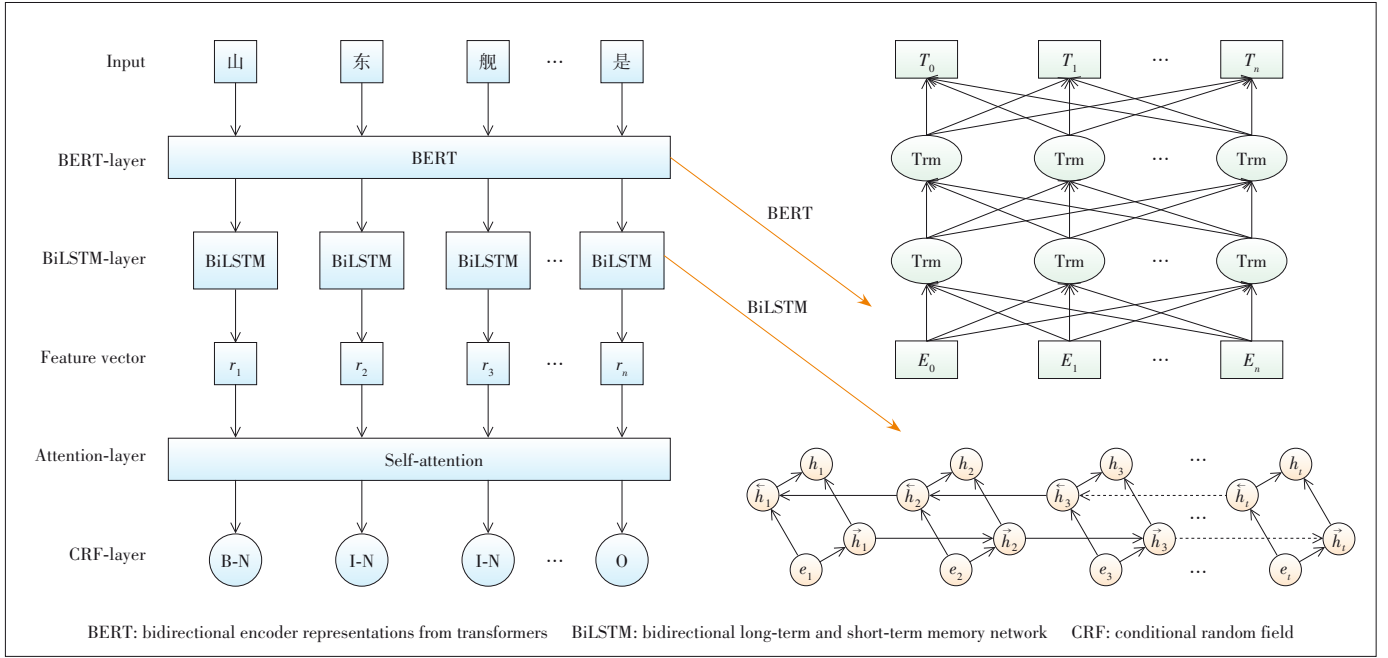
ATT-CRF network structure. The model uses the BERT model to train the word vector based on the context information of a word, and then inputs the trained word vector sequence into the BiLSTM-ATT model for further training, to capture the most important semantic information in the sentence, and finally the entity recognition result is marked by the CRF layer. The experimental results show that the proposed model achieves state-of-the-art performance on both the MSRA corpus and people's daily corpus, with the F1 values of 94.77% and 95.97% respectively.

The innovations of this paper are mainly as follows:

- 1) This paper applies the BERT pre-training language model to Chinese NER, which can obtain the semantic information of Chinese words in different contexts according to the context information of words, which effectively solves the problem of oversimplification of word vector representation. The BERT model is obtained by replacing the feature extractor in the ELMo model with a transformer. The experimental results show that the performance of the entity recognition model is improved effectively by introducing the BERT model.
- 2) The attention mechanism is embedded into the BiLSTM model and construct a BiLSTM-ATT module, which can selectively give different weights to different words in the text, and then the context-based semantic association information is used to effectively make up for the lack of deep neural network in obtaining local features, so as to highlight the importance of specific words to the whole text.
- 3) In the BERT-BiLSTM-ATT-CRF model proposed in this paper, the BERT model is only used to obtain the vector representation of the words in the text. The parameters of the model remain unchanged in the whole training process. The word vectors trained by the BERT are classified and recognized through the BiLSTM-ATT-CRF model, which can maintain the polysemy of words and reduce the training practice parameters.

2 Proposed BERT-BiLSTM-ATT-CRF Model

In recent years, converting traditional named entity recognition problems into sequence labeling tasks is the basic idea of the deep learning model for Chinese NER. The overall structure of the proposed BERT-BiLSTM-ATT-CRF model is shown in Fig. 1. The whole model is divided into three layers: the BERT layer, BiLSTM-ATT layer and CRF layer. Firstly, the annotated corpus is represented by the word vector based on context information through the BERT layer, and then the word vector is input into the BiLSTM-ATT layer for further training to obtain the important semantic features in the sentence. Finally, the output result of the BiLSTM-ATT layer is decoded by CRF to obtain the tag sequence of the optimal sentence level, and then extracting and classifying each entity in the sequence is conducted and classified to complete the task of Chinese entity recognition.



▲ Figure 1. Overall architecture of BERT-BiLSTM-ATT-CRF model

Algorithm 1 is the algorithm flow of the BERT-BiLSTM-ATT-CRF model.

Algorithm 1. The algorithm flow of BERT-BiLSTM-ATT-CRF model

Input: A sentence sequence S , a radical information matrix A .

Output: The entity list Y .

1: Preprocessing the dataset. The output embedding of each word in the sequence consists of three parts: token embedding (E^t), segment embedding (E^s) and position embedding (E^p);

2: The generated sequence vector $X = E^t \oplus E^s \oplus E^p$ is input into bidirectional transformer encoder for feature extraction, and the sequence vector with rich semantic preferential energy is obtained;

3: The word vectors generated by BERT training are input into the BiLSTM-ATT module to obtain the sequence depth features. $H = BiLSTM(X)$, $H' = Attention(H)$;

4: The probability and loss score of tag sequence y were calculated by CRF model;

5: **if** not converge **then**

Repeat lines 2 – 4;

6: **end if**

7: **return** the label sequence Y by using the Viterbi algorithm.

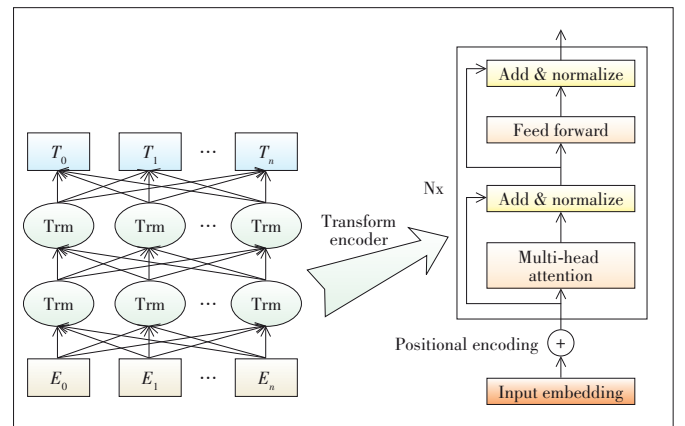
2.1 BERT Module

In the field of natural language processing (NLP), word embedding is used to map a word into a low dimensional space, which can effectively solve the problem of text feature sparseness, so that similar words in the semantic space have a closer distance. Traditional word vector generation methods, such as one hot, word2vec and Elmo^[19], and other pre-trained language models are mostly independent of the context informa-

tion of words, so it is difficult to accurately represent the polysemy of words. However, the BERT model proposed by JACOB et al. can be used to represent words according to their context information in an unsupervised way, which can effectively solve the problem of polysemy representation.

The structure of the BERT model is shown in Fig. 2. The multi-layer bidirectional transformer^[20] is used as the encoder in BERT model, and each unit is composed of feed-forward neural network (Feed Forward) and multi-head attention mechanism, so that the representation of each word can integrate the information of its left and right sides.

As shown in Fig. 2, the key part of the BERT model is the self-attention mechanism module in the transformer encoder. The function of the attention mechanism is to calculate every word in an input sentence to obtain the degree of correlation



▲ Figure 2. Structure of bidirectional encoder representations from transformers (BERT) model

between words in the sentence and then adjust the weight coefficient matrix to obtain the representation of words. The calculation is as follows:

$$\text{Attention}(\mathbf{Q}, \mathbf{K}, \mathbf{V}) = \text{Softmax}\left(\frac{\mathbf{Q}\mathbf{K}^T}{\sqrt{d_k}}\right)\mathbf{V}, \quad (1)$$

where $(\mathbf{Q}, \mathbf{K}, \mathbf{V})$ is the input word vector matrix, d_k is the dimension of the input vector, and $\mathbf{Q}\mathbf{K}^T$ is the relationship between input word vectors.

The calculation of the transformer adopts the multi-head attention mechanism^[20] to project through multiple linear transformation pairs for enhancing the model ability of focusing on different positions. The calculation is shown in Eqs. (2) and (3):

$$\text{MultiHead}(\mathbf{Q}, \mathbf{K}, \mathbf{V}) = \text{Concat}(\text{head}_1, \text{head}_2, \dots, \text{head}_k)\mathbf{W}^0, \quad (2)$$

$$\text{head}_i = \text{Attention}(\mathbf{Q}\mathbf{W}_i^Q, \mathbf{K}\mathbf{W}_i^K, \mathbf{V}\mathbf{W}_i^V), \quad (3)$$

where \mathbf{W}^0 is the additional weight matrix of the model to obtain different spatial position information. At the same time, in order to deal with the degradation problem in deep learning, the residual network and normalization layer are added into the transformer coding unit. The calculation is as follows:

$$\text{LN}(x_i) = \alpha \times \frac{x_i - u_i}{\sqrt{\sigma_L^2 + \varepsilon}} + \beta, \quad (4)$$

$$\text{FFN}(Z) = \max(0, Z\mathbf{W}_1 + b_1)\mathbf{W}_2 + b_2, \quad (5)$$

where α and β are learning parameters, and μ and σ are the mean and variance of the input layer. The representation of fully connected feedforward network (FFN) is shown in Eq. (5), where the output of the multi-head attention mechanism is denoted as Z and b is the bias vector.

2.2 BiLSTM-ATT Module

LSTM^[21-22] is a variant of recurrent neural network (RNN). It can effectively solve the gradient explosion or gradient disappearance during RNN training. Since the LSTM model cannot process context information at the same time, GRAVES et al.^[23] proposed the BiLSTM model, whose basic idea is to obtain the context information of input sequence through two hidden layers of LSTM. The specific operation is to connect the output vectors of the two hidden layers of LSTM to generate the context vector. The structure of LSTM unit is shown in Fig. 3, which consists of input gate, forgetting gate and output gate.

The vector representation of the output of the hidden layer of LSTM model is defined as follows:

$$f_t = \sigma(\mathbf{W}_{fx}\mathbf{x}_t + \mathbf{W}_{fh}h_{t-1} + \mathbf{b}_f), \quad (6)$$

$$i_t = \sigma(\mathbf{W}_{ix}\mathbf{x}_t + \mathbf{W}_{ih}h_{t-1} + \mathbf{b}_i), \quad (7)$$

$$\tilde{c}_t = \tanh(w_{cx}\mathbf{x}_t + w_{ch}h_{t-1} + \mathbf{b}_c), \quad (8)$$

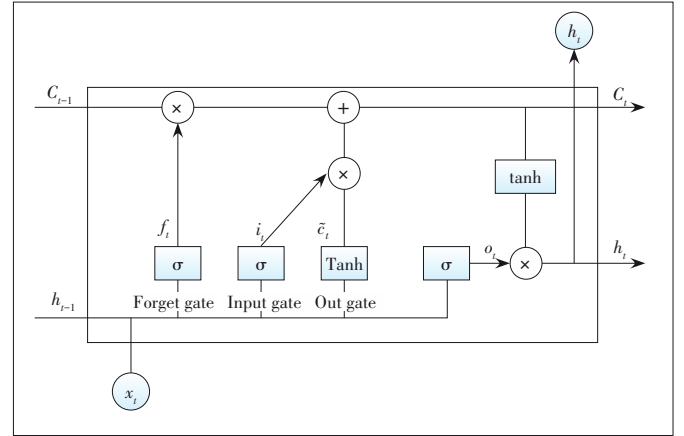
$$c_t = f_t * c_{t-1} + i_t * \tilde{c}_t, \quad (9)$$

$$o_t = \sigma(\mathbf{W}_{ox}\mathbf{x}_t + \mathbf{W}_{oh}h_{t-1} + \mathbf{b}_o), \quad (10)$$

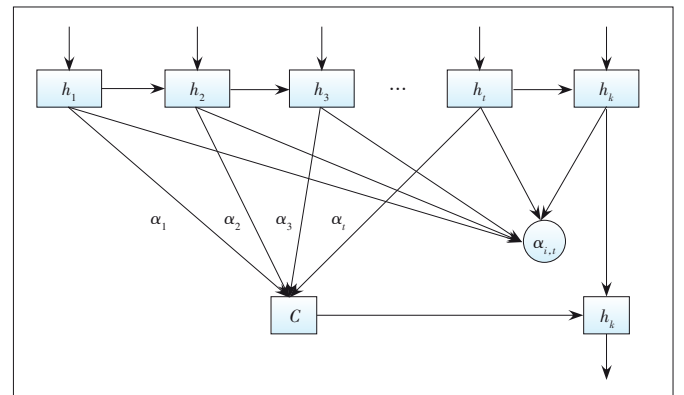
$$h_t = o_t * \tanh(c_t), \quad (11)$$

where \mathbf{W} and \mathbf{b} respectively represent the weight matrix and bias auto vector connecting the two hidden layers; σ is sigmoid activation function; \mathbf{x}_t represents the input vector at the time t ; f_t , i_t and o_t represent the input gate, forgetting gate and output gate at the time t respectively; $*$ represents the point multiplication operation, and h_t represents the output of LSTM unit at the time t .

The core idea of attention mechanism is to focus on important information at a specific time, while ignoring other non-important information^[24-25]. The integration of attention mechanism and BiLSTM model (Fig. 4) can effectively highlight the



▲ Figure 3. Long short-term memory (LSTM) unit structure



▲ Figure 4. Embedding attention mechanism into bidirectional long-term and short-term memory network (BiLSTM) model

role of keywords. The purpose of embedding attention mechanism in the BiLSTM neural network is to selectively give different weights to different words in the text, and then using context based semantic association information can effectively make up for the deficiency of deep neural network in obtaining local features.

In this paper, the calculation of the attention mechanism constructed can be summarized as follows:

1) Suppose h_i represents the feature vector output from the hidden layer of the BiLSTM model containing the context information of word w_i ; then h_i is transformed into u_i through the full connection layer, where u_i is defined as follows:

$$u_i = \tanh(W h_i + b), \quad (12)$$

where W and b represent the weight matrix and bias auto vector of attention mechanism respectively.

2) The similarity between u_i and the context vector u_i is calculated, and the normalized weight $\alpha_{i,t}$ is obtained by the Softmax function, where $\alpha_{i,t}$ is defined as follows:

$$\alpha_{i,t} = \frac{\exp(u_i^T u_t)}{\sum_i \exp(u_i^T u_t)}, \quad (13)$$

where $\alpha_{i,t}$ represents the importance of the corresponding word in the whole sentence; u_t represents the contribution of the corresponding word to the sentence, which is mainly obtained through random initialization and training.

3) The h_i obtained by each word is multiplied by the corresponding attention weight $\alpha_{i,t}$ to obtain the global vector C of the sentence, where C is defined as follows:

$$C = \sum_{j=1}^T \alpha_{i,t} h_j. \quad (14)$$

The sentence-level global vector C and the BiLSTM layer output h_t of the target word are combined into a vector $[C; h_t]$, which is fed to a tanh function as the output of attention layer. The output z_t of the attention layer is defined as follows:

$$z_t = \tanh(W [C; h_t]). \quad (15)$$

2.3 CRF Module

In the task of entity recognition, the BiLSTM model only obtains the word vector containing context information, but cannot deal with the interdependence between adjacent tags. Therefore, we use the CRF model^[26-27] to obtain an optimal prediction sequence through the relationship of adjacent tags, which is used to make up for the shortcomings of the BiLSTM model. The main operations of the CRF layer are as follows:

1) The parameter of the CRF layer is a $(k+2) \times (k+2)$ matrix A . The A_{ij} represents the transfer score from the i -th tag to the j -th tag, and then the previously labeled tags can be used when labeling a position. The reason for adding 2 is to

add a start state for the beginning of a sentence and a termination state for the end of the sentence. If you remember a tag sequence $y = (y_1, y_2, \dots, y_n)$ whose length is equal to the length of the sentence, the model scores the tag of sentence x , which is equal to y . The specific calculation is shown in Eq. (16).

$$\text{Score}(x, y) = \sum_{i=1}^n P_{i, y_i} + \sum_{i=1}^{n+1} A_{y_{i-1} y_i}. \quad (16)$$

Among them, P is the score matrix output by the BiLSTM-ATT module, and the size of P is $n \times k$, where n is the number of words and k is the number of tags; P_{ij} is the score of the i -th tag corresponding to the j -th word; A_{ij} is the transfer score matrix, A is the score of tag i transferred to tag j , and the size of A is $k+2$.

2) Obviously, the score of the whole sequence is equal to the sum of the scores of each position. The score of each position is divided into two parts: one part is determined by the score matrix P output by the LSTM model and the other is determined by the transfer matrix A of the CRF model. Therefore, the normalized probability can be obtained by the Softmax function as

$$P(y|x) = \frac{\exp(\text{Score}(x, y))}{\sum_{y' \in Y_x} \exp(\text{Score}(x, y'))}, \quad (17)$$

where x is the true label value, y' is the predicted label value, and Y_x is the set of all possible labels. During the training process, the maximum likelihood probability of the correct label sequence is as follows:

$$\log(p(y|x)) = S(x, y) - \sum_{y' \in Y_x} S(x, y'). \quad (18)$$

3) Finally, the Viterbi algorithm^[28] is used to obtain the sequence with the highest total score of prediction on all sequences, which is taken as the annotation result of the final entity recognition. The sequence with the highest score is as follows:

$$Y^* = \arg \max (x, y'), (y' \in Y_x). \quad (19)$$

3 Experiments

Our experiments on different datasets show that the proposed BERT-BiLSTM-ATT-CRF entity recognition model is effective in different fields. In addition, we compare the existing NER models with state-of-the-art performance, and further verify that our entity recognition model is effective and stable.

3.1 Datasets

In this paper, we mainly use the Chinese annotated the People's Daily corpus^[29] and MSRA corpus^[30] as the experimental data sets. These two data sets are Chinese evaluation data sets

in the domestic public news field. They mainly include three types of entities: person names, place names and organizations. In order to ensure the fairness of the comparison, we use the same data segmentation method as CHEN et al. used^[31], and divide the data into three parts: the training set, verification set and test set. The specific scales of the corpora are shown in Table 1.

3.2 Data Annotation and Evaluation Metrics

The commonly used labeling modes of NER include BIO (B-begin, I-inside, O-outside), BIOE (B-begin, I-inside, O-outside, E-end), BIOES (B-begin, I-inside, O-outside, E-end, S-single), etc. In this experiment, we choose to use the BIO labeling mode, and there are seven prediction labels, which are “O”, “B-PER”, “I-PER”, “B-ORG”, “I-ORG”, “B-LOC” and “I-LOC”. In order to evaluate the performance of the proposed model, the precision (P), recall (R) and F-measure (F) are used as the evaluation criteria. The definitions of P , R and F are shown as follows:

$$P = \frac{TP}{TP + FP}, R = \frac{TP}{TP + FN},$$

$$F_\beta = \frac{(\beta^2 + 1)PR}{\beta^2 P + R} \quad (\beta^2 \in [0, +\infty]) \quad (20)$$

Among them, TP is the number of positive samples correctly predicted; TN is the number of negative samples predicted correctly; FP is the number of negative samples predicted incorrectly; FN is the number of positive samples predicted incorrectly. P is the precision rate and R is the recall rate.

3.3 Hyper-Parameter Settings

We select the optimal hyper-parameter values of the model through model training and consideration of previous work in the literature. There are two kinds of pre-training language models: BERT-Base and BERT-Large. Some parameters of these two models are different. In this experiment, we choose to use the pre-training language model of BERT-Base. The model has a total of 12 layers and 768 dimensions of the hidden layer; it adopts a 12-head mode, including 110 million parameters. During the training, the maximum sequence length is set to 128, the size of batch size is 64, the number of hidden layers of BiLSTM is 200, and the Adam optimizer^[32] is used to select the appropriate learning rate to 0.001 5. In order to prevent over-fitting of the model, the dropout technology^[33] is introduced into the model and its value is set to 0.5. The specific parameter settings are shown in Table 2.

3.4 Experimental Results and Analysis

3.4.1 Compared with Traditional Neural Network

In order to make a more objective evaluation on the perfor-

▼Table 1. Statistics of datasets

Dataset	Type	Train	Dev	Test
People's Daily	Sentence	17.6k	0.9k	1.7k
MSRA	Sentence	46.4k	Null	4.4k

MSRA: Microsoft Research Asia corpus

▼Table 2. Optimal hyper-parameter values of BERT-BiLSTM-ATT-CRF model

Layer	Parameter	Value
BERT	Transformer layer number	12
	Hidden layer dimension	768
	Head number	12
BiLSTM	Optimizer	Adam
	Batch size	32
	Dropout rate	0.5
	Learning rate	0.001 5
	Hidden layer number	200

ATT: attention mechanism

BERT: bidirectional encoder representations from transformers

BiLSTM: bidirectional long-term and short-term memory network

CRF: conditional random field

mance of the proposed BERT-BiLSTM-ATT-CRF model, we use the People's Daily corpus and MSRA corpus to evaluate the performance of different models, and use the values of P , R and $F1$ to evaluate the performance of model entity recognition. The specific experimental results are shown in Tables 3 and 4.

As shown in Tables 3 and 4, we compare the proposed BERT-BiLSTM-ATT-CRF model with the traditional classical neural network model. Firstly, the experimental results of LSTM-CRF and BiLSTM-CRF show that the $F1$ value of the latter is higher than that of the former on the People's Daily corpora and MSRA corpora. The main reason is that LSTM only considers the above information, while BiLSTM can obtain context sequence information by using bidirectional structure and extract more effective features. Secondly, the experimental results of BiLSTM and BiLSTM-CRF show that the $F1$ value of BiLSTM-CRF model increases by 5.04% and 7.99% respectively on the two corpora after adding the CRF module. The main reason is that the CRF module can make full use of the interdependence between adjacent tags while considering

▼Table 3. Test results on People's Daily corpus

Model	$P/\%$	$R/\%$	$F1/\%$
LSTM-CRF	84.20	80.20	82.00
BiLSTM	81.08	79.21	80.05
BiLSTM-CRF	87.21	83.21	85.09
BERT-BiLSTM-CRF	96.04	95.30	95.67
BERT-BiLSTM-ATT-CRF	96.28	95.67	95.97

ATT: attention mechanism

BERT: bidirectional encoder representations from transformers

BiLSTM: bidirectional long-term and short-term memory network

CRF: conditional random field

LSTM: long short-term memory

▼Table 4. Test results on MSRA corpus

Model	P/%	R/%	F1/%
LSTM-CRF	83.45	80.20	82.00
BiLSTM	78.72	79.21	80.05
BiLSTM-CRF	86.79	83.21	85.09
BERT-BiLSTM-CRF	94.38	94.92	94.65
BERT-BiLSTM-ATT-CRF	94.52	95.02	94.77

ATT: attention mechanism

BERT: bidirectional encoder representations from transformers

BiLSTM: bidirectional long-term and short-term memory network

CRF: conditional random field

LSTM: long short-term memory

the context information, so as to obtain the global optimal tag sequence.

At the same time, the results in Tables 3 and 4 show that the performance of the entity recognition model is improved when the attention mechanism is added to the BERT-BiLSTM-CRF model. The main reason is that the attention mechanism is embedded in the BiLSTM neural network, so that the model can selectively give different weights to different words in the text, and then use the context based semantic association information to effectively make up for the lack of deep neural network in obtaining local features.

In order to improve the performance of the Chinese entity recognition model, some researchers have introduced the BERT model to preprocess the word vector on the basis of the BiLSTM-CRF model. The experimental results show that the $F1$ values of the BERT-BiLSTM-CRF model on the two corpora are 94.74% and 94.21% respectively, which is much higher than that of the BiLSTM-CRF model on the same corpus. The main reason is the addition of the BERT model, which can obtain the semantic vector of the word according to the context information of the word to represent the polysemy of the word, so that the generated word vectors can better represent the semantic information in different contexts, thus enhancing the generalization ability of the model and improving the performance of the model entity recognition. In this paper, the attention mechanism is introduced on the basis of the BERT-BiLSTM-CRF model, which effectively highlights the role of keywords in sentences, thereby improving the entity recognition ability of the model. The comparison of the experimental results of BERT-BiLSTM-CRF and BERT-BiLSTM-ATT-CRF shows that after adding attention, the $F1$ value of the model obtained by BERT-BiLSTM-ATT-CRF is higher than that of the former in both corpora, which proves the effectiveness of the model proposed in this paper.

3.4.2 Comparison with Previous Works

In order to further verify the effectiveness and stability of the proposed BERT-BiLSTM-ATT-CRF model, we compare it with the existing advanced models. The results are shown in Table 5.

As shown in Table 5, the MSRA corpus is used as the data

▼Table 5 Different models compared on MSRA corpus

Model	P/%	R/%	F1/%
CHEN et al. (2006) ^[31]	91.22	81.71	86.20
ZHANG et al. (2006) ^[32]	92.20	90.18	91.18
ZHOU et al. (2013) ^[33]	91.86	88.75	90.28
LU et al. (2016) ^[34]	NULL	NULL	87.94
Radical-BiLSTM-CRF (2016) ^[35]	91.28	90.62	90.95
IDCNN-CRF (2017) ^[36]	89.39	84.64	86.95
Lattice-LSTM-CRF (2018) ^[12]	93.57	92.79	93.18
CNN-BiLSTM-CRF(2019) ^[10]	91.63	90.56	91.09
WC-LSTM-pertain (2019) ^[15]	Null	Null	93.74
BERT-IDCNN-CRF (2020) ^[36]	94.86	93.97	94.41
BERT-BiLSTM-CRF (2020) ^[37]	94.38	94.92	94.65
HanLP (BERT) ^[38]	94.79	95.65	95.22
BERT-BiLSTM-ATT-CRF	94.52	95.02	94.77

BERT: bidirectional encoder representations from transformers

BiLSTM: bidirectional long-term and short-term memory network

CNN: convolutional neural network

CRF: conditional random field

HanLP: Han Language Processing

IDCNN: Iterated Dilated Convolutional Neural Network

LSTM: long short-term memory

WC: word-character

set to evaluate the performance of the entity recognition model. CHEN et al.^[31-34] constructed a statistical model using manual features and character embedding features. The Radical-BiLSTM-CRF^[35] model uses bidirectional LSTM to extract the feature vector of the root sequence and then joins it with the character vector to form the model input, which improves the performance of model entity recognition. The Lattice-LSTM-CRF model^[12] improves the traditional LSTM unit to grid LSTM, and then makes full use of the information between words and the word order, effectively avoiding the error of word segmentation and obtaining better results of entity recognition. The CNN-BiLSTM-CRF model^[10] extracts glyph embedding with morphological features from each Chinese character by CNN, and connects it with the word embedding of semantic feature information to form the input of the model, which obtains good results. The WC-LSTM-CRF^[15] model uses word information to strengthen semantic information and reduce the influence of word segmentation errors. The $F1$ value reaches 93.74%.

The above-mentioned entity recognition models greatly improve the value of $F1$, but the improved models always focus on the extraction of character and word features and ignore the problem of polysemy in Chinese. LI et al.^[36] and XIE et al.^[37] used the BERT pre-training language model to represent the vector, which enhanced the generalization ability of the word vector model and enriched the syntactic and grammatical information in the sentence. This model effectively solved the representation problem of polysemy of a word. In order to further improve the performance of entity recognition model, we construct the BERT-BiLSTM-ATT-CRF model based on the

research in Ref. [33]. The model can effectively capture the most important semantic information in the sentence while ensuring the polysemy representation of a word. Although the model proposed in this paper is not different from the model of BERT-BiLSTM-CRF and BERT-IDCNN-CRF, the *F1* value of the model on the MSRA corpus reaches 94.77%. The experimental results show that the proposed model achieves state-of-the-art performance on both the MSRA corpus and People's Daily corpus.

4 Conclusions

Traditional named entity recognition methods require professional domain knowledge and a large amount of human participation to extract features. Meanwhile, there are some problems in Chinese entity recognition tasks, such as polysemy and Chinese sentences without entity boundary identifiers. Firstly, we use the BERT pre-training language model to obtain the semantic features containing the contextual information of the word, which effectively solves the problem of polysemy representation of a word; Secondly, the classic neural network model BiLSTM is embedded with the attention mechanism, which can extract the most important semantics in the sentence features; Finally, we use the CRF model to obtain an optimal prediction sequence through the relationship of adjacent tags, which is used to make up for the shortcomings of the BiLSTM model. In order to verify the effectiveness of the proposed BERT-BiLSTM-Att-CRF model, the People's Daily corpus and MSRA corpus are used as the data sets for model performance evaluation. Compared with other models, the BERT-BiLSTM-ATT-CRF model shows the best results on both the corpora.

The biggest advantage of the BERT-BiLSTM-ATT-CRF model is that it can conduct pre-training according to the semantic information of the word context and obtain the word level features, syntactic structure features and semantic information features of context, which makes the model have better performance than the other models. At the same time, the attention mechanism is embedded into the BiLSTM model to enhance the extraction of key information features in sentences. Combined with CRF, it can take advantage of the interdependence between adjacent tags to further improve the ability of Chinese entity recognition. Our next work plan is to study the construction method of domain specific NER, and test the performance and generalization ability of the proposed model in multi-domain NER tasks.

References

[1] GRIDACH M. Character-level neural network for biomedical named entity recognition [J]. Journal of biomedical informatics, 2017, 70: 85 – 91. DOI: 10.1016/

- j.jbi.2017.05.002
- [2] LAMPLE G, BALLESTEROS M, SUBRAMANIAN S, et al. Neural architectures for named entity recognition [C]//Conference of the North American Chapter of the Association for Computational Linguistics: Human Language Technologies. Association for Computational Linguistics, 2016. DOI: 10.18653/v1/n16-1030
- [3] MA X Z, HOVY E. End-to-end sequence labeling via Bi-directional LSTM-CNNs-CRF [C]//54th Annual Meeting of the Association for Computational Linguistics. Association for Computational Linguistics, 2016: 1064 – 1074
- [4] SHIN Y, LEE S G. Learning context using segment-level LSTM for neural sequence labeling [J]. IEEE/ACM transactions on audio, speech, and language processing, 2020, 28: 105 – 115. DOI: 10.1109/TASLP.2019.2948773
- [5] DONG D Z, OUYANG S. Optimization Techniques of Network Communication in Distributed Deep Learning Systems [J]. ZTE technology journal, 2020, 26(5): 2-8. DOI: 10.12142/ZTETJ.202005002
- [6] HAMMERTON J. Named entity recognition with long short-term memory [C]//Proceedings of the seventh conference on natural language learning at HLT-NAACL. Association for Computational Linguistics, 2003: 172 – 175. DOI: 10.3115/1119176.1119202
- [7] CHIU J P C, NICHOLS E. Named entity recognition with bidirectional LSTM-CNNs [J]. Transactions of the association for computational linguistics, 2016, 4: 357 – 370. DOI: 10.1162/tac1_a_00104
- [8] LI L S, GUO Y K. Biomedical named entity recognition based on CNN-BLSTM-CRF model [J]. Journal of Chinese information processing, 2018, 32(1): 116 – 122. DOI: 10.3969/j.issn.1003-0077.2018.01.015
- [9] LUO L, YANG Z H, YANG P, et al. An attention-based BiLSTM-CRF approach to document-level chemical named entity recognition [J]. Bioinformatics, 2017, 34(8): 1381 – 1388. DOI: 10.1093/bioinformatics/btx761
- [10] WU F Z, LIU J X, WU C H, et al. Neural Chinese named entity recognition via CNN-LSTM-CRF and joint training with word segmentation [C]//The World Wide Web Conference. ACM, 2019: 3342 – 3348. DOI: 10.1145/3308558.3313743
- [11] QIN Y, SHEN G W, ZHAO W B, et al. Network security entity recognition method based on deep neural network [J]. Journal of Nanjing university (natural science), 2019, 55 (1): 29 – 40
- [12] ZHANG Y, YANG J. Chinese NER using lattice LSTM [EB/OL]. (2018-07-05) [2020-05-01]. <https://arxiv.org/abs/1805.02023>
- [13] WANG L, XIE Y, ZHOU J S, et al. Fragment level Chinese named entity recognition based on neural network [J]. Journal of Chinese information processing, 2018, 32 (3): 84 – 90, 100. DOI: 10.3969/j.issn.1003-0077.2018.03.012
- [14] LIU X J, GU L C, SHI X Z. Named entity recognition based on BiLSTM and attention mechanism [J]. Journal of luoyang institute of technology, 2019, 29 (1): 65 – 70
- [15] LIU W, XU T G, XU Q H, et al. An encoding strategy based word-character LSTM for Chinese NER [C]//Conference of the North American Chapter of the Association for Computational Linguistics: Human Language Technologies. Association for Computational Linguistics, 2019: 2379 – 2389
- [16] DEVLIN J, CHANG M W, LEE K, et al. BERT: pre-training of deep bidirectional transformers for language understanding [EB/OL]. (2018-10-11) [2020-05-01]. <https://arxiv.org/abs/1810.04805>
- [17] MIKLOV T, CHEN K, CORRADO G, et al. Efficient estimation of word representations in vector space [EB/OL]. (2013-09-07) [2021-05-01]. <https://arxiv.org/abs/1301.3781>
- [18] PENNINGTON J, SOCHER R, MANNING C. Glove: global vectors for word representation [C]//Conference on Empirical Methods in Natural Language Processing (EMNLP). Association for Computational Linguistics, 2014. DOI: 10.3115/v1/d14-1162
- [19] PETERS M E, NEUMANN M, IYYER M, et al. Deep Contextualized Word Representations [C]//Conference of the North American Chapter of the Association for Computational Linguistics: Human Language Technologies. Association for Computational Linguistics, 2018: 2227 – 2237. DOI: 10.18653/v1/N18-1202
- [20] VASWANI A, SHAZEER N, PARMAR N, et al. Attention is all you need [C]//Advances in Neural Information Processing Systems 30: Annual Conference on Neural Information Processing Systems. NIPS, 2017: 5998 – 6008
- [21] JOZEFOWICZ R, ZAREMBA W, SUTSKEVER I. An empirical exploration of recurrent network architectures [C]//32nd International Conference on Ma-

- chine Learning. JMLR, 2015: 2342 – 2350
- [22] GUO D, ZHENG Q F, PENG X J, et al. Face detection detection, alignment alignment, quality assessment and attribute analysis with multi-task hybrid convolutional neural networks [J]. ZTE Communications, 2019, 17(3): 15 – 22. DOI: 10.12142/ZTECOM.201903004
- [23] GRAVES A, SCHMIDHUBER J. Framewise phoneme classification with bidirectional LSTM and other neural network architectures [J]. Neural networks, 2005, 18(5/6): 602 – 610. DOI: 10.1016/j.neunet.2005.06.042
- [24] TAN Z X, WANG M X, XIE J, et al. Deep semantic role labeling with self-attention [EB/OL]. (2017-12-05)[2020-05-01]. <https://arxiv.org/abs/1712.01586>
- [25] SHEN T, ZHOU T Y, LONG G D, et al. DiSAN: directional self-attention network for RNN/CNN-free language understanding [EB/OL]. (2017-11-20)[2020-05-01]. <https://arxiv.org/abs/1709.04696>
- [26] LAFFERTY J, MCCALLUM A, PEREIRA F. Conditional random fields: probabilistic models for segmenting and labeling sequence data [C]//18th International Conference on Machine Learning 2001 (ICML 2001). ACM, 2001: 282 – 289
- [27] ZHU Y Y, WANG G X, KARLSSON B F. CAN-NER: Convolutional attention network for Chinese named entity recognition [EB/OL]. (2019-04-30)[2020-05-01]. <https://arxiv.org/abs/1904.02141>
- [28] VITERBI A. Error bounds for convolutional codes and an asymptotically optimum decoding algorithm [J]. IEEE transactions on information theory, 1967, 13(2): 260 – 269. DOI: 10.1109/TIT.1967.1054010
- [29] SI N W, WANG H J, LI W, et al. Chinese part of speech tagging model based on attentional long-term memory network [J]. Computer science, 2018, 45 (4): 66 – 70
- [30] LEVOW G A. The third international Chinese language processing bakeoff: word segmentation and named entity recognition [C]//Fifth SIGHAN Workshop on Chinese Language Processing. Association for Computational Linguistics, 2006: 108 – 117
- [31] CHEN A T, PENG F C, SHAN R, et al. Chinese named entity recognition with conditional probabilistic models [C]//Fifth SIGHAN Workshop on Chinese Language Processing. Association for Computational Linguistics, 2006: 173 – 176
- [32] ZHANG S X, QIN Y, WEN J, et al. Word segmentation and named entity recognition for sighan bakeoff3 [C]//Fifth SIGHAN Workshop on Chinese Language Processing. Association for Computational Linguistics, 2013: 158 – 161
- [33] ZHOU J S, QU W G, ZHANG F. Chinese named entity recognition via joint identification and categorization [J]. Chinese journal of electronics, 2013, 22 (2): 225 – 230
- [34] LU Y N, ZHANG Y, JI D H. Multiprototype Chinese character embedding [C]//Tenth International Conference on Language Resources and Evaluation. Association for Computational Linguistics, 2016: 855-859
- [35] DONG C H, ZHANG J J, ZONG C Q, et al. Character-based LSTM-CRF with radical-level features for Chinese named entity recognition [M]//Natural Language Understanding and Intelligent Applications. Cham, witzerland: Springer International Publishing, 2016: 239 – 250. DOI: 10.1007/978-3-319-50496-4_20
- [36] LI N, GUAN H M, YANG P, et al. Chinese named entity recognition method based on BERT-IDCNN-CRF [J]. Journal of shandong university (science edition), 2020, 55 (1): 102 – 109
- [37] XIE T, YANG J N, LIU H. Chinese entity recognition based on BERT-BiLSTM-CRF model [J]. Computer systems & applications, 2020(7): 48 – 55
- [38] HE H. HanLP: Han language processing [EB/OL]. (2020-04-30)[2020-07-01]. <https://github.com/hankcs/HanLP>

Biographies

LI Daiyi (lidaiyi@nuaa.edu.cn) received his master's degree from School of computer and Communication Engineering, Zhengzhou University of Light Industry, China in 2018. He is studying for a doctor's degree in the School of Computer Science and Technology, Nanjing University of Aeronautics and Astronautics, China. His main research interests are knowledge graphs and big data.

TU Yaofeng received his Ph.D. degree from Nanjing University of Aeronautics and Astronautics, China. He is a researcher at ZTE Corporation. His research interests include big data, database and machine learning.

ZHOU Xiangsheng is an expert and senior R&D manager in the AI field of ZTE Corporation. His research fields mainly include NLP, NAS, training acceleration, etc.

ZHANG Yangming is a software engineer at ZTE Corporation. His research interests mainly focus on natural language processing, knowledge engineering and acoustic signal processing.

MA Zongmin received his Ph.D. degree from the City University of Hong Kong, China and is a full professor with Nanjing University of Aeronautics and Astronautics, China. His research interests mainly include big data and knowledge engineering. He has published more than 100 papers in highly cited international journals and authored five monographs published by Springer. He is the Fellow of IFSA and Fellow of IET.



Intelligent Antenna Attitude Parameters Measurement Based on Deep Learning SSD Model

Abstract: Due to the consideration of safety, non-contact measurement methods are becoming more acceptable. However, massive measurement will bring high labor-cost and low working efficiency. To address these limitations, this paper introduces a deep learning model for the antenna attitude parameter measurement, which can be divided into an antenna location phase and a calculation phase of the attitude parameter. In the first phase, a single shot multibox detector (SSD) is applied to automatically recognize and discover the antenna from pictures taken by drones. In the second phase, the located antennas' feature lines are extracted and their attitude parameters are then calculated mathematically. Experiments show that the proposed algorithms outperform existing related works in efficiency and accuracy, and therefore can be effectively used in engineering applications.

Keywords: deep learning; drone; object detection; SSD algorithm; visual measurement; antenna attitude parameters

FAN Guotian¹, WANG Zhibin²

(1. ZTE Corporation, Shenzhen 518057, China;
2. Xidian University, Xi'an 710071, China)

DOI: 10.12142/ZTECOM.2022S1006

<http://kns.cnki.net/kcms/detail/34.1294.TN.20220125.1135.001.html>, published online January 26, 2022

Manuscript received: 2021-04-16

Citation (IEEE Format): G. T. Fan and Z. B. Wang, "Intelligent antenna attitude parameters measurement based on deep learning SSD model," *ZTE Communications*, vol. 20, no. S1, pp. 36 - 43, Jan. 2022. doi: 10.12142/ZTECOM.2022S1006.

1 Introduction

With the rapid development of communication technologies, an increasing number of base stations are built around the world. Antennas work as an interface between radio waves propagating through space and electric currents moving in metal conductors. For providing subscribers with high-quality communication services, it is critical to guarantee the speed and stability of network signals. According to radiation direction, antennas in base stations can be roughly divided into three categories: 1) omnidirectional antennas which have uniform radiation power in the horizontal direction; 2) directional antennas that have uneven radiation power in both horizontal and vertical directions; 3) special antennas which have variable radiation direction depending on their usages. Among these categories, the directional antennas' radiation direction and power are most susceptible to the attitude.

To ensure that each base station antenna works properly, the antenna attitude parameters which determine the electromagnetic coverage of the directional antenna need to be set

appropriately. Sector-shaped antennas are one of the most common directional antennas, and their attitude parameters mainly include the pitch angle, the azimuth angle, and the height position. Among them, the antennas' suspension height is fixed. However, the pitch angle and the azimuth angle of the antennas can be easily changed by external factors such as wind and sunlight, which further changes the electromagnetic coverage and weakens the stability of signals. Thus, it is urgent to regularly and efficiently measure the pitch angle and the azimuth angle of sector-shaped antennas on the base station.

Existing antenna attitude parameter measurement methods can be roughly divided into the following two categories.

1) Contact measurement methods. In these methods, engineering surveyors apply physical tools such as inclinometers and goniometers to measure the antennas' relevant posture parameters and then read the measurements manually. However, these methods suffer from the following limitations. First, since antennas are usually installed on high places such as roofs, hillsides, and the top of telephone poles, these methods put the engineering surveyors' life at risk; Second, since the engineering surveyors' wages are high and the measuring tools are expensive, the cost is high; Last but not the least, the time to perform these methods is usually relatively long. Actu-

This work is supported in part by ZTE Industry-Academia-Research Cooperation Funds under Grant No. HC-CN-20181030016.

ally, nowadays, most countries do not apply these contact methods anymore.

2) Non-contact measurement using drones. Most base station antennas are built on high places which usually cannot be reached easily. With drones being more and more frequently applied in complete high-altitude tasks such as shooting, transportation, and reconnaissance, they are also applied to assist the measurement process of the elevation angle and the azimuth angle of sector-shaped antennas on the base station. Usually, drones are controlled by smartphones to take pictures of the antennas, which can be previewed by the operators in real-time^[1]. Then, for obtaining the required antennas' attitude parameters, techniques such as image analysis and three-dimensional reconstruction are applied to analyze collected antenna pictures. Compared with traditional methods, the non-contact measurement methods have advantages of high efficiency, safety, and convenience. Thus, they are becoming more and more popular in both research and industrial communities. However, they also suffer from shortcomings of relatively low efficiency and the requirement of manual intervention.

2 Related Work

To address the above disadvantages of existing non-contact measurement methods, we propose a novel antenna attitude parameter measurement algorithm, which can be divided into an antenna localizing phase and an attitude parameter calculation phase. In the first phase, a deep learning algorithm called the single shot multibox detector (SSD) is applied to automatically identify and localize the antenna from pictures taken by drones. For locating the antennas in real-time, a lightweight MobileNet is applied in the SSD for feature extraction and the ratio of antennas' length to width is used as prior information, which greatly improves the efficiency. In the attitude parameter calculation phase, a straight line detection process is performed on the localized image by applying the line segment detector (LSD), and the longest straight line is selected as a feature line. The attitude parameters are then calculated according to extracted feature lines mathematically.

The remaining of this paper is organized as follows. In Section 2, we demonstrate how the proposed antenna attitude parameter measurement algorithm works. In Section 3, we report the experimental results. The paper is concluded in Section 4.

3 Proposed SSD Algorithm

In this part, we will introduce the related work and technical details of the two phases of the proposed algorithm.

3.1 First Phase

The first phase of the algorithm is to locate the antenna automatically. We propose a deep learning algorithm based on an SSD network, which can locate the position of the antenna

accurately.

3.1.1 SSD Network

The regression-based object detection algorithm is called the one-stage detection algorithm. The input image uses a convolutional neural network (CNN) to directly return to the target category and position. It does not need to go through the tedious process of extracting candidate regions like region-based convolution neural networks (R-CNN). It is a kind of an end-to-end efficient object detection algorithm model that mainly includes You Only Look Once (YOLO)^[2] and SSD^[3].

The SSD algorithm is an important representative network model based on regression algorithms. It improves the YOLO algorithm and also combines related ideas of anchor boxes in the candidate region algorithm Faster R-CNN. The SSD algorithm is a great breakthrough in the application of deep learning to solve object detection problems. While the SSD algorithm has greatly improved the detection efficiency, it can better detect small objects and has a certain degree of accuracy.

In essence, the SSD network is a CNN that can directly get the position, category, and confidence of the detected object using forward propagation. The basic feature extraction network that the conventional SSD network uses is c-16^[4]. It mainly extracts feature maps of different scales and uses a series of fixed-size candidate bounding boxes to predict the location of the object and the classification confidence of each bounding box which probably contains the object, and finally performs a non-maximum suppression (NMS) method to get the final result.

3.1.2 Mobile-SSD Object Detection Network Model

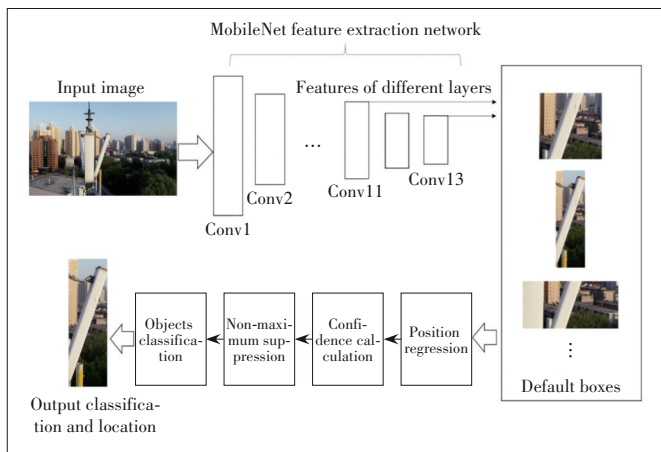
To fulfill the requirement of automatic intelligent detection, we optimize the SSD network based on the characteristics of the antenna object aiming at improving training efficiency and computing speed of the network. The optimized network can be better adapted to real-time work. We call the improved network model in this paper the Mobile-SSD model.

While retaining the overall detection process and end-to-end characteristics of the SSD network, we improve the network by using the following strategy: 1) Modify the feature extraction network; 2) Reduce the network structure's redundancy; 3) Add prior information.

The overall processing flow of the improved model is shown in Fig. 1. The final predicted output of the network is basically composed of two parts: one is the confidence level of the target's category, and the other is the position coordinates of the detected target's bounding box. According to the former, we can obtain the category of each antenna object detected in the image. According to the latter, we can obtain the antenna's position.

The following improvements and optimizations have been made to the SSD network structure.

1) Modify the output categories of the network. Objects



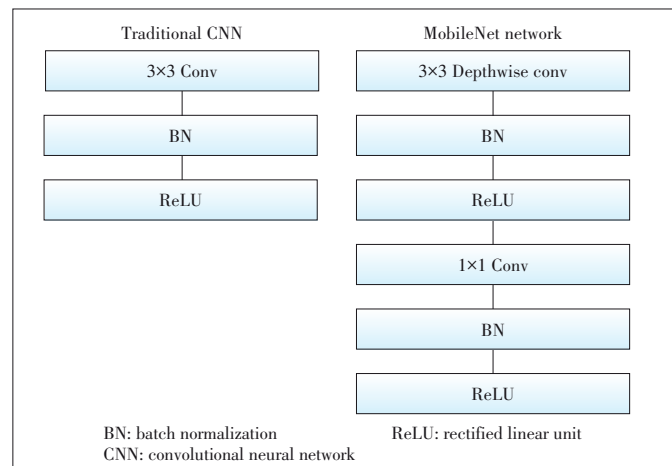
▲ Figure 1. Mobile-single shot multibox detector (SSD) object detection network model

used for antenna attitude measurement are organized into two categories: antenna side and antenna top. Thus, we only need to obtain the category and location of these two types of antenna objects from the network's output. However, the number of the categories of the original SSD network's output layer is 21, which is unnecessary for our work. Thus, we modify the number of the categories to 3 (background, antenna side, and antenna top). In this way, we can reduce redundancy and improve detection efficiency.

2) Replace the basic convolutional neural network for feature extraction. The original SSD network uses VGG16 as the basic feature extraction network. Most of its structure is composed of standard convolutional layers, so it takes a long time to extract features through convolution operation, and the overall detection efficiency cannot meet the requirement of mobile object detection which needs high efficiency. Therefore, it is a key problem to reducing the convolution complexity of the network and improve the efficiency of the network.

In order to improve the efficiency of feature extraction, we replace the feature extraction network in the original SSD model with a lightweight CNN MobileNet^[5], which can complete image feature extraction through a more efficient convolution operation. The lightweight CNN network model with deep separable convolution is more suitable for mobile or embedded devices. As shown in Fig. 2, the image detection process of the MobileNet network model is different from the traditional deep CNN.

In normal circumstances, the MobileNet model will use a 3×3 convolution kernel for convolution operation. The calculation of the convolution in MobileNet can be reduced by about 8 times compared with the traditional standard convolution. At the same time, the parameter number of the overall network is also reduced, so that the complexity of the network model during the training is reduced. And after completing the convolution, MobileNet will convert the convolution results into normal distribution by regularization, which can better avoid the overfitting phenomenon that always oc-



▲ Figure 2. Difference between MobileNet and traditional network

curs during the training. In this way, the network performance has been greatly improved.

3) Set the aspect ratio of the default box according to the prior information of the antennas. According to the characteristics of the SSD algorithm model, different types of objects should be accurately detected, which is completed by using several default boxes with different aspect ratios on the feature map. The basic size and shape of the default box are all subjectively set based on experience. The default aspect ratios of the original SSD network are 1:2, 1:3, and 1, 2, 3. However, most of the sector antennas are produced with a unified standard, so the aspect ratio of the side and top of antennas has been basically determined. Adding the aspect ratio of antennas as prior information can reduce the detection interference obviously. Therefore, by collecting antenna pictures for calculation and statistics, we obtain that the aspect ratio of the antenna side is 1:4, and the aspect ratio of the antenna top is 3:1. Then by removing the useless default aspect ratio and adding the specified aspect ratio of antenna objects, we can reduce the interference of useless information and make the network more targeted and efficient.

3.2 Second Phase

After completing the automatic detection of the location of the antenna objects by the Mobile-SSD algorithm, the second phase is the measurement of antenna attitude parameters. The main process of the measurement algorithm is as follows. Firstly, use the LSD straight line detection algorithm to detect and extract the image straight line from the selected area. And then according to the length of the straight lines that exist in the feature detection images, sort the sequence of straight lines and take the longest straight line as the antenna feature line. At last, combine the drone's own parameters to calculate the azimuth angle and pitch angle. In the following parts, we will introduce the details of the algorithm for antenna attitude parameters calculation.

3.2.1 LSD Line Detection Algorithm

In the field of image process, in 1962 the Hough transform^[6] laid the foundation for the detection of line segments and shapes in images. Subsequently, RAFAEL et al. proposed a linear detection algorithm LSD^[7] based on the Hough transform, and the accuracy of detection can achieve sub-pixel precision. The main difference between the LSD algorithm and the Hough transform is that the former uses the concept of the gradient to determine the straight line. The gradient in the selected area is calculated, and the area which has the same gradient is regarded as a straight-line segment. The direction of the line segment is also the same as the gradient average direction. Detecting the straight line in the image is implied by looking for the pixel area in the image with large gradient changes. The efficiency and effect of the LSD algorithm are much better than those of the Hough transform, therefore we use the LSD algorithm to complete extracting the characteristic line of the antenna object in the determined area.

The specific process of the LSD line detection algorithm can be summarized as follows^[7]:

Algorithm 1. Algorithm of the specific process of the LSD line detection

Input: the image to be detected I

Output: the line detection result set L

a) Do Gaussian down-sampling on the input image I at a certain scale, usually scale=0.8.

b) Calculate the gradient of each pixel in the down-sampled image and the corresponding level-line direction.

c) Pseudo-sort all pixels according to the obtained gradient, establish the corresponding state sequence table, initially set all pixels to NOT USED.

d) Traverse all the gradient, change the state in the state sequence table to USED for the points whose value is less than the threshold ρ , and record it in the table for an update.

e) Take the pixel with the largest gradient in the state table as the seed point, and set the state to USED.

do:

1. Starting from the seed point, change the state of NOT USED points that meet the condition of the direction in $[k, -k]$ around the pixel points to USED.

2. Use the circumscribed rectangle R to enclose all the satisfying points.

3. Determine whether the density of the homogeneous same-sex point meets the set threshold. If not, cut the circumscribed rectangle R into a new circumscribed rectangle, until the density reaches the requirement.

4. Calculate the corresponding nondeterministic finite automaton (NFA) of the final circumscribed rectangle R .

5. By changing the NFA of R , when $NFA(R) \leq \varepsilon$, the rectangle is considered to be the output line l , and it should be added to the line detection result set L . Repeat the algorithm until the state of all pixels is USED.

3.2.2 Antenna Feature Line Extraction

After the detection by the Mobile-SSD network, in an image with an antenna object, we will get the coordinate position of the antenna object, and mark it with a rectangular box. We call this area the region of interest (ROI). By using the LSD algorithm introduced in Section 2.2.1, we can detect all straight lines in the ROI area. In the actual scene of antenna attitude parameter measurement, the one that can generally represent the two parameters of the antenna is the longest line segment on the antenna's side and top, so we need to select the longest straight line in the ROI area. We sort by the support domain line sequence in the region and connect the longest line group in the same gradient direction to the longest line, and then mark it in the image as the feature line.

As shown in Fig. 3, the longest red line is the feature line extracted from the side of the antenna. We use this longest straight line to represent the antenna's feature. The subsequent calculation of antenna attitude parameters is based on the feature line.

3.2.3 Calculate Antenna Attitude Parameters

For the sector antenna, we find that its hanging height, orientation, and other parameters are basically fixed, and the main parameters that affect the normal operation of the antenna are the pitch angle and the azimuth angle, which are the parameters we need to calculate. The pitch angle is physically the angle between the object and the horizontal plane; the azimuth angle is the angle between the direction parallel to the horizontal ground and the true north of the earth.

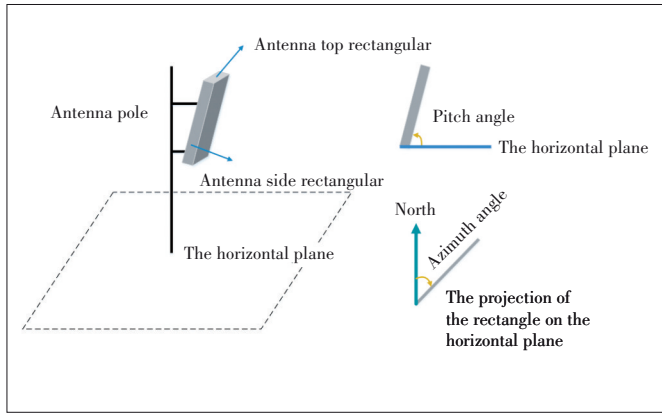
The schematic diagram of the pitch angle and the azimuth angle defined in the main three-dimensional space is shown in Fig. 4.

1) The pitch angle of the antenna. In space, the pitch angle α can be converted to the angle formed by the side rectangle of the antenna and the horizontal plane in the image taken by the drone from its front view, which is usually defined as the pitch angle of the sector antenna. From the plane view, it can be regarded as the angle obtained by rotating the side rectangle of the antenna object counterclockwise along the horizontal plane.

As shown in Fig. 5, the image plane taken by the drone is



▲ Figure 3. Feature line extracted



▲ Figure 4. Pitch angle and azimuth angle

G . The projection of the feature line l on the image plane G is l' . h is a horizontal line, and the projection on the image plane G is h' . The antenna pitch angle is the angle α between l and h , and it can be converted into the angle α' between l' and h' . Suppose l' and h' intersect at point $A(x_1, y_1)$, take a point $B(x_2, y_2)$ on l' and take a point $C(x_3, y_3)$ on h' , and then the antenna pitch angle α can be calculated by the following formula:

$$\alpha = \cos^{-1} \frac{\overline{AB} \cdot \overline{AC}}{|\overline{AB}| \times |\overline{AC}|}. \quad (1)$$

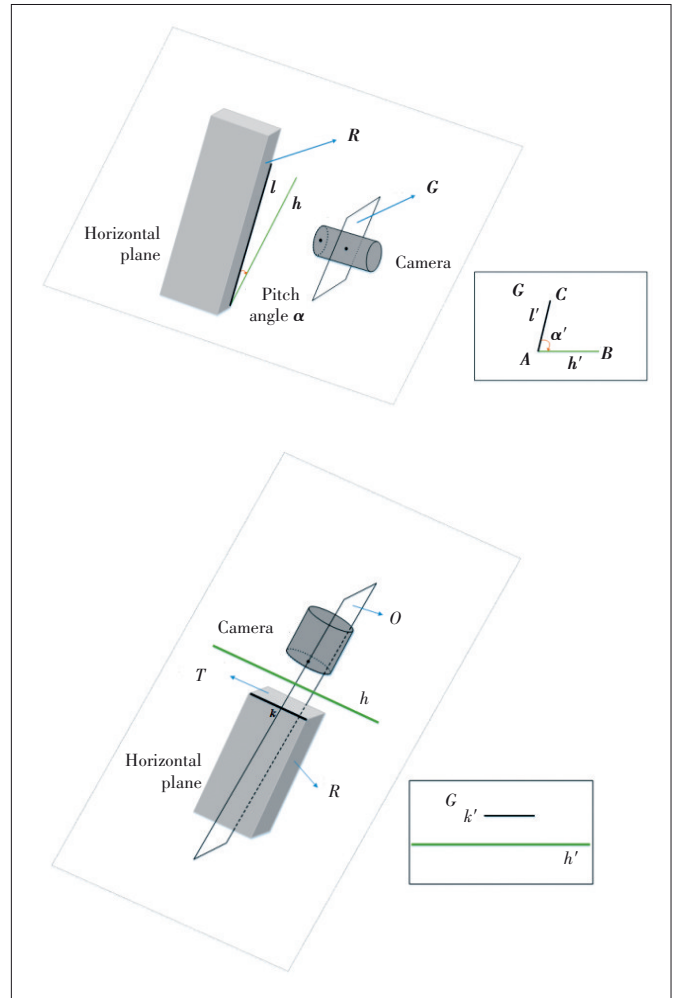
2) The azimuth angle of the antenna. In space, the azimuth angle β can be converted to the angle between the top rectangle and the direction of the north pole of the magnetic field in the image taken by the drone from its top view, which is usually defined as the azimuth angle of the sector antenna. From the plane view, it can be regarded as the angle obtained by rotating the top rectangle of the antenna target clockwise along the vertical direction indicated by true north.

According to the drone's related sensors and GPS position, we can obtain the drone's heading angle as θ , and the antenna azimuth angle β can be calculated by the following formula.

$$\beta = (\theta + 180) \% 360. \quad (2)$$

The value range of θ and β is $[0, 360)$, where 0 means facing true north, 90 means facing true east, 180 means facing true south, and 270 means facing true west.

To sum up, when we use the SSD algorithm to complete the antenna object intelligent detection in the image, we will obtain the classification of the antenna image while locating the object. When the object is classified as an antenna side, the corresponding pitch angle parameter is calculated; when the object is classified as an antenna top, the corresponding azimuth angle parameter is calculated. In this way, we can achieve an intelligent and automated calculation method that can reduce the cost of manual measurement.



▲ Figure 5. Calculation of angles

4 Experiments

In this part, we will present details of the experiment on the two phases of our algorithm.

4.1 Experiments on First Phase

4.1.1 Standard of Evaluation

The output of an object detection task usually includes the classification results, the confidence of each classification, the coordinates of the prediction frame, etc. According to the characteristics of the output results, precision P and recall R are selected as the main standards of evaluation.

The precision rate refers to the ratio of the true positive samples in the correctly identified samples; the recall rate refers to the ratio of the correct identification in all positive samples. It can be calculated mainly through the confusion matrix of the classification results, as shown in Table 1.

In the process of object detection, judging positive samples and negative samples is not as simple as the classification problem, and it needs to be judged according to the classification confidence and threshold of the prediction result. The re-

▼Table 1. Confusion matrix of the results

	Predicted Positive Samples	Predicted Negative Samples
Real positive samples	TP	FN
Real negative samples	FP	TN

FN: false negative FP: false positive TN: true negative TP: true positive

sults that indicate that the detection is correct mainly include the following samples. True positive (TP) is a positive sample, and the intersection over union (IoU) is greater than the set threshold; True negative (TN) is a negative sample and the IoU is greater than the set threshold. On the contrary, false positive (FP) and false negative (FN) are the corresponding cases of detection errors. During the experiment in this paper, the IoU threshold is set to 0.5.

Therefore, the calculation formulas for precision and recall are defined as follows:

$$\text{Precision} = \frac{TP}{TP + FP},$$

$$\text{Recall} = \frac{TP}{TP + FN}.$$
(3)

In fact, when conducting large-scale experiments, in order to evaluate the performance of the algorithm more comprehensively, the average precision (AP) is usually used for measurement, and the average of all APs of the detection classification is calculated to get the mean average precision mAP, which is most commonly used as the standard of evaluation. The mAP can better prevent some classifications from being too extreme to weaken others. Therefore, we choose the mAP as our object detection model.

4.1.2 Experiment Results and Analysis

In the experiment, we use the Mobile-SSD model proposed in Section 2 and YOLO and SSD models to train and test on the antenna data set under the same hardware conditions. The detection objects include the antenna side and the antenna top.

In the training phase, we collect a total of 1 832 original antenna images including antennas under different backgrounds and lighting conditions. What's more, through data augmentation, the total number of images that can be used for training reaches 3 856. The training epoch of each network model reached 1×10^5 times. The convergence speed of the Mobile-SSD model is fast and stable, which proves the model has strong adaptability to datasets and has great stability.

In the testing phase, 500 images were selected as the test dataset. The trained model was applied to detect the antenna side and the antenna top surface respectively. Table 2 mainly shows the accuracy of each model. The AP value and the overall mAP value of several algorithms are shown in Table 2 and Fig. 6.

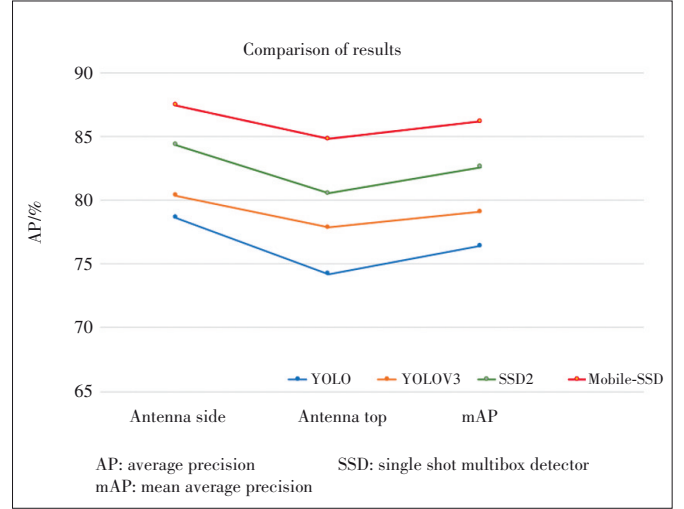
The experiment results show that the model proposed in the

▼Table 2. Comparison of results of the accuracy of each model

Network Structure	Antenna Side	Antenna Top	MAP
YOLO	78.62%	74.21%	76.42%
YOLOV3	80.34%	77.85%	79.10%
original SSD	84.34%	80.52%	82.58%
Mobile-SSD	87.42%	84.78 %	86.18%

mAP: mean average precision SSD: single shot multibox detector

YOLO: You Only Look Once



▲Figure 6. Comparison of results

paper is more accurate compared with the two models of the YOLO series. This is mainly due to the improvement of the detection details of the SSD network's anchor mechanism and the high efficiency of the candidate frame mechanism. Compared with the original SSD network, the addition of prior information about antennas makes Mobile-SSD more accurate.

In conclusion, the results prove that the improvement strategy proposed in this paper is feasible and accurate. However, we find in the experiments that the detection accuracy of the network decreases when there exist obstacles. The current antenna object detection network implemented has a good effect only in identifying unobstructed and intact antennas.

4.2 Experiments on Second Phase

4.2.1 Pitch Angle Measurement Experiment

The main goal of the experiment in this section is to verify the feasibility and correctness of the proposed scheme for measuring the pitch angle of the sector antenna. In the experiment, the sector antenna model is used for indoor measurement experiments. First, manually adjust the antenna attitude to obtain different elevation angles and use the inclinometer to manually read and record them as the reference value of each group of experiments, and then use the measurement system to perform measurement calculations through the drone. A total of 5 sets of experiments with different pitch angles are performed. Each group of experiments performed 10 measure-

ments, and the difference between the obtained measurement value and the reference value was used as the error value for analysis.

The experiment results and the error values obtained from each group of experiments are shown in Fig. 7.

4.2.2 Azimuth Angle Measurement Experiment

The main goal of the experiment in this section is to verify the feasibility and correctness of the proposed scheme for measuring the azimuth angle of the sector antenna. In the experiment, the sector antenna model is used for indoor measurement experiments. First, manually adjust the antenna attitude to obtain different azimuth angles, read the parameters using the mechanical compass and record them as the reference value of each experiment. And then use the measurement system to perform measurement calculations through the drone. A total of 5 sets of experiments with different azimuth angles are performed. Each group of experiments performed 10 times, and the difference between the obtained measurement value and the reference value is used as the error value for analysis.

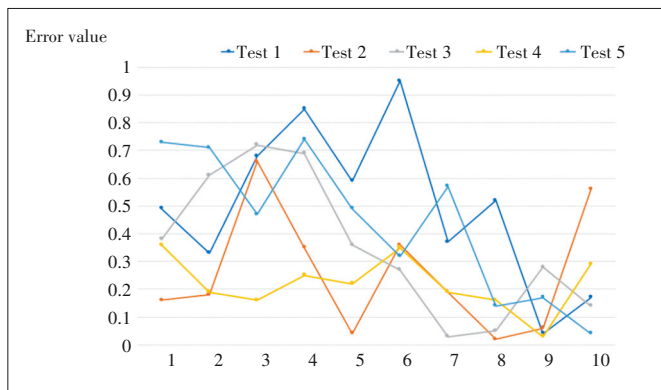
The experiment results and the error values obtained from each group of experiments are shown in Fig. 8.

4.2.3 Comparison to Existing Schemes

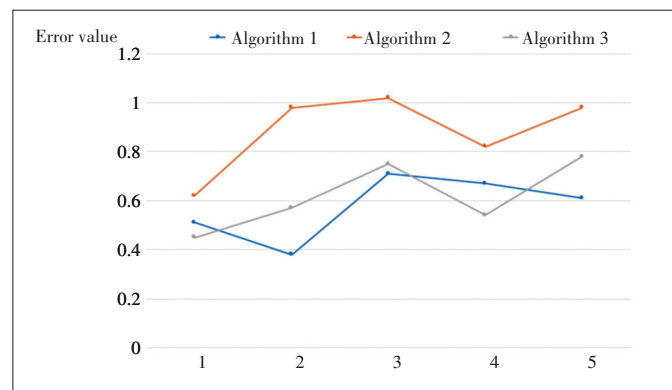
The experiment in this section is to compare the algorithm proposed in the paper (Algorithm 1) with the existing anten-

na attitude measurement algorithm, including a non-contact antenna attitude measurement scheme based on the 3D reconstruction and rendezvous measurement proposed by WANG^[8] (we refer it as Algorithm 2) and an image antenna attitude measurement scheme based on the drone's aerial photography proposed by ZHOU^[9] (we refer it as Algorithm 3). The main experimental method is to manually adjust the attitude angle of the fixed antenna model and measure the pitch angle and the azimuth angle using different schemes. The results are compared and analyzed. The results are drawn as a line graph for a more intuitive comparative analysis, which is shown in Figs. 9 and 10.

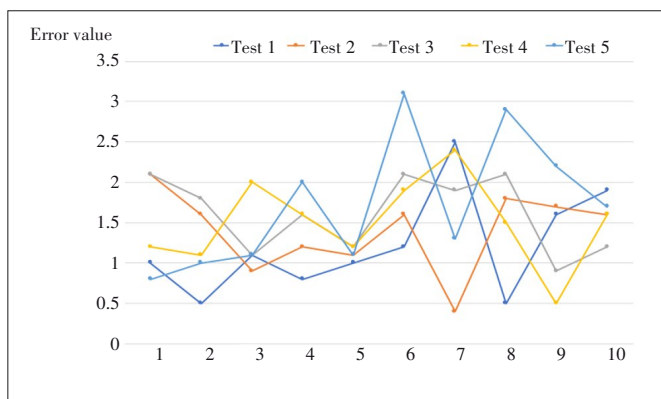
From the experiment results, the pitch angle error in the measurement of the scheme in the paper is basically within the range of 1° , and the azimuth angle error is basically within the range of 5° . Compared with other methods in the pitch angle experiment, the difference of the detection error is not large, and it can meet the standards required by the industry. The performance in the azimuth experiment is much better than Algorithm 2 which proves the effectiveness of our method. Algorithm 3 has relatively good measurement accuracy in two experiments and has a similar error value with Algorithm 1. However, manual intervention is required for antenna location using Algorithm 3 while Algorithm 1 automatically locates the antenna position through the SSD network. When the hardware can be guaranteed, Algorithm 1 may have better performance.



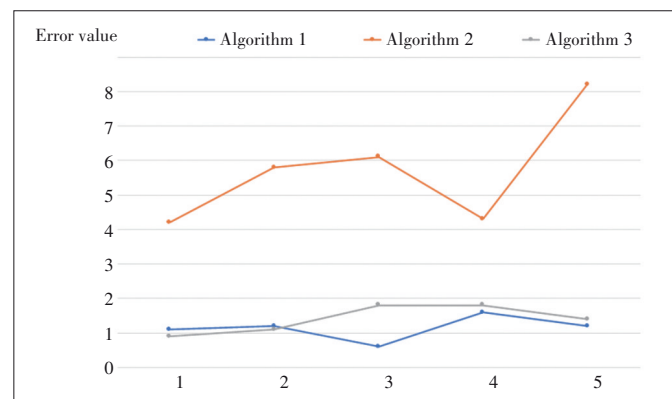
▲ Figure 7. Result of the pitch angle measurement experiment



▲ Figure 9. Pitch angle measurement comparison



▲ Figure 8. Result of the azimuth angle measurement experiment



▲ Figure 10. Azimuth angle measurement comparison

5 Conclusions

In this paper, we propose a novel antenna attitude parameters measurement algorithm, which can be divided into an antenna location phase and an attitude parameter calculation phase. Compared with traditional methods, we apply deep learning algorithms to the measurement, which achieves the function of automatic positioning of the antenna and reduces manual intervention in the measurement process. Experiment results show that the accuracy and efficiency of the proposed algorithm outperform those of existing methods. In addition, the measurement accuracy reaches the industry standard, which shows that the proposed algorithm can be applied in real applications.

In the future, we will conduct our studies from the following aspects: 1) optimizing the deep learning detection model to make it more efficient and accurate; 2) investigating the automatic cruise of drones based on deep learning; 3) automatically identifying whether antennas are affected by external factors such as obstruction, damage and bad weather.

Reference

- [1] MAO Y Y, YOU C S, ZHANG J, et al. A survey on mobile edge computing: the communication perspective [J]. *IEEE communications surveys & tutorials*, 2017, 19(4): 2322 – 2358. DOI: 10.1109/COMST.2017.2745201
- [2] REDMON J, DIVVALA S, GIRSHICK R, et al. You only look once: unified, real-time object detection [C]//*IEEE Conference on Computer Vision and Pattern Recognition*. IEEE, 2016: 779 – 788. DOI: 10.1109/CVPR.2016.91
- [3] LIU W, ANGUELOV D, ERHAN D, et al. SSD: Single shot multibox detector [C]//*European Conference on Computer Vision*. ECCV, 2016: 21-37. DOI: 10.1007/978-3-319-46448-0_2
- [4] SIMONYAN K, ZISSERMAN A. Very deep convolutional networks for large-scale image recognition [J]. *Computer science*, 2014
- [5] HOWARD A G, ZHU M L, CHEN B, et al. MobileNets: efficient convolutional neural networks for mobile vision applications [EB/OL]. [2021-04-16]. <https://arxiv.org/abs/1704.04861>
- [6] PAO D C W, LI H F, JAYAKUMAR R. Shapes recognition using the straight line Hough transform: Theory and generalization [J]. *IEEE transactions on pattern analysis and machine intelligence*, 1992, 14(11): 1076 – 1089. DOI: 10.1109/34.166622
- [7] GIOI R G VON, JAKUBOWICZ J, MOREL J M, et al. LSD: A fast line segment detector with a false detection control [J]. *IEEE transactions on pattern analysis and machine intelligence*, 2010, 32(4): 722 – 732. DOI: 10.1109/TPAMI.2008.300
- [8] WANG M L. Pose measurement with multiple-view space geometry [D]. Xidian University, 2017
- [9] ZHOU M. Attitude measurement of antenna based on the UAV aerial images [D]. Xidian University, 2019

Biographies

FAN Guotian (fan.guotian@zte.com.cn) received his M.Sc. degree in network systems from University of Sunderland, UK in 2008. Currently he is working as a deputy director in ZTE Corporation, China. His research interests include big-data mining, deep learning of digital image, intelligent planning and optimization of wireless network.

WANG Zhibin received his master's degree in computer science and technology from Xidian University, China in 2020. He is now a Ph.D. candidate of computer science and technology, Xidian University. His main research interests include database SQL engine & executor related machine learning and deep learning, spatio-temporal data retrieval, data analysis, and image analysis and processing.



Multi-Task Learning with Dynamic Splitting for Open-Set Wireless Signal Recognition

Abstract: Open-set recognition (OSR) is a realistic problem in wireless signal recognition, which means that during the inference phase there may appear unknown classes not seen in the training phase. The method of intra-class splitting (ICS) that splits samples of known classes to imitate unknown classes has achieved great performance. However, this approach relies too much on the predefined splitting ratio and may face huge performance degradation in new environment. In this paper, we train a multi-task learning (MTL) network based on the characteristics of wireless signals to improve the performance in new scenes. Besides, we provide a dynamic method to decide the splitting ratio per class to get more precise outer samples. To be specific, we make perturbations to the sample from the center of one class toward its adversarial direction and the change point of confidence scores during this process is used as the splitting threshold. We conduct several experiments on one wireless signal dataset collected at 2.4 GHz ISM band by LimeSDR and one open modulation recognition dataset, and the analytical results demonstrate the effectiveness of the proposed method.

Keywords: open-set recognition; dynamic method; adversarial direction; multi-task learning; wireless signal

XU Yujie¹, ZHAO Qingchen¹,
XU Xiaodong¹, QIN Xiaowei¹,
CHEN Jianqiang²

(1. University of Science and Technology of China,
Hefei 230026, China;

2. ZTE Corporation, Shenzhen 518057, China)

DOI: 10.12142/ZTECOM.2022S1007

<http://kns.cnki.net/kcms/detail/34.1294.>

tn.20220125.1740.005.html, published online
January 27, 2022

Manuscript received: 2021-07-05

Citation (IEEE Format): Y. J. Xu, Q. C. Zhao, X. D. Xu, et al., "Multi-task learning with dynamic splitting for open-set wireless signal recognition," *ZTE Communications*, vol. 20, no. S1, pp. 44 – 55, Jan. 2022. doi: 10.12142/ZTECOM.2022S1007.

1 Introduction

With the rapid development of wireless communication technology, the wireless spectrum is getting crowded, especially in the Industrial, Scientific and Medical (ISM) band which is open to the public and takes no authorization. A large number of wireless communication signals share the ISM band, such as Wi-Fi, Bluetooth and ZigBee. These coexisting signals interfere with each other and may cause performance reduction to the communication system^[1]. The technology of wireless signal recognition (WSR) is a foundational work to deal with this problem. The WSR technology can be used to identify the wireless signal and hence help to improve the communication system by choosing a better channel or other strategies.

Traditional algorithms of WSR could mainly be separated

into two groups: likelihood-based and feature-based methods^[2]. Likelihood-based methods obtain the optimal decision based on hypothesis testing theory but suffer high computation complexity^[3-4]. Feature-based methods usually extract several features and employed classifiers to realize signal recognition. These features are normally chosen using expert's knowledge. Although feature-based methods may not be optimal, they are usually simple to implement, with near-optimal performance, when designed properly. Feature-based methods heavily rely on expert's knowledge, which may perform well on specialized solutions but poor in generality^[5-6]. With the increasing number of wireless signals in the ISM band, communication systems tend to be complex and diverse. As a result, traditional feature-based methods used to detect and recognize the complex signals are confronted with a new dilemma.

In recent years, the method of deep learning has emerged and achieved great success in the fields of image, speech, text and so on. Deep learning is an end-to-end approach that can automatically learn signal representation directly from the original wireless data without the need for designing expert

This work was supported by the Natural Science Foundation of Anhui Province under Grant No. 2008085MF213 and ZTE Industry-University-Institute Cooperation Funds under Grant No. 20190822003.

features such as high-order cyclic moments. Inspired by the advantages of deep learning compared to conventional feature-based approaches, more and more researchers use deep learning methods to solve the problem of WSR. Generally, these deep learning methods utilize raw data obtained from devices such as channel state information (CSI) [7–8] and In-phase/Quadrature (I/Q) data [9–10] as the input of a deep neural network. However, most of these methods are under a close-set assumption that the classes in the inference phase all appear in the training phase, which is impractical. When facing a real scene, we have to deal with classes not seen in the training phase (also known as unknown unknown classes (UUCs) while KKC means known known classes [11]). As shown in Fig. 1, six classes from the modulation recognition dataset [12] are selected as KKC during the training phase and all eleven classes are served as testing samples during the inference phase. It challenges the traditional classifiers that they have to predict the unknown classes as one of the known class. In fact, the UUCs will be labeled as one of the KKC with high probability, generally. Therefore, the purpose of open-set recognition (OSR) is to identify unknown classes while correctly classify known classes [13].

The difficulty of OSR is that there is no knowledge of UUCs during the training stage. Current OSR methods mainly fall into two main categories: discriminative methods and generative methods. The discriminative methods choose an empirical threshold based on samples of KKC to determine whether testing samples belong to KKC or UUCs [14]. To take full advantage of the knowledge of KKC, a few studies use Extreme Value Theory (EVT) to model the tail of evaluation scores so as to determine a better threshold [15–17]. The discriminative

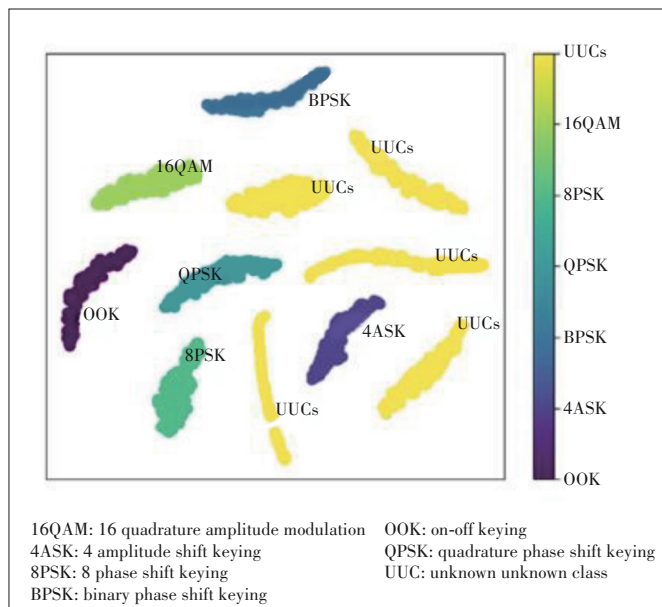
methods are sensitive to thresholds but there is no principle of how to choose thresholds. Furthermore, the generative methods utilize a generative model to generate fake data as UUCs [18–20]. The fake data is used in the training phase together with the known data, thus the OSR problem is turned into an $N+1$ classification problem. In addition, the intra-class splitting (ICS) method selects a certain percentage of samples from known data as atypical samples to imitate UUCs. This method is simple and efficient but also has some drawbacks. For instance, it is very sensitive to the predefined splitting ratio and the method of directly using splitting samples as UUCs is coarse. Besides, the performance of the ICS method degrades significantly in a new environment. We intend to address these drawbacks in this article.

Multi-task learning trains multiple tasks at the same time and uses shared representations to learn the common ideas between a collection of related tasks [21]. There are few literatures studying multi-task learning (MTL) in OSR [22–24]. Most of these studies use discriminative methods applied in the image field and thresholds are calculated based on KKC. Specifically, some researchers train two tasks simultaneously, one for the traditional close-set classification task and the other for evaluating testing samples. The evaluation score of the second task is compared with the threshold to determine whether it belongs to KKC or UUCs. Besides, the auxiliary task is used to force the network to learn more informative features to improve separation of classes from each other and from KKC. Different from the above works, we propose an MTL network based on the characteristics of communication signals on a generative method to improve the performance of open-set classifier.

In this paper, we propose an MTL network with a dynamic method to determine the splitting ratio for the OSR problem. The splitting ratio will be used to split known data into two subsets: inner samples and outer samples, which are applied to imitate UUCs [25]. The contributions of the proposed method are described as follow: Firstly, we propose an MTL network based on the characteristic of wireless signal to improve the OSR performance in new environment. Secondly, we provide a dynamic method to automatically select the splitting ratio. Specifically, we perturb a sample from the center of one class toward its adversarial direction and the change point of confidence scores during this process is used as the splitting threshold. Thirdly, we perform numerical experiments to demonstrate the effectiveness of the proposed method.

2 Related Work

This paper studies the OSR problem of wireless signals by using an MTL network with the dynamic splitting method. Some studies are related to this work. We will review these studies in three subsections that present the research of WSR, OSR, MTL, respectively.



▲ Figure 1. An example of known known classes (KKCs) and UUCs using t-SNE (t-distributed stochastic neighbor embedding)

2.1 Wireless Signal Recognition

WSR is a fundamental task to enable any form of cross-technology ISM band signals' coexistence mechanism. Traditional feature based algorithms extract features for preprocessing and then employ them to realize classification. PALICOT et al. used channel bandwidth and its shape as reference features, which was found to be the most discriminating parameter among others^[5]. KIM et al. used cyclostationary features that was caused by the periodicity in the signal or in its statistics like mean and autocorrelation or they can be intentionally induced to assist spectrum sensing^[6]. However, these algorithms rely heavily on expert's knowledge to extract features and are poor in generality.

On the other hand, deep learning based approaches have shown great advantages in terms of performance and no need for expert's knowledge. These approaches utilize different information to train deep neural networks. YI et al. used Received Signal Strength Indication (RSSI) values as input data to train a Convolutional Neural Network (CNN) classifier^[26]. The proposed model can achieve an accuracy of over 93% for detecting the different classes of interference with minimal computational resources. KIM et al. used k-nearest neighbor (kNN) and neural networks to train models with CSI values as the input^[7]. The proposed model can classify tens of signal sources with over 90% accuracy. CROCE et al. adopted the artificial neural network, with which a Wi-Fi device could detect the presence of an LTE-U signal by examining the error pattern of a received Wi-Fi signal^[27]. The proposed method reached an average accuracy of over 95% in recognizing ZigBee, microwave, and LTE (in unlicensed spectrum) interference. In Ref. [9], a CNN classifier trained on In-phase/Quadrature (IQ) vectors and amplitude/phase vectors can recognize ZigBee, Wi-Fi, and Bluetooth signals and achieve an average accuracy of more than 98% in a high signal-to-noise ratio (SNR) scenario. Thus we choose IQ data as the input of deep neural network considering its rich information. However, open-set recognition of WSR is rarely studied, which is very common in real world.

2.2 Open-Set Recognition

The discriminative methods usually identify unknown samples based on an empirical threshold. MENDES et al.^[14] introduced an open set version of Nearest Neighbor classifier (OS-NN) to deal with the OSR problem based on the traditional Nearest Neighbor classifier. Some studies used the extreme value theory (EVT) to model the tail of data so as to determine a better threshold. BENDALE and BOULT^[15] proposed the OpenMax model by replacing the SoftMax layer with an OpenMax layer. Specifically, the training samples' distances from their corresponding class mean activation vectors (MAV) are calculated and used to fit the separate Weibull distribution for each class. SCHEIRER et al.^[16] proposed a Weibull-Calibrated SVM (W-SVM) model, which combined the statistical

eEVT for score calibration with two separated SVMs. YOSHIHASHI et al.^[17] presented the classification-reconstruction learning algorithm for open set recognition (CROSR), which utilized latent representations for reconstruction and enabled robust UUCs' detection without harming the KKC's classification accuracy. However, these EVT-based methods provide no principled means of selecting the size of tail for fitting.

The generative methods usually use generative neural networks to generate fake data imitating UUCs. Although such methods suffer from the difference between the fake data generated by generative models and the real data of UUCs, they are still highly promising to turn an OSR problem into an $N+1$ classification problem. Counterfactual image generation (OS-RCD)^[18] adopts an encoder-decoder GAN architecture to generate the synthetic open set examples that are close to KKC's, yet do not belong to any KKC's. JO et al.^[19] adopted the GAN technique to generate fake data as the UUCs' data to further enhance the robustness of the classifiers for UUCs. The ICS method^[28] used a pretrained close-set network to score known samples and select atypical samples as samples of UUCs. In the meantime, a closed regular term was proposed in order to ensure the accuracy of close-set classification. Although the ICS method is simple and effective, the selection of atypical samples is very sensitive to the predefined splitting ratio and pretrained network. SCHLACHTER et al.^[29] proposed a one-stage method based on alternating between ICS and the training of a deep neural network, which removed the need for the pretrained network but still relied on the predefined splitting ratio. MIYATO et al.^[30] provided a fast way to calculate the adversarial direction of the current network. Here, the adversarial direction for a given datum is the direction to which the probabilities of each class change most and it is toward the decision boundary^[31]. Inspired by the DICS method and adversarial direction, we propose a novel dynamic method to automatically select the splitting ratio.

2.3 Multi-Task Learning

In recent years, some researchers have tried to use multi-tasking learning to solve the open-set recognition problem. PERERA et al.^[22] proposed a multi-task network to learn more descriptive features where an auxiliary classifier performed self-supervision. The self-supervision task had to determine which transformation was applied and thus the network needed to learn structural properties of image content such as shape and orientation. OZA et al.^[23] combined a classifier network and a decoder network with a shared feature extractor network within a multi-task learning framework. Reconstruction errors from the decoder network were utilized for open-set rejection and the tail of the reconstruction error distribution from KKC's was modeled by the EVT to improve the overall performance. YU et al.^[24] proposed a multi-task curriculum learning framework to perform the task of detecting out-of-distribution samples and semi-supervised learning. The in-distribution

bution samples in unlabeled data having small out-of-distribution scores were selected and used with labeled data for training the deep neural networks in a semi-supervised manner. SONG et al.^[32] proposed a framework incorporating GAN with a multi-task discriminator, which simultaneously discriminates category, reality, and client identity of input samples. In this paper, based on the characteristics of communication signals, we propose an MTL network on a dynamic generative method.

3 Proposed Method

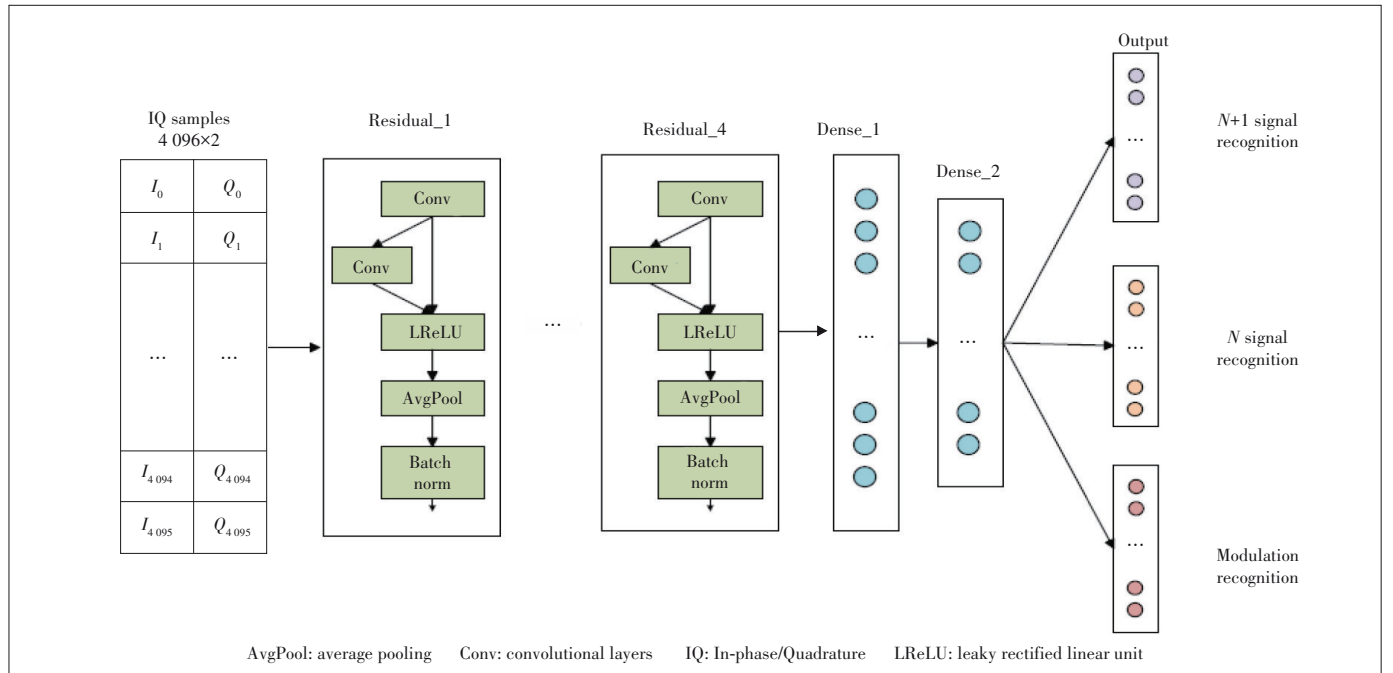
In this section, we first describe the MTL network architecture of our method, and then we present the dynamic method to automatically select the splitting ratio. Finally, we demonstrate the procedure of the proposed scheme.

3.1 MTL Network

To deal with the OSR problem of WSR, we propose an MTL network architecture (Fig. 2). Inspired by the idea of ICS, we use dynamically split samples to imitate unknown classes, and thus turn the OSR problem into an $(N+1)$ -class signal recognition task. However, the split samples are actually from known classes and their new labels differ from the ground truth. Hence, a naive neural network with $(N+1)$ -class output will result in low closed-set accuracy, because the split samples are incorrectly predicted. To prevent this situation, we take the same strategy as that proposed in Ref. [28] of training a closed-set regularization subnetwork simultaneously which forces the split samples to be correctly classified. Meanwhile, in order to mitigate the decline of identification accuracy of a trained net-

work applied in new scenes, we introduce an auxiliary task of modulation recognition to learning more generalized expression. The MTL network consists of one shared deep neural network and three individual task-specific layers. The purpose of the $(N+1)$ -class signal recognition task is to classify all testing samples, including KKC and UUCs, where the $(N+1)$ -th class represents UUCs and is trained with dynamically split samples with data augmentation. The modulation recognition task is designed as an auxiliary task to help learn more generalized expression. Besides, we keep the N -class signal recognition task of classifying known classes to guarantee a high closed-set classification performance. The shared deep neural network is composed of four residual blocks and two dense layers. Each residual block includes two convolutional layers (Conv), an activation layer with a leaky rectified linear unit (LReLU), an average pooling (AvgPool) and a batch normalization layer. Each of three individual task-specific layers contains one output layer. The MTL network takes IQ data samples as the input and maps them to a specific category. The dimensions of one sample are 4096×2 . In the inference phase, only the $(N+1)$ -class signal recognition task is used as an end-to-end classifier for open-set recognition.

Formally, given a training set of samples x_i , where i indicates one of the known N classes, we divide x_i into two subsets: inner samples $x_{i,inner}$ and outer samples $x_{i,outer}$ using the dynamic splitting method. The number of outer samples is too small to learn knowledge about UUCs at the beginning of training. To keep the network training in a good direction, we employ data augmentation on the outer samples. The augmented outer samples $x_{i,aug}$ are served as samples of unknown classes



▲ Figure 2. Multi-task learning (MTL) network architecture of the proposed method

with a new label y_{N+1} while the inner samples $x_{i,inner}$ are also used to train the $(N+1)$ -class signal recognition task. In the meantime, all x_i are used as the input of the N -class signal recognition task and modulation recognition task with the original label y_i . The cross entropy loss functions of three tasks are denoted as:

$$L_{OS} = -\frac{1}{B} \sum_{b=1}^B \sum_{j=1}^{N+1} y_{OS}^{(b)}(j) \log(\hat{y}_{OS}^{(b)}(j)), \quad (1)$$

$$L_{CS} = -\frac{1}{B} \sum_{b=1}^B \sum_{j=1}^N y_{CS}^{(b)}(j) \log(\hat{y}_{CS}^{(b)}(j)), \quad (2)$$

$$L_{MR} = -\frac{1}{B} \sum_{b=1}^B \sum_{j=1}^{N'} y_{MR}^{(b)}(j) \log(\hat{y}_{MR}^{(b)}(j)), \quad (3)$$

where B indicates the batch size of one epoch. $y_{OS}^{(b)}(j)$ and $\hat{y}_{OS}^{(b)}(j)$ present the j -th element of a true one-hot type OSR label and the predicted one of the b -th sample, by which the augmented outer samples are assigned with UUCs label. Meanwhile, y_{CS} and y_{MR} are the true signal category label and modulation category label of known classes. Therefore, the loss function of the shared deep neural network is given as:

$$L_{total} = \alpha L_{OS} + \beta L_{CS} + \lambda L_{MR} + \eta L_2, \quad (4)$$

where L_2 represents the L_2 -norm regularization term. The total loss L_{total} is a linear combination of the loss of each task and regularization term. α, β, λ and η indicate the weight of each item. By training with shared weights, the deep neural network can learn generalized expression between multiple related tasks. Consequently, minimizing the first term forces the network to classify between the inner and outer samples, i.e., completing the task of open-set recognition. On the other hand, minimizing the second and third terms corresponds to reducing the empirical risk on the known classes. Hence, the classifier learns to identify unknown classes while correctly classifying known classes.

3.2 Dynamic Splitting Method

The original ICS method^[28] is restricted to the predefined splitting ratio and pretrained network. The improved version^[29] removes the restriction on the pretrained network but still relies on the predefined splitting ratio. In this subsection, we propose a dynamic method to automatically select the splitting ratio by continuously perturbing samples toward the adversarial direction of current network. An approximate curve of confidence score and deviation during this process is constructed and the change point of this curve is acquired and used to determine the splitting ratio.

First, we select some candidate samples of the class center by ranking the evaluation confidence score of known samples.

Formally, let $f(x)$ represent the predicted probability of a trained classifier on sample x , which is one-dimensional vector after softmax. The confidence score represents the degree to which the sample belongs to the category. The higher the score, the more centralized the sample is. It is denoted as:

$$\text{score} = \max(f(x)) \cdot I(f_{oh}(x) = y), \quad (5)$$

where y is the label, $f_{oh}(x)$ is the predicted result in one-hot and $I(\cdot)$ is an indicator function that returns 1 if the predicted class is the same as the true label and otherwise returns 0. We choose several samples per class with the highest score as candidate samples of the class center. Then we continuously disturb these samples toward adversarial direction to generate adversarial samples. Here, the adversarial direction for a given datum is the direction to which the probabilities of each class change most and it is toward the decision boundary^[31]. The adversarial direction $r_{adv}(x, \varepsilon)$ for given ε is calculated by

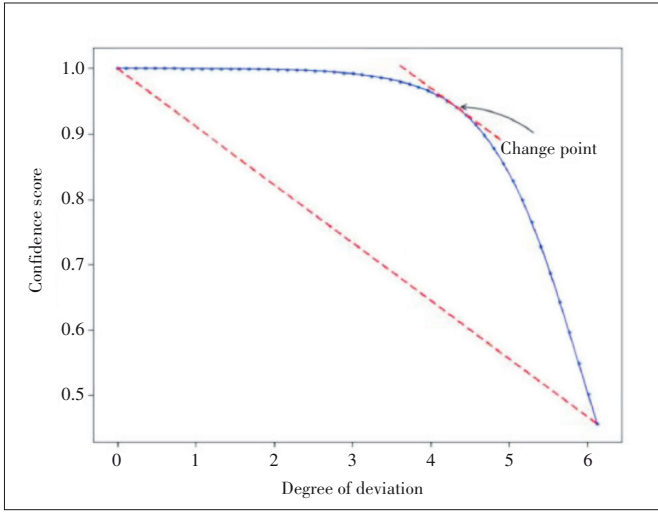
$$r_{adv}(x, \varepsilon) = \arg \max_{r: \|r\| \leq \varepsilon} D_{KL}(f(x) \| f(x+r)), \quad (6)$$

where D_{KL} indicates Kullback-Leibler divergence and r indicates slight perturbation constrained by parameter ε ; $f(x)$ and $f(x+r)$ represent the predicted probabilities of the samples before and after perturbation. Generally, it is hard to obtain a closed form for the exact adversarial direction r_{adv} , so we use a fast approximation method to compute it the same as in Ref. [30]. Thereby, the adversarial samples are formulated as

$$x_{adv}(\delta) = x + \delta r_{adv}(x, \varepsilon) / \|r_{adv}(x, \varepsilon)\|, \quad (7)$$

where δ is a parameter that denotes the degree of disturbance toward the adversarial direction. We continuously vary this parameter to generate adversarial samples from the center of a class to the decision boundary. The scores of adversarial samples will be calculated and used to approximate a curve.

As shown in Fig. 3, the horizontal axis shows the degree to which the sample deviates from the center of one class, and the vertical axis shows the corresponding confidence score. When the sample of class is moved away from the center, the confidence score begins to plummet at some points. Similar to Ref. [33], the point with the furthest distance from the straight line connected by two points of the maximum and minimum confidence scores, is selected as the change point. Thereby, the sample whose confidence score is lower than the change point is selected as the outer sample. The change point is improper and the candidate sample should be discarded if the confidence score is almost constant within a certain range of disturbance or the confidence score of change point is less than 0.9. The former means this sample is hard to achieve the decision boundary toward current approximate adversarial direction. For convenience, we abandon this kind of candidate



▲ Figure 3. An example of confidence score approximate curve

samples. The latter usually indicates this sample is not in the center of class while the confidence scores of the most known samples are normally higher than 0.9, which will lead to too many outer samples. To prevent this situation, we also abandon this kind of candidate samples. When the candidate samples of one class drop more than a certain number, which means that the current network may not be trained well, the samples of this class will not be split and all used as inner samples to retrain the network. After a certain period of training, the splitting ratio of the neural network is adjusted by the method above until the stable performance is achieved.

It may happen that the outer samples are too many or too few so that the neural network becomes worse and worse or remains unchanged during the training process. To avoid such a situation, we choose to set a maximum splitting ratio and perform data augmentation for the segmented samples. In our experiment, the maximum splitting ratio was set to 0.2 and the automatically calculated splitting ratio exceeding the threshold will be limited to 0.2. In Ref. [34], three augmentation methods based on the characteristics of modulated signals are considered, i.e., rotation, flip, and Gaussian noise, and remarkable results are achieved. We choose to use a combination of these methods to enhance the outer samples. The enhanced outer samples are randomly chosen at an appropriate amount.

3.3 Training Procedure

The proposed scheme enhances the generalization ability of the network by using multi-task learning and dynamically selects the splitting ratio. The training procedure of the proposed scheme is summarized in Algorithm 1. The input of this scheme are samples of known classes including data and multiple labels. At first, we pretrain the $(N+1)$ -class classifier $f_{OS}(\cdot)$ with N -class data x since there is no samples of unknown classes in the training data. Then we utilize the pretrained classifier $f_{OS}(\cdot)$ to evaluate all samples as Eq. (5) and a few sam-

ples with the highest score of each class are selected as candidate samples. We continuously disturb the candidate sample toward its adversarial direction of the current network and record the confidence score to approximate a curve. The change point of this curve is modified as splitting ratio ρ if it is appropriate. The samples with confidence scores less than ρ are selected as x_{outer} and the rest are x_{inner} . The data x_{outer} are enhanced to $x_{outer, aug}$ using the method of rotation, flip, and Gaussian noise. The $f_{OS}(\cdot)$ is retrained with x_{inner} served as KKC and $x_{outer, aug}$ served as UUCs. At the same time, the $f_{CS}(\cdot)$ and $f_{MR}(\cdot)$ with x , y_{CS} and y_{MR} are trained to learn a generalized expression. The loss functions are shown as Eqs. (2), (3) and (4). The $f_{OS}(\cdot)$ is then used to calculate the splitting ratio ρ again until the performance of the open-set classifier is stable. Finally, only the $(N+1)$ -class network is used as the open-set classifier.

Algorithm 1. Proposed scheme

Inputs:

- x : Data of KKC
- y_{CS} : Signal type label of KKC
- y_{MR} : Modulation type label of KKC

Output:

$f_{OS}(\cdot)$: Open-Set Classifier

- 1: Pretrain the $(N+1)$ -class classifier $f_{OS}(\cdot)$ with x and y_{CS} , where all KKC are used as inner samples
- 2: Calculate the splitting ratio ρ of each class using the proposed dynamic method based on $f_{OS}(\cdot)$
- 3: Modify the splitting ratio and split x into two subsets: x_{inner} and x_{outer} . Enhance the data x_{outer} to x_{aug}
- 4: Train $f_{OS}(\cdot)$ with x_{inner} and x_{aug} that assigned with new labels. Meanwhile, train $f_{CS}(\cdot)$ and $f_{MR}(\cdot)$ with x , y_{CS} and y_{MR} to learn a generalized expression.
- 5: Return to 2 until the stable performance is achieved.

4 Experiment

In the section, we will firstly introduce the two wireless signal datasets used in our experiment. The evaluation criteria of the proposed method are shown next. Then we describe six baseline methods including four state-of-the-art methods from the literature and two variations with different configurations for comparison. Finally, a number of experimental results and analysis are presented.

4.1 Datasets

A wireless signal dataset collected at 2.4 GHz ISM band by LimeSDR and a publicly available modulation dataset, which are used for evaluating the performance of the proposed model, are detailed in this section. For convenience, we use WS to represent the wireless signal dataset and RML to represent the radio modulation dataset.

The dataset of WS contains 10 kinds of signals that mainly work on the 2.4 GHz unlicensed frequency band, namely Wi-

Fi, ZigBee, Bluetooth, microwave oven, analog video monitor, narrowband digital signal, wideband OFDM signal, game control signal, cordless phone signal and wideband FM signals. We collect the IQ orthogonal data of all classes except for narrowband digital signals and wideband OFDM signals by using a LimeSDR receiver to receive wireless signals from different transmitters. The seven main transmitters are shown in Fig. 4. From top to bottom and left to right, they are microwave oven, ZigBee, smartphone, game controller, analog video monitor, cordless phone and camera. The smartphone is used for transmitting Bluetooth and Wi-Fi signals. The analog video monitor together with the camera is used for creating wideband FM signals. Besides, the narrowband digital and wideband OFDM signal are both generated by MATLAB R2019a, where non-ideal power amplifiers are considered therein. The nonlinearity of the power amplifier is modeled in a memoryless polynomial form. Each class is collected at six scenes including line-



▲ Figure 4. Pictures of main transmitters used in WS dataset collection

▼ Table 1. WS dataset parameters

Signal Types	Scenes	Frequency	Bandwidth	Samples per Classes
Wi-Fi, Bluetooth, cordless phone, wide-band FM, ZigBee, microwave oven, analog video monitor, narrow-band digital signal, wide-band OFDM signal, game control signal	Line-of-sight (1, 3, 5, 7 m); Non-line-of-sight (1, 3 m)	2.442 GHz	20 MHz	7 500

OFDM: orthogonal frequency-division multiplexing WS: the wireless signal dataset

▼ Table 2. RML dataset parameters

Normal Classes	Difficult Classes	Sample Length	SNR Range	Samples per Classes
OOK, 4ASK, BPSK, QPSK, 8PSK, 16QAM, AM-SSB-SC, AM-DSB-SC, FM, GMSK, OQPSK	OOK, 4ASK, 8ASK, BPSK, QPSK, 8PSK, 16PSK, 32PSK, 16APSK, 32APSK, 64APSK, 128APSK, 16QAM, 32QAM, 64QAM, 128QAM, 256QAM, AM-SSB-WC, AM-SSB-SC, AM-DSB-WC, AM-DSB-SC, FM, GMSK, OQPSK	1 024	-20 dB to 30 dB	106 496
AM: amplitude modulation APSK: amplitude phase shift keying ASK: amplitude shift keying BPSK: binary phase shift keying	DSB: double sideband FM: frequency modulation GMSK: Gaussian filtered minimum shift keying OOK: on-off keying	OQPSK: offset- quadrature phase shift keying PSK: phase shift keying QAM: quadrature amplitude modulation QPSK: quadrature phase shift keying	RML: the radio modulation dataset SC: suppressed carrier SSB: single side band WC: with carrier	

of-sight (LOS) and non-line-of-sight (NOS) conditions with different communication distances between the transmitter and the LimeSDR receiver. The synthetic signal is added noise with corresponding degree to simulate six collecting scenes. Table 1 shows the specific dataset collection settings of different signals including the center frequency, bandwidth and communication distance between the transmitter and receiver. Furthermore, each class has 7 500 samples of which there are 1 250 samples for each scenes and the dimensions of each sample are 4 096×2.

To further verify the performance of the proposed method, we also test it on one public modulation signal dataset. O'SHEA et al.^[12] provide two different types of the datasets, both of which are synthetically generated datasets using GNU Radio with commercially used modulation parameters. Some realistic channel imperfections are included in the datasets, including channel frequency offset, sample rate offset, and additive white Gaussian noise along with multipath fading. The "Normal" dataset consists of 11 classes that are all with relatively low information density and are commonly seen in impaired environments. These 11 signals can be used for classification tasks at a high SNR. The "Difficult" dataset contains 24 modulations. These include a number of high order modulations (QAM256 and APSK256), which are used in the real world in very high SNR and low-fading channel environments. Detailed specifications and generation details of the datasets can be found in Ref. [12]. The specific modulations along with the parameter list can be found in Table 2. The dimensions of one sample are 1 024×2. In this paper, we use 4 096 samples each class of one high SNR scene in the Normal dataset to train the proposed network and use samples of different SNR scenes to test the performance of the trained network. We design a related task of distinguishing the modulation type of phase modulation, frequency modulation and amplitude modulation to help the task of modulation recognition learn richer knowledge.

4.2 Evaluation

In the field of open-set recognition, there are N known classes and K unknown classes. The concept of openness is to define how open the problem is^[13]. Larger openness corresponds to more open problems, while the problem is completely closed when the openness equals 0. We changed the number of N and K to get different openness in the following experiments. The openness is denoted by O , and its definition is the same as that in Ref. [13] and can be simplified to:

$$O = 1 - \sqrt{\frac{2N}{2N + K}}. \quad (8)$$

The close-set accuracy P is used to evaluate the performance of an close-set recognizer and denoted as

$$P = \frac{1}{m} \sum_{j=1}^m I(f(x^j) = y^j), \quad (9)$$

where m is the total number of known samples. x^j and y^j represent the j -th sample of known classes and the corresponding label. The balanced accuracy (T) is used to evaluate the performance of an open-set recognizer. T balances the accuracy of unknown classes and unknown classes with the same weights. Accordingly, it is defined as

$$T = \frac{1}{2} \left(P + \frac{1}{n} \sum_{k=1}^n I(f(x^k) = y^k) \right), \quad (10)$$

where n is the total number of unknown samples. x^k and y^k represent the k -th sample of unknown classes and the corresponding label. In the end, the area under curve (A) is taken into consideration for keeping consistent with prior studies.

4.3 Baseline Methods

We selected five baseline methods including three state-of-the-art methods from the literature and two variations with different configurations for comparison. In the baseline methods, six categories of both datasets are selected as KKC during the training phase and all categories are used in the inference phase. The networks are basically the same as that in Fig. 2 but with different tasks. The Adam optimizer is adopted among these methods and the batch size is set to 32. The ratio of training set to testing set is set to 4:1.

1) Intra-class splitting (ICS): The ICS method was implemented in Ref. [28]. The pretrained network is similar to the proposed network but only has the N -class classifier. The network with the best performance was saved during 50 pretraining epochs. The splitting ratio was set to 0.2 for both datasets and the training epochs of open-set network was set to 100.

2) Dynamic intra-class splitting (DICS): The DICS method was implemented in Ref. [29]. The hyper-parameters were set the same as those for ICS.

3) Open-set interference signal recognition using boundary

samples (OSISR): The OSISR method was implemented in Ref. [25]. The hyperparameter ε used in adversarial-sample generation was equal to 10^{-6} and the corresponding learning rate η and the number of iteration epochs were set to 0.01 and 100. The splitting ratio μ of adversarial samples was selected as 80 for both datasets.

4) Deep CNN-based multi-task learning for open-set recognition (MLOS): The MLOS method was implemented according to Ref. [23]. We modified the network structure to fit the sample shape of WS and RML datasets. The hyperparameters were kept as those in Ref. [23]. The MLOS method is a discriminative method and does not have an open-set classifier. So we just evaluated T and P of this method.

5) ICS with data augmentation (ICS-aug): In order to explore the difference between the proposed dynamic splitting method and the predefined method, we consider ICS-aug the same as the proposed method to get rid of the impact of data augmentation. The method of data augmentation consists of rotation, flip, and Gaussian noise. The hyperparameters were kept the same as those in Ref. [34].

6) The proposed method without MTL (P-w/o MTL): In order to explore the importance of using MTL, we considered to train a network without MTL as a baseline. The difference between using or not using MTL is whether modulation recognition task is employed. Specifically, the loss function of the proposed method without MTL is given as:

$$L_{\text{total}} = \alpha L_{OS} + \beta L_{CS} + \eta L_2, \quad (11)$$

where the symbol meanings are the same as those in the proposed method. The performance of the trained network with and without MTL was measured in new scenes.

4.4 Basic Experiment

Firstly, the proposed method and the other baselines were compared on both the datasets. In each experiment on one dataset, we selected six classes as the known classes used in the training phase and all classes were used in the testing phase to evaluate the capabilities of network. Each experiment was repeated three times and the means and standard deviations (STD) of evaluation were reported.

The results with performance metrics (STD) on both datasets are shown in Table 3. The proposed method outperforms four baseline methods and achieves comparable performance to the proposed method without MTL. Specifically, the proposed method achieved an improvement of T by more than 4% on the WS dataset and by more than 7% on the RML dataset compared with the state-of-the-art method OSISR. The method of ICS-aug has an increase of T by about 2% than OSISR on the WS dataset, which indicates that the operation of data augmentation effectively expands the simulated samples of unknown classes. Meanwhile, the proposed method has better performance of T by about 2% on the RML dataset compared with ICS-aug, which means that the dynamic method of select-

▼Table 3. Results with performance metrics (STD)

Metrics	Dataset	ICS/%	DICS/%	OSISR/%	MLOSIR/%	ICS-aug/%	P-w/o MTL/%	Proposed/%
T	WS	91.2(± 1.1)	91.5(± 0.7)	93.1(± 0.5)	81.6(± 0.3)	95.0(± 0.6)	97.1(± 1.3)	97.2(± 0.9)
	RML	88.7(± 3.0)	88.6(± 2.3)	90.3(± 2.1)	80.3(± 0.5)	96.3(± 2.1)	98.0(± 2.1)	97.9(± 2.3)
P	WS	92.3(± 0.9)	91.6(± 0.6)	93.2(± 0.4)	98.8(± 0.3)	95.3(± 0.5)	97.2(± 1.4)	97.3(± 1.0)
	RML	88.3(± 2.9)	87.8(± 2.1)	91.4(± 2.0)	98.6(± 0.4)	97.5(± 2.1)	98.3(± 1.9)	98.2(± 2.4)
A	WS	95.6(± 1.3)	96.0(± 1.0)	97.2(± 0.5)	-	98.5(± 0.9)	99.3(± 1.1)	99.4(± 0.8)
	RML	94.1(± 3.1)	94.0(± 2.9)	91.3(± 3.4)	-	98.8(± 2.3)	99.8(± 2.2)	99.8(± 2.4)

DICS: dynamic intra-class splitting
ICS: intra-class splitting
ICS-aug: ICS with data augmentation

MLOSIR: deep CNN-based multi-task learning for open-set recognition
OSISR: open-set interference signal recognition using boundary samples
P-w/o MTL: the proposed method without multi-task learning

RML: the radio modulation dataset
STD: standard deviation
STWS: the wireless signal dataset

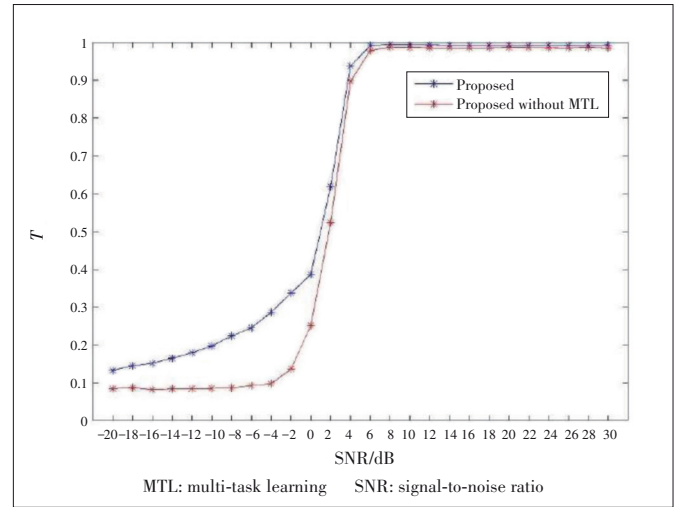
ing the splitting ratio is superior to the predefined method by automatically selecting the suitable splitting ratio of each class. Thereby, we argue that the proposed method can automatically select the appropriate splitting ratio per training period. This means that more precise outer samples are selected for imitating unknown classes, which leads to better performance of the open-set recognizer on more complex datasets.

P is a measurement of the ability of an open-set recognizer to correctly classify a sample from known classes while A is a measurement of the effect of the open-set classifier. As shown in Table 3, P and A show a similar trend as T and the proposed method outperforms the other baseline methods except the method of not using MTL. The values of A are generally larger than those of P and the proposed method seems to be more superior for the RML dataset. Besides, the MLOSIR method achieves the best performance of P , due to its use of a close-set classifier to classify known classes.

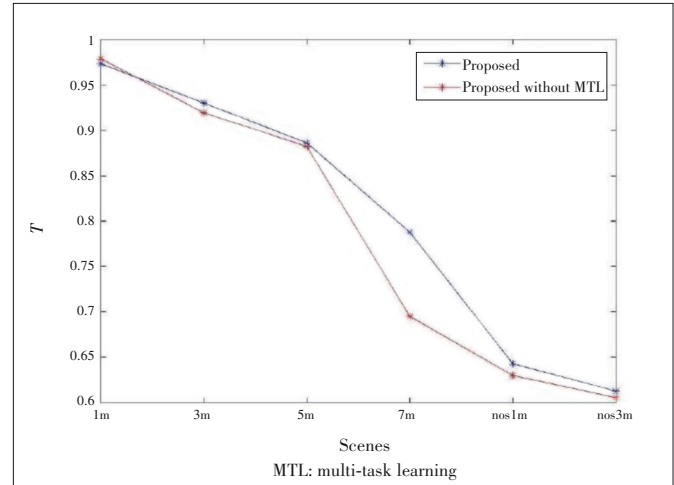
4.5 MTL Experiment

We also compared the performance of the proposed method using MTL and that not using MTL in new scenes. We used part of the WS dataset collected in the scene of LOS condition with 1 m communication distance to train the networks and the samples of the other five scenes were used to test the performance. Different kinds of signals in the training set have different SNRs and the total SNR of the training set ranges from 20 dB to 50 dB. As for the RML dataset, we use the samples with an SNR equal to 8 dB to train the two kinds of networks and test them with other 25 scenes with various SNRs from -20 dB to 30 dB.

The results of the proposed methods with and without MTL trained on one scene and tested on other collecting scenes on two datasets are shown in Figs. 5 and 6. Firstly, on the RML dataset, the networks trained in the 8 dB SNR scene maintained their performance in higher SNR scenes. Secondly, the performance declined rapidly with the decrease of SNR from 4 dB to -4 dB and then tended to be stable on the RML dataset. While on the WS dataset, T also decreased with the increase of communication distance and complexity. Thirdly, the MTL method had a comparable performance with the method not using it in higher SNR scenes but outperforms in



▲ Figure 5. T of proposed methods with and without MTL on the radio modulation dataset (RML) dataset



▲ Figure 6. T of proposed methods with and without MTL on the wireless signal dataset (WS) dataset

low SNR scenes on both datasets. Specifically, the proposed method achieved an improvement of T by about 10% on the scene “7 m” of the WS dataset and by more than 10% on the scene “-2 dB” of the RML dataset. Thereby, we argue that the proposed method can benefit from learning shared ex-

pression of a collection of related tasks and improve the performance in new scenes.

4.6 Openness Experiment

Openness is an important parameter in the problem of OSR, which describes how open an OSR problem is. The definition of openness is denoted as in Eq. (8). On the RML dataset, we used six classes from the Normal dataset to train the network and used different numbers of unknown classes from the Difficult dataset to test. Specifically, the number of KKC's were set from 1 to 18. In this case, a larger number of UUCs means larger openness. While on the WS dataset, we used different numbers of classes as KKC's to train the network and the rest were served as UUCs on the WS dataset. The number of KKC's was chosen from 3 to 9 and the corresponding openness was from 0.32 to 0.03.

The results of the proposed method and two baseline methods under different openness on each dataset are shown in Figs. 7 and 8, respectively. It can be seen that the performance of three methods decreases with the increase of openness. This is because that the proportion of KKC's and all classes becomes small so that it is difficult to learn enough knowledge from KKC's. The accuracy of KKC's stays high but the accuracy of recognizing UUCs gets lower and T declines. Besides, the performance of the proposed method outperforms the other two baseline methods regarding T . As discussed before, this improvement is brought by the efficient data augmentation and better robustness of the proposed method that is achieved by dynamic splitting ratio determining.

4.7 Data Augmentation Experiment

In order to solve the problem that there are too few outer samples at the beginning of the training process and to make the experiment in a good direction, we used the method of data augmentation to enhance the split outer samples. The specific methods are basically the same as those in Ref. [34]. In this work, we evaluate the effects of different data augmentation methods on the proposed method under different scenes.

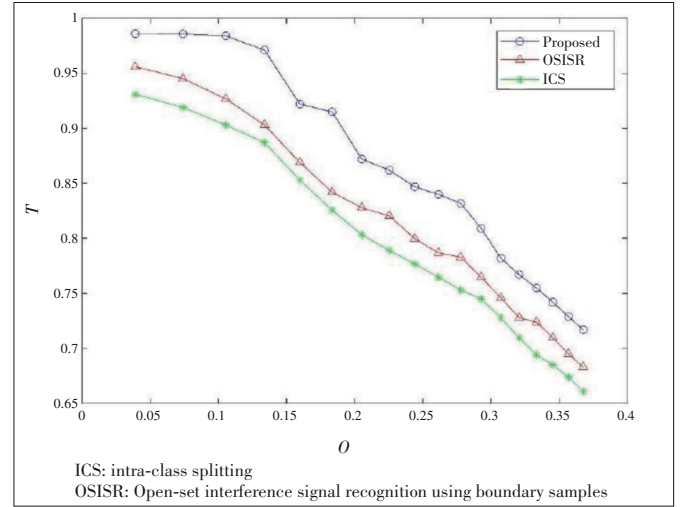
Formally, let (I, Q) represent the original IQ orthogonal signal, which has a length of 1 024 in the RML dataset, and (\hat{I}, \hat{Q}) represent the augmented signal. According to the rotation formula in two dimensional planes, the rotated signal is defined as:

$$\hat{I} = I \cos \theta - Q \sin \theta, \quad \hat{Q} = I \sin \theta + Q \cos \theta, \quad (12)$$

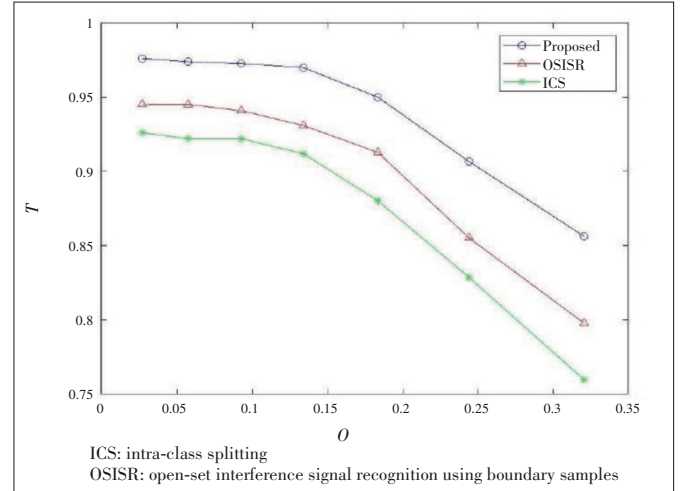
where θ is the angle of rotation, which was set to $\pi/2$, π , and $3\pi/2$. The flip of a signal is given as:

$$\hat{I} = \pm I, \quad \hat{Q} = \mp Q. \quad (13)$$

The two types of flips were both used in this study. We also augmented signal samples by adding a Gaussian noise. The



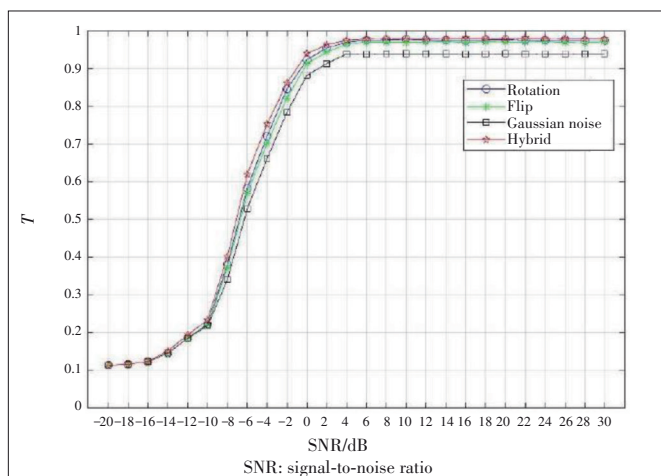
▲ Figure 7. T of the proposed, OSISR and ICS methods under different O on the radio modulation dataset (RML) dataset



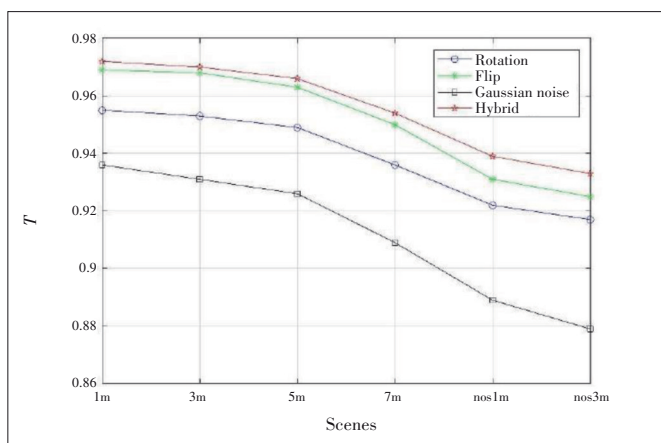
▲ Figure 8. T of the proposed, OSISR and ICS methods under different O on the wireless signal dataset (WS) dataset

standard deviation of the Gaussian noise was set to 0.000 1, 0.000 5 and 0.001. Besides, we also considered a combination of three methods and only part of the augmented samples were randomly selected to keep the data balanced.

Figs. 9 and 10 show the T of the proposed method using four data augmentation methods trained on different scenes of two datasets. It can be seen that the performance declined under low-SNR or complex scenes. On both datasets, the hybrid method achieves the greatest performance at a higher SNR (≥ -8 dB). The rotation and flip data augmentation methods achieve secondary performance and the noise data augmentation method performs the worst. Intuitively, adding Gaussian noise reduces the SNR of the original data sample, which in turn generates more signal samples with low SNRs. However, the improvement of the noise method is trivial because the resulting classification accuracy in a low SNR is small. Therefore, the hybrid approach was selected for our experiments.



▲ Figure 9. T of proposed methods using different data augmentation methods on the radio modulation dataset (RML)



▲ Figure 10. T of proposed methods using different data augmentation methods on the wireless signal dataset (WS)

5 Conclusions

In this paper, we propose an MTL network with dynamical splitting ratio determining for wireless signal open-set recognition. Specifically, the dynamic method automatically selects the splitting ratio per class by continuously perturbing class center samples toward the adversarial direction of the current network. The change point of a sample's confidence score during this process is acquired and used to determine the splitting threshold. After adjusting improper splitting thresholds, the original samples of KKC's with higher scores than the threshold are selected as inner samples while the rest are served as outer samples. We use a hybrid data augmentation method to enhance the outer samples, which are used to imitate UUCs later. The network will keep training using the latest splitting data until the performance is stable. Besides, we simultaneously train the original signal classification task and the auxiliary modulation classification task using the MTL method. By learning a shared expression of the related tasks, the network extracts generalized feature and improves the performance loss when applied in a new environment. We conducted our ex-

periments on one wireless signal dataset collected at 2.4 GHz ISM band by LimeSDR and one open modulation recognition dataset. The results of different experiments show the superiority of the proposed method over state-of-the-art methods regarding a compromise of closed set accuracy and rejection capability. The experiments indicate that the proposed method still has poor performance in high openness, although it is better than baseline methods. Therefore, future work could focus on improving the identification accuracy under high openness.

References

- [1] RAYANCHU S, PATRO A, BANERJEE S. Airshark: detecting non-WiFi RF devices using commodity WiFi hardware [C]//ACM SIGCOMM conference on Internet measurement conference. ACM, 2011: 137 - 154. DOI: 10.1145/2068816.2068830
- [2] LI X F, DONG F W, ZHANG S, et al. A survey on deep learning techniques in wireless signal recognition [J]. Wireless communications and mobile computing, 2019, 2019: 5629572. DOI: 10.1155/2019/5629572
- [3] DOBRE O A, HAMEED F. Likelihood-based algorithms for linear digital modulation classification in fading channels [C]//Canadian Conference on Electrical and Computer Engineering. IEEE, 2006: 1347 - 1350. DOI: 10.1109/CCECE.2006.277525
- [4] CHAVALI V G, SILVA C R C MDA. Maximum-likelihood classification of digital amplitude-phase modulated signals in flat fading non-Gaussian channels [J]. IEEE transactions on communications, 2011, 59(8): 2051 - 2056. DOI: 10.1109/TCOMM.2011.051711.100184
- [5] PALICOT J, ROLAND C. A new concept for wireless reconfigurable receivers [J]. IEEE communications magazine, 2003, 41(7): 124 - 132. DOI: 10.1109/MCOM.2003.1215649
- [6] KIM K, AKBAR I A, BAE K K, et al. Cyclostationary approaches to signal detection and classification in cognitive radio [C]//IEEE International Symposium on New Frontiers in Dynamic Spectrum Access Networks. IEEE, 2007: 212 - 215. DOI: 10.1109/DYSPAN.2007.35
- [7] KIM Y, AN S, SO J. Identifying signal source using channel state information in wireless LANs [C]//International Conference on Information Networking (ICOIN). IEEE, 2018: 616 - 621. DOI: 10.1109/ICOIN.2018.8343192
- [8] YANG Z S, WANG Y X, ZHANG L J, et al. Indoor interference classification based on WiFi channel state information [C]//Proc. International Conference on Security, Privacy and Anonymity in Computation, Communication and Storage. Springer, 2018: 136 - 145. DOI: 10.1007/978-3-030-05345-1_11
- [9] KULIN M, KAZAZ T, MOERMAN I, et al. End-to-end learning from spectrum data: A deep learning approach for wireless signal identification in spectrum monitoring applications [J]. IEEE access, 2018, 6: 18484 - 18501. DOI: 10.1109/ACCESS.2018.2818794
- [10] RIYAZ S, SANKHE K, IOANNIDIS S, et al. Deep learning convolutional neural networks for radio identification [J]. IEEE communications magazine, 2018, 56(9): 146 - 152. DOI: 10.1109/MCOM.2018.1800153
- [11] NAYLOR A R. Known knowns, known unknowns and unknown unknowns: a 2010 update on carotid artery disease [J]. The surgeon, 2010, 8(2): 79 - 86. DOI: 10.1016/j.surge.2010.01.006
- [12] O'SHEA T J, ROY T, CLANCY T C. Over-the-air deep learning based radio signal classification [J]. IEEE journal of selected topics in signal processing, 2018, 12(1): 168 - 179. DOI: 10.1109/JSTSP.2018.2797022
- [13] GENG C X, HUANG S J, CHEN S C. Recent advances in open set recognition: A survey [J]. IEEE transactions on pattern analysis and machine intelligence, 2021, 43(10): 3614 - 3631. DOI: 10.1109/TPAMI.2020.2981604
- [14] MENDES JÚNIOR P R, SOUZA R M, DE O WERNECK R, et al. Nearest neighbors distance ratio open-set classifier [J]. Machine learning, 2017, 106

- (3): 359 – 386. DOI: 10.1007/s10994-016-5610-8
- [15] BENDALE A, BOULT T E. Towards open set deep networks [C]//IEEE Conference on Computer Vision and Pattern Recognition. IEEE, 2016: 1563 – 1572. DOI: 10.1109/CVPR.2016.173
- [16] SCHEIRER W J, ROCHA A, MICHEALS R J, et al. Meta-recognition: The theory and practice of recognition score analysis [J]. IEEE transactions on pattern analysis and machine intelligence, 2011, 33(8): 1689 – 1695. DOI: 10.1109/TPAMI.2011.54
- [17] YOSHIHASHI R, SHAO W, KAWAKAMI R, et al. Classification-reconstruction learning for open-set recognition [C]//IEEE/CVF Conference on Computer Vision and Pattern Recognition (CVPR). IEEE, 2019: 4011 – 4020. DOI: 10.1109/CVPR.2019.00414
- [18] NEAL L, OLSON M, FERN X, et al. Open set learning with counterfactual images [C]//Proc. European Conference on Computer Vision (ECCV). Springer, 2018: 613 – 628
- [19] JO I, KIM J, KANG H, et al. Open set recognition by regularising classifier with fake data generated by generative adversarial networks [C]//IEEE International Conference on Acoustics, Speech and Signal Processing. IEEE, 2018: 2686 – 2690. DOI: 10.1109/ICASSP.2018.8461700
- [20] YU Y, QU W Y, LI N, et al. Open-category classification by adversarial sample generation [EB/OL]. (2017-06-17) [2020-10-15]. <https://arxiv.org/abs/1705.08722>
- [21] CRAWSHAW M. Multi-task learning with deep neural networks: A survey [EB/OL]. (2020-09-10)[2021-10-15]. <https://arxiv.org/pdf/2009.09796.pdf>
- [22] PERERA P, MORARIU V I, JAIN R, et al. Generative-discriminative feature representations for open-set recognition [C]//IEEE/CVF Conference on Computer Vision and Pattern Recognition (CVPR). IEEE, 2020: 11811 – 11820. DOI: 10.1109/CVPR42600.2020.01183
- [23] OZA P, PATEL V M. Deep CNN-based multi-task learning for open-set recognition [EB/OL]. (2019-03-07)[2020-10-15]. <https://arxiv.org/abs/1903.03161>
- [24] YU Q, IKAMI D, IRIE G, et al. Multi-task curriculum framework for open-set semi-supervised learning [C]//European Conference on Computer Vision. Springer, 2020: 438 – 454. DOI: 10.1007/978-3-030-58610-2_26
- [25] XU Y J, QIN X W, XU X D, et al. Open-set interference signal recognition using boundary samples: A hybrid approach [C]//International Conference on Wireless Communications and Signal Processing (WCSP). IEEE, 2020: 269 – 274. DOI: 10.1109/WCSP49889.2020.9299700
- [26] YI S, WANG H, XUE W Q, et al. Interference source identification for IEEE 802.15.4 wireless sensor networks using deep learning [C]//29th Annual International Symposium on Personal, Indoor and Mobile Radio Communications. IEEE, 2018: 1 – 7. DOI: 10.1109/PIMRC.2018.8580857
- [27] CROCE D, GARLISI D, GIULIANO F, et al. Learning from errors: detecting cross-technology interference in WiFi networks [J]. IEEE transactions on cognitive communications and networking, 2018, 4(2): 347 – 356. DOI: 10.1109/TCCN.2018.2816068
- [28] SCHLACHTER P, LIAO Y W, YANG B. Open-set recognition using intra-class splitting [C]//27th European Signal Processing Conference (EUSIPCO). IEEE, 2019: 1 – 5. DOI: 10.23919/eusipco.2019.8902738
- [29] SCHLACHTER P, LIAO Y W, YANG B. Deep open set recognition using dynamic intra-class splitting [J]. SN computer science, 2020, 1(2): 1 – 12. DOI: 10.1007/s42979-020-0086-9
- [30] MIYATO T, MAEDA S I, KOYAMA M, et al. Virtual adversarial training: a regularization method for supervised and semi-supervised learning [J]. IEEE transactions on pattern analysis and machine intelligence, 2019, 41(8): 1979 – 1993. DOI: 10.1109/TPAMI.2018.2858821
- [31] KIM D, CHOI Y, KIM Y. Understanding and improving virtual adversarial training [EB/OL]. (2019-09-15)[2020-10-15]. <https://arxiv.org/abs/1909.06737>
- [32] SONG M K, WANG Z B, ZHANG Z F, et al. Analyzing user-level privacy attack against federated learning [J]. IEEE journal on selected areas in communications, 2020, 38(10): 2430 – 2444. DOI: 10.1109/JSAC.2020.3000372
- [33] ZACK G W, ROGERS W E, LATT S A. Automatic measurement of sister chromatid exchange frequency [J]. The journal of histochemistry and cytochemistry, 1977, 25(7): 741 – 753. DOI: 10.1177/25.7.70454
- [34] HUANG L, PAN W J, ZHANG Y, et al. Data augmentation for deep learning-based radio modulation classification [J]. IEEE access, 2019, 8: 1498 – 1506. DOI: 10.1109/ACCESS.2019.2960775

Biographies

XU Yujie received the B. Eng. and M. Eng. degree in electronic and information engineering from University of Science and Technology of China (USTC), China in 2017 and 2021. His research interest is deep learning for wireless signal identification.

ZHAO Qingchen received the B.Eng. degree in electronic information engineering from Anhui University of Finance and Economics, China in 2018. He is currently pursuing his M. Eng. degree in Department of Electronic Engineering and Information Science, University of Science and Technology of China (USTC), China. His research interest is smart transmission.

XU Xiaodong (xdxu@ustc.edu.cn) received the B.Eng. and Ph.D. degrees in electronic and information engineering from University of Science and Technology of China (USTC) in 2000 and 2007, respectively. From 2000 to 2001, he served as a research assistant at the R&D center, Konka Telecommunications Technology. Since 2007, he has been a faculty member with the Department of Electronic Engineering and Information Science, USTC. He is currently working with the CAS Key Laboratory of Wireless-Optical Communications, USTC. His research interests include the areas of wireless communications, signal processing, wireless artificial intelligence and information-theoretic security.

QIN Xiaowei received the B.S. and Ph.D. degrees from the Department of Electrical Engineering and Information Science, University of Science and Technology of China (USTC), China in 2000 and 2008, respectively. Since 2014, he has been a member of staff in Key Laboratory of Wireless-Optical Communications of Chinese Academy of Sciences at USTC. His research interests include optimization theory, service modeling in future heterogeneous networks, and wireless artificial intelligence in mobile communication networks.

CHEN Jianqiang received the M. Eng. degree from Nanjing University of Technology, China in electromagnetic field and microwave technology. At present, he works at the intelligent home terminal product line of ZTE Corporation and has many years of experience in the communication industry. His research direction is Wi-Fi key technologies and their applications, in which he has more than 10 patents.



Multi-Cell Uplink Interference Management: A Distributed Power Control Method

Abstract: This paper investigates a multi-cell uplink network, where the orthogonal frequency division multiplexing (OFDM) protocol is considered to mitigate the intra-cell interference. An optimization problem is formulated to maximize the user supporting ratio for the uplink multi-cell system by optimizing the transmit power. This paper adopts the user supporting ratio as the main performance metric. Our goal is to improve the user supporting ratio of each cell. Since the formulated optimization problem is non-convex, it cannot be solved by using traditional convex-based optimization methods. Thus, a distributed method with low complexity and a small amount of multi-cell interaction is proposed. Numerical results show that a notable performance gain achieved by our proposed scheme compared with the traditional one is without inter-cell interaction.

Keywords: uplink interference; multi-cell uplink network; non-cooperative game; interactive scheme

HU Huimin^{1,2}, LIU Yuan^{1,2}, GE Yiyang^{1,2},
WEI Ning^{3,4}, XIONG Ke^{1,2}

(1. School of Computer and Information Technology, Beijing Jiaotong University, Beijing 100044, China;
2. Beijing Key Laboratory of Traffic Data Analysis and Mining, Beijing 100044, China;
3. ZTE Corporation, Shenzhen 518057, China;
4. State Key Laboratory of Mobile Network and Mobile Multimedia Technology, Shenzhen 518055, China)

DOI: 10.12142/ZTECOM.2022S1008

<http://kns.cnki.net/kcms/detail/34.1294.TN.20220125.1546.003.html>, published online January 26, 2022

Manuscript received: 2021-08-08

Citation (IEEE Format): H. M. Hu, Y. Liu, Y. Y. Ge, et al., "Multi-cell uplink interference management: a distributed power control method," *ZTE Communications*, vol. 20, no. S1, pp. 56 – 63, Jan. 2022. doi: 10.12142/ZTECOM.2022S1008.

1 Introduction

In 5G and Internet of Things (IoT) networks, the number and density of users have increased dramatically and data transmission has shown explosive growth, leading to an urgent need for greater capacity and higher spectrum efficiency (SE)^[1-3], especially in the uplink transmission. For the uplink transmission, a cell user may suffer unacceptably high interference from other users in neighboring cells, who transmit signals over the same frequency band with it.

To pursue high SE and mitigate the inter-user interference, the orthogonal frequency division multiple access (OFDMA) protocol was proposed^[4]. OFDMA divides the

whole available channel frequency band into several sub-channels, so that multiple users can access over different sub-channels for data transmission simultaneously^[5-7]. In OFDMA-based cellular systems, when the number of sub-channels is greater than or equal to the total number of users in all cells, the intra-cell interference can be ignored, since the sub-channels are orthogonal to each other^[8].

However, in wireless cellular networks, due to the limited spectrum resource, different cells have to share the same spectrum resource. That is the users in different cells may transmit signals over the same sub-channel in an OFDMA-based cellular system so that the inter-cell interference (ICI) cannot be neglected, especially in the ultra-dense cellular system, where the radius of the cell is much smaller than traditional ones and the distance between the users from different cells is also smaller than traditional ones. Thus, in the ultra-dense cellular system, the inter-cell interference becomes the major factor of limiting the network capacity and users' achievable-information rates^[9-10]. More importantly,

This work was supported in part by the National Key R&D Program of China (No. 2020YFB1806903), by ZTE Industry-Academia-Research Cooperation Funds under Grant No. HC-CN-20191211004, by the National Natural Science Foundation of China (NSFC) (No. 62071033 and also by the Fundamental Research Funds for the Central Universities (No. 2020JBZD010). XIONG Ke is the corresponding author.

as the demand for spectrum resource utilization continues to increase, the ICI issue is getting much worse^[11].

As a matter of fact, the ICI is related to many factors including network topology, frequency reuse methods, multiple access schemes, and transmit power of users, among which the power control is shown to be the most significant way to migrate the ICI.

Moreover, in practical multi-cell networks, it is impossible to deploy a centralized power control algorithm due to the huge signaling overhead on collecting global network information from all users, so a lot of related work on multi-cell ICI suppression by designing distributed power control can be found in the literature^[12-18]. In Ref. [12], an efficient power allocation approach in OFDMA cellular networks was proposed, which was based on the non-cooperative game theory. In Ref. [13], the distributed power control and subcarrier allocation problems in the multi-cell OFDMA system were studied, and the convergence rule and steady state characterization were analyzed with the potential game. In Ref. [14], a power control scheme was proposed to manage the LTE uplink interference, which was designed based on data-driven machine learning paradigms. In Ref. [15], two power control schemes were proposed by adjusting the maximum transmit power of femtocell users to suppress the cross-tier interference at a macro-cell base station (BS). In Ref. [16], a new interference cancellation scheme was presented for the uplink multi-channel environment to reduce error propagation with low backhaul use, and the scheme shares one real value scaler and hard symbols through backhaul to minimize residual interference variance. In Ref. [17], the user's unique interference-aware open-loop power control (IA-OPC) scheme was proposed, in which the incoming and outgoing line interference in the cell were taken into account. In Ref. [18], the energy efficiency maximization problem was investigated under uncertain channels, for which an optimal mobile relay selection algorithm and a robust distributed power control algorithm were proposed.

However, the aforementioned works on the distributed power control did not take into account information interaction, so the achieved performance is limited. As is known, more efficient strategies can be designed based on more information interacted among cells. This paper aims to design a new distributed power control method for OFDMA-based multi-cell networks by introducing proper inter-cell interaction. Note that proper inter-cell interaction means that the less interaction amount, the better. The contributions of this paper are summarized as follows.

1) An optimization problem is formulated to maximize the user supporting ratio for the uplink multi-cell systems by optimizing the transmit power, where the OFDM protocol is considered for mitigating the intra-cell interference. Different from existing works^[12,17], the goal of which was to improve the network throughput, this paper adopts the user

supporting ratio as the main performance metric, which is described as the ratio between the number of users meeting the quality of service (QoS) threshold and the total number of users in the cell. If more users are supported, more profits can be gained by the communication network operators. Different from the existing work^[19], which examined the exact downlink average capacity of multi-cell MIMO cellular network with co-channel interference, this paper aims to design a simple and low-complexity multi-cell uplink interference management method.

2) Since the formulated optimization problem is non-convex and we aim to design a distributed method with low complexity and a small amount of multi-cell interaction, the problem cannot be solved by using traditional convex-based optimization methods. Thus, an interactive power control scheme is proposed based on the non-cooperative game. In the presented scheme, a power control scheme based on a non-cooperative game is introduced, and the predicted transmit power obtained by the non-cooperative game is shared. Hence, it has low complexity and a small amount of multi-cell interaction. Numerical results show that a notable performance gain is achieved by our proposed scheme compared with the traditional one without inter-cell interaction. In our simulation, it shows that the user supporting ratio obtained by the interactive scheme based on the non-cooperative game is higher than that obtained by the non-interactive scheme.

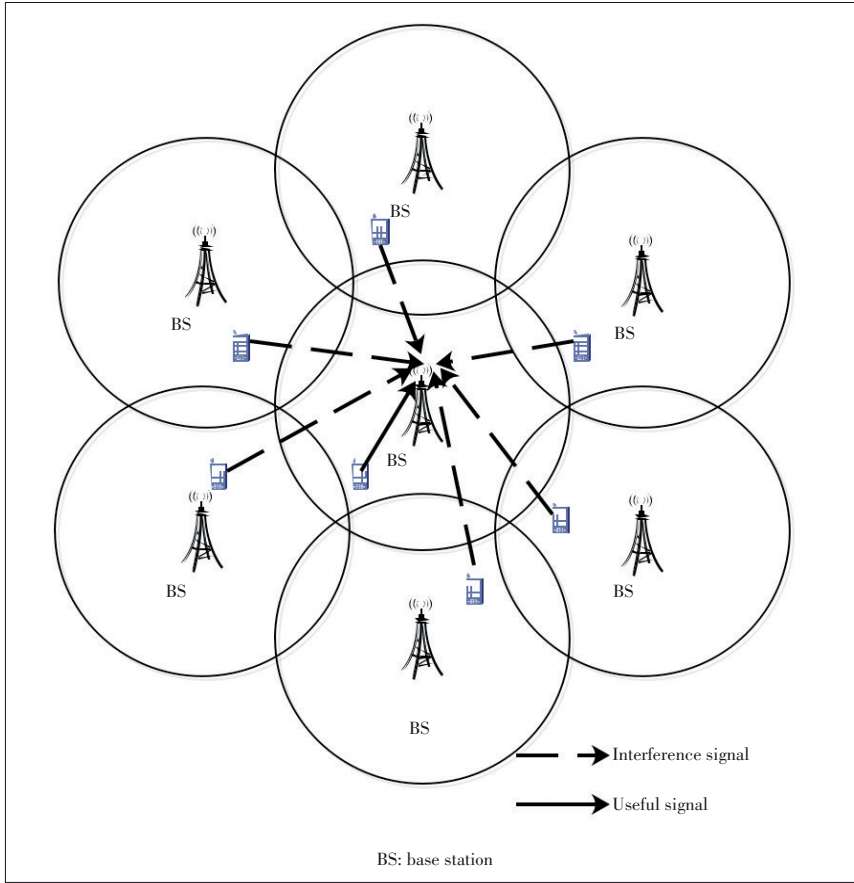
The rest of the paper is organized as follows. In Section 2, we present the system model and formulate the optimization problem. In Section 3, we present a distributed interactive uplink power control algorithm based on non-cooperative games. Section 4 proves the effectiveness of the proposed scheme via simulations. Section 5 summarizes the paper.

2 System Model

2.1 Network Model

We consider a multi-cell uplink transmission network, consisting of M cells/BSs, as shown in Fig. 1. In each cell, the number of users is N . Each BS in M cells performs uplink resource allocation to serve N randomly distributed users, with $m \in \{1, 2, \dots, M\}$, and $n \in \{1, 2, \dots, N\}$, where the OFDMA is used to avoid interference between users in the cell. In addition, due to limited spectrum resources, full spectrum multiplexing is used among multiple cells. Due to full frequency reuse among M cells, users in each cell suffer from co-channel interference imposed by frequency multiplexing users in other surrounding cells, where the radius of each cell is R , and the distance between adjacent base stations is D .

Assume that the total carrier number is C , and for fairness, carrier resources are evenly divided, so that N re-



▲ Figure 1. An illustration of a multi-cell uplink system

source blocks (RBs) with the same number of sub-carriers are obtained. The size of each RB is $L = C/N$. Each user is randomly assigned with an RB, and each sub-carrier could only be exclusively allocated to one user in each cell. Let B denote the total bandwidth of the system. Then, the bandwidth of per sub-carrier is $B_s = B/C$.

Let $P_{m,n}$ denote the transmit power of the n -th user in the m -th cell. It is assumed that the BS can measure the channel quality from users in the cell to the BS in the uplink transmission. Therefore, the signal to interference plus noise ratio (SINR) of the n -th user's l -th subcarrier in the m -th cell is

$$\gamma_{m,n,l} = \frac{P_{m,n} h_{m,n,l}}{I_{m,n,l} + N_0}, \quad (1)$$

where $h_{m,n,l}$ is the channel power gain of the n -th user's l -th subcarrier in the m -th cell, N_0 is the power spectral density of additive white Gaussian noise (AWGN) on the subcarrier, and $I_{m,n,l}$ is the total interference received by the n -th user's l -th subcarrier in the m -th cell.

The expression of $I_{m,n,l}$ is given by

$$I_{m,n,l} = \sum_{i=1, i \neq m}^M \sum_{n=1}^N \alpha_{i,n,l} P_{i,n} h_{i,n,l}^m, \quad (2)$$

where $\alpha_{i,n,l}$ is a binary variable, and $\alpha_{i,n,l} = 1$ if the n -th user's l -th subcarrier in the i -th cell interferes with the l -th subcarrier in the m -th cell. Otherwise, $\alpha_{i,n,l} = 0$. $h_{i,n,l}^m$ represents the power gain from n -th user's l -th subcarrier in the i -th cell to m -th BS.

Let $R_{m,n}$ denote the achievable rate of the n -th user in the m -th cell. Therefore, the achievable rate of the n -th user over the allocated RB in the m -th cell is given by

$$R_{m,n} = \sum_{l=1}^L B_s \log(1 + \gamma_{m,n,l}). \quad (3)$$

2.2 Problem Formation

Assume that each user has an expected minimum rate requirement $R_{m,n}^{\text{th}}$. If $R_{m,n} \geq R_{m,n}^{\text{th}}$, the user can get the desired QoS. Otherwise, user's QoS requirement cannot be satisfied. In the following, $R_{m,n}^{\text{th}}$ is defined as a QoS threshold to measure the QoS of the user. The goal is to maximize the user supporting ratio of each cell, which is defined as the ratio between the number of users meeting the QoS threshold and the total number of users in cell, i.e.,

$$p_m = \frac{N_m^{\text{sat}}}{N}, \quad (4)$$

where N_m^{sat} denotes the number of users whose achievable rate meet $R_{m,n} \geq R_{m,n}^{\text{th}}$ in the m -th cell.

Therefore, the user supporting ratio maximization can be mathematically expressed by

$$\begin{aligned} P_1: \quad & \max_{P_{m,n}} p_m \\ \text{s.t.} \quad & P_{\min} \leq P_{m,n} \leq P_{\max}, \\ & \forall m \in M, \forall n \in N, \end{aligned} \quad (5)$$

where P_{\max} denotes the maximum transmit power of each user, and P_{\min} denotes the minimum transmit power of each user.

The notations used in this paper are summarized in Table 1.

3 Proposed Solution

In this section, a distributed interference suppression method with low complexity and a small amount of multi-cell interaction is proposed to maximize the user supporting ratio of each cell. To reach the goal, the problem is defined as a non-cooperative game problem, and then a power interaction policy is proposed based on the power update formula obtained by the non-cooperative game.

▼Table 1. Summary of notations

Notation	Description
M	Number of BSs or cells
N	Number of users per cell
C	Total number of subcarriers
B	Total bandwidth
B_s	Bandwidth of per subcarrier
L	Number of subcarriers per user
$P_{m,n}$	Transmit power of the n -th user in the m -th cell
P_{\max}	Maximum transmit power of each user
P_{\min}	Minimum transmit power of each user
$R_{m,n}$	Achievable rate of the n -th user in the m -th cell
$R_{m,n}^{\text{th}}$	QoS threshold of the n -th user in the m -th cell
$\gamma_{m,n,l}$	SINR of the n -th user's l -th subcarrier in the m -th cell
$h_{m,n,l}$	Power gain of the n -th user's l -th subcarrier in the m -th cell
$h_{i,n,l}^m$	Power gain from n -th user's l -th subcarrier in the i -th co-frequency cell to m -th BS
$I_{m,n,l}$	Total interference received by the n -th user's l -th subcarrier in the m -th cell
N_0	Power spectral density of AWGN on the subcarrier
$\alpha_{i,n,l}$	A binary number
p_m	User supporting ratio of cell m

AWGN: additive white Gaussian noise

BS: base station

QoS: quality of service

SINR: signal to interference plus noise ratio

3.1 Formulation as Non-Cooperative Game

Let $G = \{P, A_m, U_m(\cdot)\}$ represent the power control game model of multi-cell non-cooperative game, where $P \in \{1, 2, \dots, M\}$ represents the set of users (i.e., participants) with co-frequency interference in each cell on the same subcarrier. That is, the cell index m is used to represent the user m within the cell. A_m represents the policy set of user m , $A_m = \{P_m | P_{\min} \leq P_m \leq P_{\max}\}$, and $U_m(\cdot)$ denotes the utility function for user m . Each user maximizes its utility value by adjusting the power. In order to achieve the goal, there may be malicious competition. Therefore, it is necessary to ensure that the system can obtain a steady-state solution, that is, the Nash equilibrium solution.

According to Ref. [20], the utility function based on the non-cooperative game model is defined as

$$U_m(P) = a_m \sqrt{\gamma_m - \gamma_m^{\text{th}}} - c_m P_m, \quad (6)$$

where γ_m^{th} is the SINR threshold of user m on a subcarrier. In Eq. (6), the first term considers the minimum SINR requirement of the user, and the second term represents the interference caused by the user to other users. Besides, a_m and c_m are system parameters.

3.2 Nash Equilibrium Solution

The second term of the utility function can be understood as the price paid by each user to improve SINR. In other words, users are not only restricted by power. In order to ob-

tain the optimal solution, first of all, for convenience we have the following equation:

$$I_m = I_{m,n,l} + N_0. \quad (7)$$

Then, the gradient of the utility function $U_m(P)$ is calculated according to Eqs. (6) and (7), and we have

$$\frac{\partial U_m}{\partial P_m} = \frac{1}{2} a_m (\gamma_m - \gamma_m^{\text{th}})^{-\frac{1}{2}} \frac{h_m}{I_m} - c_m. \quad (8)$$

Let $\frac{\partial U_m}{\partial P_m} = 0$, we have

$$\gamma_m = \gamma_m^{\text{th}} + \left(\frac{a_m h_m}{2 c_m I_m} \right)^2. \quad (9)$$

According to Eq. (1), we can obtain that

$$P_m = \frac{I_m}{h_m} \gamma_m^{\text{th}} + \beta_m \frac{h_m}{I_m}, \quad (10)$$

where $\beta_m = \left(\frac{a_m}{2 c_m} \right)^2$.

According to Newton's iterative formula, we can obtain the following optimal power iterative formula:

$$P_m(k+1) = \frac{P_m(k)}{\gamma_m(k)} \gamma_m^{\text{th}} + \beta_m \frac{\gamma_m(k)}{P_m(k)}, \quad (11)$$

where k denotes the iterative number. According to Ref. [20], $\forall P \geq P'$, and then $I_m \geq I'_m$. When $I'_m \geq \sqrt{\beta_m \gamma_m^{\text{th}}}$, the iterative expression Eq. (11) converges to a unique point.

3.3 Distributed Power Control Method

According to Eq. (11), the power of user n in cell m is calculated, denoted as $P_{m,n}^{\text{game}}$, namely, predictive power. BS in each cell calculates a ratio $r_{m,n}$ for each user, with $r_{m,n} > 0$ as follows.

$$r_{m,n} = \frac{R_{m,n}}{R_{m,n}^{\text{th}}}, \quad \forall m, n. \quad (12)$$

The predicted power of users interacts between BSs. That is, the BS in cell m transmits a power $P_{m,n}^{\text{game}}$ to all BSs in other neighboring cells. The predicted power received by user n in cell m is stored in set S_p .

We define F as a binary variable. If half of the predicted power in set S_p is increased compared with the last time, $F = 1$; otherwise, $F = 0$. Then the current power of user n in cell m is set as follows,

Case 1: When $0 < r_{m,n} < v_1$, then $P_{m,n} = P_{\min}$;

Case 2: When $v_1 \leq r_{m,n} < v_2$ and $F = 1$, then $P_{m,n} = \min \{P_{m,n}^{\text{game}}, P'_{m,n}\}$, where $P'_{m,n} = P_{m,n} - (P_{m,n} - P_{\min}) \cdot (1 - r_{m,n})$. Moreover, when $v_1 \leq r_{m,n} < v_2$ and $F = 0$, then $P_{m,n} = P_{m,n}^{\text{game}}$;

Case 3: When $v_2 \leq r_{m,n} < 1$, then $P_{m,n} = \min \{P_{\min}, P'_{m,n}\}$, where $P'_{m,n} = P_{m,n} + (P_{\max} - P_{m,n}) \cdot (1 - r_{m,n})$; where v_1 and v_2 is two constants, and $0 < v_1 < v_2 < 1$.

The problem of maximizing the number of users meeting the QoS threshold is actually non-convex, and the solution is very complicated, which means that it is difficult to converge to the global optimal solution. Therefore, the condition for ending the algorithm is set to converge or reach the maximum scheduling times.

4 Simulation Results

In this section, some simulation results are presented to verify the performance of our proposed scheduling scheme. The network scenario shown in Fig. 2 is simulated, where the number of cells/BSs is 7. The radius of each cell is $R = 570$ m, and the distance between the BSs is $D = 950$ m. For multi-cell OFDM systems, there is no intra-cell interference within each cell but the inter-cell interference cannot be neglected since different users from different cells may transmit signals over the same frequency band^[22-23]. The more cell-edge users, the stronger the inter-cell interference. To explore the system power control scheme in severe inter-cell interference scenarios, in this paper, most users are densely distributed at the edge of each cell in the simulations. It is assumed that the edge area of the cell is from 380 to 570 m. Each cell has 190 users randomly and evenly distributed in the edge area and 10 users randomly and evenly distributed in the central area¹. According to Ref. [21], the channel power gain is given by

$$h_{m,n,i} = -(-55.9 + 38 \cdot \log_{10}(d_{m,n,i}) + (24.5 + 1.5 \cdot fc/925) \cdot \log_{10}(fc)), \quad (13)$$

where $d_{m,n,i}$ denotes the distance between the n -th user in the m -th cell and the base station in the i -th cell, and fc is the center frequency point and is set as $fc = 2\,300$ MHz.

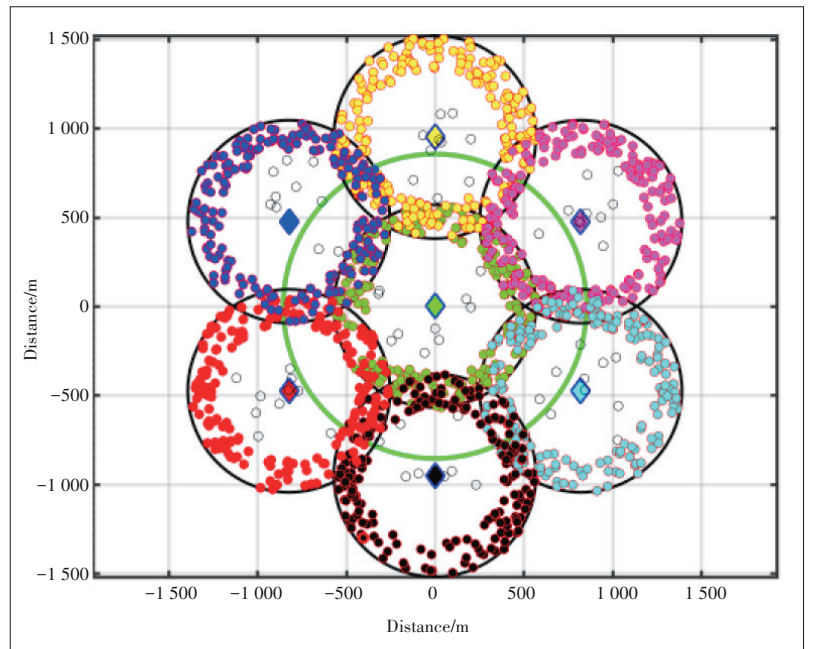
The initial power of each user is 17 dBm. The total bandwidth of the system is 10 MHz, and the total number of subcarriers is 1 600. The bandwidth of a subcarrier is $B = 1/160$ MHz, and the number of carriers allocated to each user is $L = 8$. The noise power is $N_0 = -174$ dBm/Hz,

and the maximum and minimum transmit power of the user is $P_{\max} = 23$ dBm and $P_{\min} = 14$ dBm. For the m -th cell, we define $r_m = (r_{m,1}, r_{m,2}, \dots, r_{m,N})$. r_m is sorted in ascending order and then r'_m is obtained, where $r'_m = (r'_{m,1}, r'_{m,2}, \dots, r'_{m,N})$. v_1 is set as $r'_{m,80}$ and v_2 is set as $r'_{m,140}$. That is, the rate for 40% of users is less than v_1 and 70% of users is less than v_2 . The SINR threshold and the QoS threshold of each user are determined by the distance from the user to the BS and the initial power.

In this paper, it is assumed that if a cell user works on the same frequency band as the neighbor cell user and the distance between the neighbor cell user and the BS of the current cell is less than $1.5R$, it causes interference to the user of the current cell. In addition, since the central user is relatively far from the BS of the other cell, it is assumed that there is no interference from the central user.

The user supporting ratio of cell m after using our presented policy is referred to as cell m -After, with $m \in \{1, 2, \dots, M\}$. In order to verify the effectiveness of the proposed policy, the user supporting ratio of cell m without using our presented policy (called cell m -Before) is simulated as the benchmark method, with $m \in \{1, 2, \dots, M\}$.

Fig. 3 depicts the user supporting ratio of each cell versus scheduling times under a non-cooperative game scheme. It can be observed that the user supporting ratio of each cell gradually increases with the scheduling times and finally



▲ Figure 2. Simulation scene

1. When the numbers of users in the cells are different, the proposed algorithm can still work well, because the three cases in Section 3.3 can increase the number of users meeting the QoS requirement on each carrier, which means that the total number of users meeting the QoS requirement will also increase. When the numbers of users in the cells are different, inter-cell interference received on the same frequency band may change, because the values of v_1 and v_2 are adaptive and can be adjusted according to specific interference situations, the algorithm is still valid. Without loss of generality, the numbers of users in all cells are assumed to be the same in simulations.

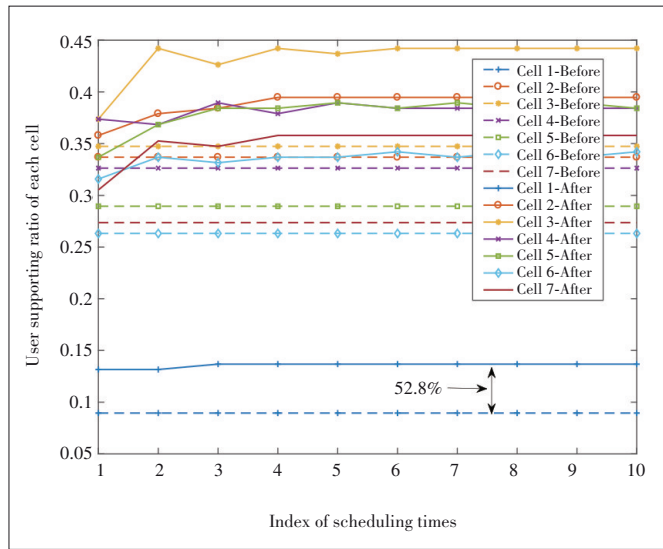
tends to be flat. Taking the first cell as an example, compared with no scheduling policy, the user supporting ratio of the cell increases by 52.8%.

Fig. 4 plots the user supporting ratio of each cell versus scheduling times under an interactive scheme based on non-cooperative game. It can be observed that the user supporting ratio of each cell gradually increases with the scheduling times and finally tends to be flat. Taking the first cell as an example, the user supporting ratio of the cell is improved by 82.8% compared with the situation when no policy is used. In addition, the interaction scheme is improved by 30% compared with the non-interaction scheme. This is because when an interactive policy is adopted, some interfering users may choose to reduce transmit power, so that other interfer-

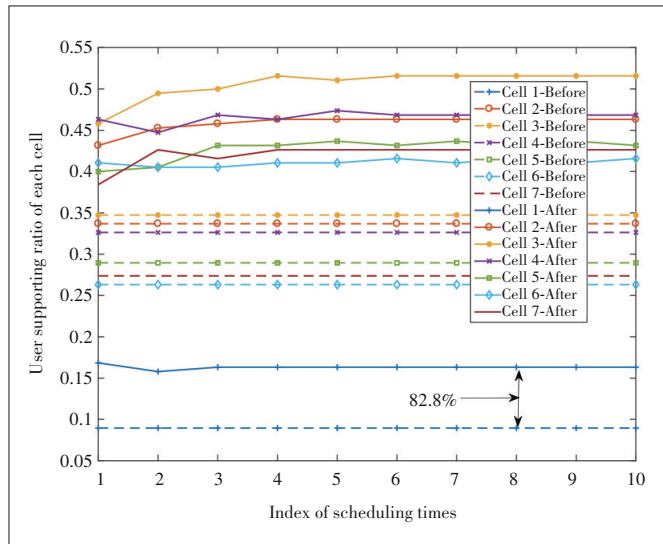
ing users may increase the communication rate.

Fig. 5 shows the average user supporting ratio of all cells versus scheduling times under the non-cooperative game scheme. One can see that the average user supporting ratio of all cells gradually increases with scheduling times and finally tends to be flat. The results with the non-cooperative game scheduling method are improved by 26.7% compared with those without the scheduling policy.

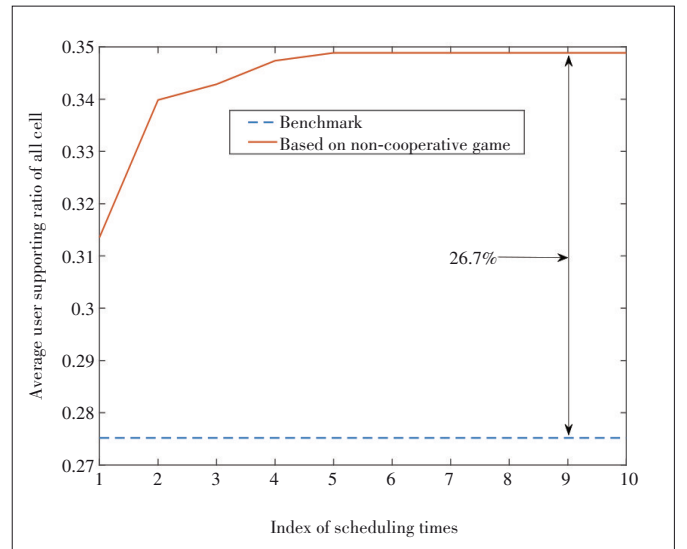
Fig. 6 shows the average user supporting ratio of all cells versus scheduling times under the interactive scheme based on the non-cooperative game. The average user supporting ratio under the proposed scheduling method based on non-cooperative game interaction is improved by 49.7% compared with the results without the scheduling policy. Be-



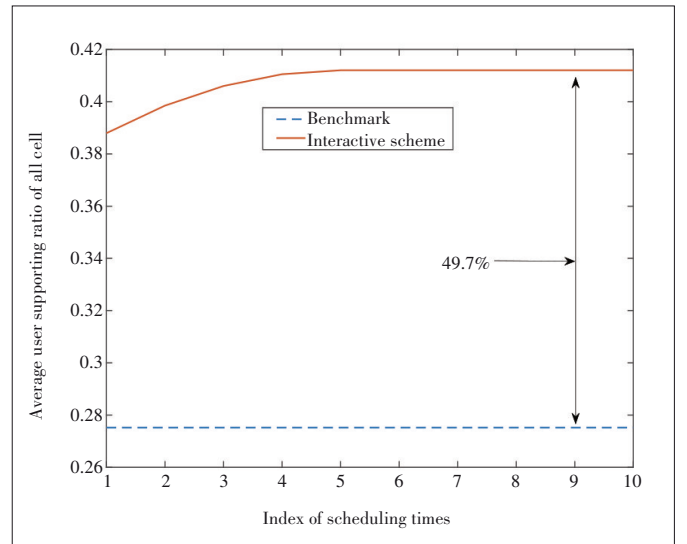
▲ Figure 3. User supporting ratio of each cell under an interactive scheme based on non-cooperative game



▲ Figure 4. User supporting ratio of each cell under an interactive scheme based on non-cooperative game



▲ Figure 5. Average user supporting ratio of all cells under the non-cooperative game scheme



▲ Figure 6. Average user supporting ratio of all cells under the interactive scheme based on the non-cooperative game

sides, the interaction scheme is improved by 23% compared with the non-interaction scheme.

5 Conclusions

A distributed power control method with low complexity and a small amount of multi-cell interaction is presented in this paper. Different from the traditional work, our goal is to improve the user supporting ratio of each cell. For this purpose, first, a non-cooperative power control scheme is proposed, and then, an interactive power control scheme based on non-cooperative games is proposed. The simulation results show that our proposed scheme achieves a notable performance gain compared with the traditional method without inter-cell interaction.

References

- [1] KAMEL M, HAMOUDA W, YOUSSEF A. Ultra-dense networks: A survey [J]. *IEEE communications surveys & tutorials*, 2016, 18(4): 2522 – 2545. DOI: 10.1109/COMST.2016.2571730
- [2] CHEN W, BAO Y Y. Key technologies of internet-of-intelligent-things towards 6G [J]. *ZTE technology journal*, 2021, 27(2): 6 – 12
- [3] GE X H, YANG B, YE J L, et al. Spatial spectrum and energy efficiency of random cellular networks [J]. *IEEE transactions on communications*, 2015, 63(3): 1019 – 1030. DOI: 10.1109/tcomm.2015.2394386
- [4] LAN M. Part 16: Air interface for fixed and mobile broadband wireless access systems amendment for physical and medium access control layers for combined fixed and mobile operation in licensed bands: IEEE 802.16e-2005 [S]. 2006
- [5] HOU S W, KO C C. Inter-carrier interference suppression for OFDMA uplink in time- and frequency-selective fading channels [J]. *IEEE transactions on vehicular technology*, 2009, 58(6): 2741 – 2754. DOI: 10.1109/TVT.2008.2010550
- [6] MORELLI M. Timing and frequency synchronization for the uplink of an OFDMA system [J]. *IEEE transactions on communications*, 2004, 52(2): 296 – 306. DOI: 10.1109/TCOMM.2003.822699
- [7] CAO Z R, TURELI U, YAO Y D. Deterministic multiuser carrier-frequency offset estimation for interleaved OFDMA uplink [J]. *IEEE transactions on communications*, 2004, 52(9): 1585 – 1594. DOI: 10.1109/TCOMM.2004.833183
- [8] KWON H, LEE B G. Distributed resource allocation through non-cooperative game approach in multi-cell OFDMA systems [C]//*Proceedings of 2006 IEEE International Conference on Communications*. IEEE, 2006: 4345 – 4350. DOI: 10.1109/ICC.2006.255764
- [9] GUO Y C, HU C J, PENG T, et al. Regression-based uplink interference identification and SINR prediction for 5g ultra-dense network [C]//*ICC 2020 IEEE International Conference on Communications*. IEEE, 2020: 7 -11
- [10] SUN Y, CHANG Y Y, WANG C, et al. Research on interference cancellation for switched-on small cells in ultra-dense network [J]. *ZTE communications*, 2016(B12): 48 – 53
- [11] AL-ZAHRANI A Y, YU F R, HUANG M Y. A distributed interference control scheme in large cellular networks using mean-field game theory [C]//*Proceedings of 2013 IEEE 24th Annual International Symposium on Personal, Indoor, and Mobile Radio Communications*. IEEE, 2013: 3339 – 3343. DOI: 10.1109/PIMRC.2013.6666724
- [12] ZHANG T K, FENG C Y, SU G, et al. Uplink multi-cell non-cooperative power allocation game algorithm for OFDMA cellular networks [C]//*Wireless Communications, Networking and Mobile Computing*. IEEE, 2009: 1 – 4
- [13] JING Q, ZHENG Z. Distributed resource allocation based on game theory in multi-cell OFDMA systems [J]. *International journal of wireless information networks*, 2009, 16(1/2): 44 – 50. DOI: 10.1007/s10776-009-0088-y
- [14] DEB S, MONOIOUDIS P. Learning-based uplink interference management in 4G LTE cellular systems [J]. *IEEE/ACM transactions on networking*, 2015, 23(2): 398 – 411. DOI: 10.1109/TNET.2014.2300448
- [15] JO H S, MUN C, MOON J, et al. Interference mitigation using uplink power control for two-tier femtocell networks [J]. *IEEE transactions on wireless communications*, 2009, 8(10): 4906 – 4910. DOI: 10.1109/TWC.2009.080457
- [16] CHOI I, LEE C. A scaled hard interference cancellation scheme in an uplink multi-cell environment [J]. *IEEE transactions on vehicular technology*, 2015, 64(12): 5741 – 5749. DOI: 10.1109/TVT.2014.2386864
- [17] KIM W, KALEEM Z, CHANG K. UE-specific interference-aware open-loop power control in 3GPP LTE-A uplink HetNet [C]//*Proceedings of 2015 Seventh International Conference on Ubiquitous and Future Networks*. IEEE, 2015: 682 – 684. DOI: 10.1109/ICUFN.2015.7182630
- [18] XU J, NIU H T, ZHAO T J, et al. Robust optimal power control and subcarrier allocation in uplink OFDMA network with assistance of mobile relay [J]. *IEEE access*, 2021, 9: 57475 – 57485. DOI: 10.1109/ACCESS.2021.3072981
- [19] GE X H, HUANG K, WANG C X, et al. Capacity analysis of a multi-cell multi-antenna cooperative cellular network with co-channel interference [J]. *IEEE transactions on wireless communications*, 2011, 10(10): 3298 – 3309. DOI: 10.1109/TWC.2011.11.101551
- [20] ZHANG T K, ZENG Z M, QIU Y. Distributed uplink power control algorithm for multi-cell OFDM systems [J]. *Journal of Beijing University of Technology*, 2008: 34(6): 561 – 566
- [21] GOLDSMITH A. *Wireless Communications* [M]. Cambridge, UK: Cambridge University Press, 2005. DOI: 10.1017/cbo9780511841224
- [22] LEI H P, ZHANG L, ZHANG X, et al. A novel multi-cell OFDMA system structure using fractional frequency reuse [C]//*Proceedings of 2007 IEEE 18th International Symposium on Personal, Indoor and Mobile Radio Communications*. IEEE, 2007: 1 – 5. DOI: 10.1109/PIMRC.2007.4394228
- [23] NOVLAN T, ANDREWS J G, SOHN I, et al. Comparison of fractional frequency reuse approaches in the OFDMA cellular downlink [C]//*Proceedings of 2010 IEEE Global Telecommunications Conference GLOBECOM 2010*. IEEE, 2010: 1 – 5. DOI: 10.1109/GLOCOM.2010.5683973

Biographies

HU Huimin received her B.S. degree from the School of Electronic and Information Engineering, Lanzhou Jiaotong University, China in 2017. She is currently pursuing the Ph.D. degree with the School of Computer and Information Technology, Beijing Jiaotong University, China. Her current research interests include age of information, energy harvesting in wireless communication networks, and wireless sensor networks.

LIU Yuan received her B.S. degree from the College of Computer and Information Technology, Liaoning Normal University, China in 2017. She is currently pursuing the Ph.D. degree with the School of Computer and Information Technology, Beijing Jiaotong University, China. Her current research interests include UAV communications, energy harvesting in wireless communication networks, and wireless sensor networks.

GE Yiyang received his B.S. degree from the School of Computer and Information Technology, Beijing Jiaotong University, China in 2019. He is cur-

rently pursuing the Ph.D. degree with the School of Computer and Information Technology, Beijing Jiaotong University. His current research interests include age of information, energy harvesting in wireless communication networks, and wireless sensor networks.

WEI Ning received his B.S. and M.S. degrees respectively in 2012 and 2015 from Shandong University, China. Currently, he is an R&D engineer in ZTE Corporation. His research interests include massive MIMO network, compressed sensing, optimization theory and machine learning.

XIONG Ke (kxiong@bjtu.edu.cn) received his B.S. and Ph.D. degrees from

Beijing Jiaotong University (BJTU), China in 2004 and 2010, respectively. From April 2010 to February 2013, he was a postdoctoral research fellow with the Department of Electronics Engineering, Tsinghua University, China. Since March 2013, he has been a lecturer and an associate professor of BJTU, where he is currently a full professor and the Vice Dean of the School of Computer and Information Technology. From September 2015 to September 2016, he was a visiting scholar with the University of Maryland, USA. He has published more than 100 academic papers in referred journals and conferences. His current research interests include wireless cooperative networks, wireless powered networks, and network information theory. He is a member of China Computer Federation (CCF) and also a senior member of the Chinese Institute of Electronics (CIE). He serves as the associate editor-in chief for the *Chinese Journal New Industrialization Strategy*, and an editor of *Computer Engineering and Software*.



SVM for Constellation Shaped 8QAM PON System

Abstract: Nonlinearity impairments and distortions have been bothering the bandwidth constrained passive optical network (PON) system for a long time and limiting the development of capacity in the PON system. Unlike other works concentrating on the exploration of the complex equalization algorithm, we investigate the potential of constellation shaping joint support vector machine (SVM) classification scheme. At the transmitter side, the 8 quadrature amplitude modulation (8QAM) constellation is shaped into three designs to mitigate the influence of noise and distortions in the PON channel. On the receiver side, simple multi-class linear SVM classifiers are utilized to replace complex equalization methods. Simulation results show that with the bandwidth of 25 GHz and overall bitrate of 50 Gbit/s, at 10 dBm input optical power of a 20 km standard single mode fiber (SSMF), and under a hard-decision forward error correction (FEC) threshold, transmission can be realized by employing Circular (4, 4) shaped 8QAM joint SVM classifier at the maximal power budget of 37.5 dB.

Keywords: passive optical networks; support vector machine; geometrically shaping; constellation classification; digital signal processing

LI Zhongya^{1,3}, CHEN Rui^{2,3},
HUANG Xingang², ZHANG Junwen^{1,3},
NIU Wenqing^{1,3}, LU Qiuyi^{1,3}, CHI Nan¹

(1. Key Laboratory for Information Science of Electromagnetic Waves, Fudan University, Shanghai 200433, China;
2. ZTE Corporation, Shenzhen 518057, China;
3. Department of Communication Science and Engineering, School of Information Science and Technology, Fudan University, Shanghai 200433, China)

DOI: 10.12142/ZTECOM.2022S1009

<http://kns.cnki.net/kcms/detail/34.1294.TN.20211122.1958.001.html>, published online November 23, 2021

Manuscript received: 2021-07-25

Citation (IEEE Format): Z. Y. Li, R. Chen, X. G. Huang, et al., "SVM for constellation shaped 8QAM PON system," *ZTE Communications*, vol. 20, no. S1, pp. 64 – 71, Jan. 2022. doi: 10.12142/ZTECOM.2022S1009.

1 Introduction

The newly emerged application scenarios of access networks such as high-definition video streaming services, virtual reality and cloud computing are all driving capacity upgradation for next-generation (NG) passive optical networks (PONs), which is highly recognized for their low cost and flexible advantages. In the meantime, organizations like IEEE 802.3ca and ITU-T are working on the standardization of their 50 Gbit/s/λ⁻¹ PON^[1], and feasible 100 Gbit/s solutions are under investigation^[2-3]. Low-cost intensity modulation and direct detection (IM/DD) transmission schemes have been demonstrated using 10 Gbit/s transmitters^[3-5]. To achieve high-speed PONs with bandwidth limited optics components, advanced modulation formats and effective digital signal processing (DSP) are the central research topics^[6]. Electrical/optical duo-binary^[3], pulse amplitude modulation (PAM)^[7], and carrierless amplitude and phase (CAP) modulation^[8] have been widely investigated for a potential low-cost solution for medium- and long reach-

PON systems. Related works suggest that compared with non-return zero (NRZ), PAM, or orthogonal frequency division multiplexing (OFDM), the IM/DD based CAP modulation scheme has great potential in the optical transmission system for its advantages of low power consumption, high spectrum efficiency, and low cost^[9]. But limited works have been devoted to researching the applicability of CAP modulation in the PON system. In this work, we transmit single band CAP modulated 8QAM signals in the PON system and provide the performance analysis.

In fiber-optic communication systems, higher-order QAM modulation leads to higher spectral efficiency, but at the same time, inter-symbol interference (ISI) increases, which demands higher signal-to-noise ratios (SNRs) to ensure reliable system transmission. However, for legacy optics based high capacity PON systems, the bandwidth limitation and fiber dispersion would induce severe distortion to signals and lead to lower SNR. To overcome impairments, several DSP methods are introduced including feed forward equalization (FFE), decision feed-back equalization (DFE)^[10], Volterra (VOT) nonlinear equalization, least-mean-square (LMS) equalization^[6], and digital pre-equalization. Such schemes bring great costs on computational complexity and are impractical in real deploy-

This work was partially supported by the NSFC project (No. 61925104, No. 62031011), and by ZTE Industry-Academia-Research Cooperation Funds under Grant No. HC-CN-20191231006.

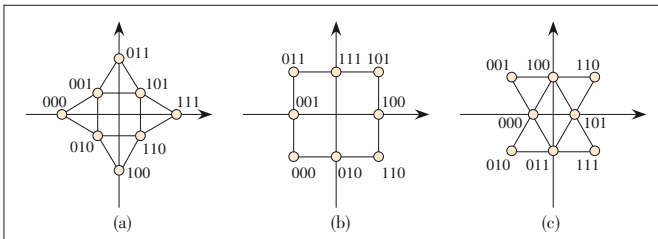
ments. In Refs. [11 – 12] support vector machines (SVMs) are used for QAM classification, which is an unusual way to mitigate signal distortions. Moreover, a geometrically shaping technology is applied to QAM signals in Ref. [12] to further improve its resistance to noise. However, the related research is carried out in a 50 m fiber and visible light system, of which channel characteristics, such as the bandwidth, dispersion, attenuation, and origins of nonlinearity, are quite different from the PON systems. The idea of separating computational pressures onto transmitter and receiver sides is novel but needs to be assessed and optimized in the cost-sensitive PON system. Thus, it is still a challenge to develop a reliable and low-cost solution to dealing with the linear and nonlinear distortions in the bandwidth limited high speed PON system.

To cope with this problem, we adopt a cheap scheme employing the constellation shaping technique and the linear SVM. In the data coding phase, constellations are shaped to decrease possible noise and inter-symbol interference (ISI), which shares the equalization pressure at the receiver side. And we choose three kinds of shaped 8QAM constellations to evaluate their performances in the PON system. On the receiver side, we propose to utilize an SVM for signal recovering after a simple LMS equalization. The signal recovering process is converted to a classification problem of the constellation points and SVM can precisely generate decision boundary though the nonlinear distortion of the constellation is serious. Simulation results indicate that at the bandwidth of 25 GHz and an overall bitrate of 50 Gbit/s, system performance can be significantly improved by the proposed constellation shaping joint SVM scheme. Over 37 dB link loss budget is achieved.

2 Principle

2.1 SVM for Modified 8QAM Constellation

By redesigning the distribution of the transmitted signal constellation, geometrically shaping (GS) can improve the minimum Euclidean distance (ED) between constellation points representing different QAM symbols, thus reducing the effects of noise. In this section, we evaluate three special-shaped 8QAM constellations among the GS-8QAM signals. Fig. 1 shows the redesigned constellations. The most commonly used is Circular (4, 4) which divides 8 constellation points into 4 points in the outer ring and 4 points in the inner ring; in addition,



▲ Figure 1. Constellations of shaped 8 quadrature amplitude modulation (8QAM): (a) Circular (4, 4), (b) rectangular and (c) triangular

we also discuss the rectangular distribution and triangular distribution.

The ratio of the radius of the outer ring to the radius of the inner ring (second outer) is 1.932, 1.414 and 1.414 for Circular (4, 4), Rectangular and Triangular respectively, which refers to the amplitude difference between the symbol points in the three constellations. Apparently, the high amplitude signal induces severer nonlinear impairments to low amplitude signals. Therefore, distortion and compression appear in the constellation points near the outer ring, which destroys the original separable margin and changes the ED between different symbols. This phenomenon is harmful to the ED based signal detection method. We consider the 8QAM constellation set as \mathcal{M} and one received symbol as y_{ij} , and then the ED based signal detection result of y_{ij} can be obtained as:

$$\tilde{x}_{ij} = \arg \min_{x \in \mathcal{M}} |y_{ij} - x|. \quad (1)$$

Once the position of y_{ij} deviates a considerable distance from the correct x due to the nonlinear distortion and compression, the detection result of Eq. (1) will go wrong in high probability. However, by searching suitable received symbols in different groups as the support vectors, SVM can effectively find the optimal decision boundaries during groups without the restriction of constellation set \mathcal{M} . In the binary classification case, two groups are supposed to be separable if there exists one function which can be expressed as:

$$f(x) = w^T x + b, \quad (2)$$

where w and b denote the weight and bias. Given the training data x_i , and $y_i \in \{\pm 1\}$ is the associated label, the function should satisfy that $f(x) > 0$, if $y_i = 1$; $f(x) < 0$, if $y_i = -1$. $f(x) = 0$ acting as a decision boundary toward two regions is called a hyperplane. Those points satisfying $f(x) = \pm 1$ are called support vectors and the distance between $f(x) = \pm 1$ is called margin which equals to $2/\|w\|$. The goal of SVM is to find the optimal support vector such that the margin is maximized. In other words, this is an optimization problem.

$$\begin{aligned} & \underset{\{w, b\}}{\text{minimize}} \quad \frac{1}{2} \|w\|^2 \\ & \text{subject to} \quad y_i (w^T x_i + b) \geq 1, \text{ with } i = 1, 2, \dots, n \end{aligned} \quad (3)$$

For those cases that the data cannot support perfectly linear separating, slack variable $\xi_i > 0$ is introduced:

$$\begin{aligned} & \underset{\{w, b\}}{\text{minimize}} \quad \frac{1}{2} \|w\|^2 + C \sum_{i=1}^n \xi_i \\ & \text{subject to} \quad y_i (w^T x_i + b) \geq 1 - \xi_i \\ & \quad \xi_i \geq 0, i = 1, 2, \dots, n \end{aligned} \quad (4)$$

If the training data set is assumed to be linearly inseparable,

ble, the kernel function can be used to map the origin input vectors into a linearly separable space. In this paper, shaped 8QAM constellation classifications are treated as linear separable problems. Therefore, the detailed derivation for SVM classifiers using kernel function is not discussed here and can be found in Refs. [13 – 14].

Detection of the shaped 8QAM constellation is an eight-class classification problem. However, we can build a binary SVM classifier between each one class and the rest seven classes, so the results of eight binary SVM classifiers can solve the eight-class classification problem^[15–16]. This problem can be trained in many efficient ways^[17–18]. After training, the workflow of an SVM classifier is shown in Fig. 2(a). At first, the input feature vector is normalized by a linear kernel function. Then the normalized feature that joints a few support vectors is fed into the $\text{sign}(\bullet)$ function for decision. Finally, the decision output vector is decoded to get the final classification result.

In fact, the training process of SVM is to find the optimal support vectors which decide ω and the hyperplane. So, when the shaped 8QAM constellation suffers from distortions and compression after the transmission in the PON channel, the position changes of the support vectors will rearrange the hyperplane. Figs. 2(a) and 2(b) show the influence of nonlinearity on the constellation points and the hyperplanes. In Figs. 2(a) and 2(b), the blue ball denotes the constellation points of the outer ring and the red ball denotes the constellation points of the inner ring. Owing to the nonlinear response of the channel, the outer ring will be compressed more severely than the inner ring, which results in the approaching of the blue ball and the red ball. And then from Fig. 2(a) to Fig. 2(b), the support vectors picked from the colored balls

will direct the hyperplanes to new positions, while the ED decision method still holds its eight decision areas on the three kinds of shaped 8QAM constellations. Points in the compressed 8-QAM constellation are easy to fall on the wrong ED decision areas due to annoying noise but the SVM can figure out the compression and reflect on the changes of decision boundaries. As a result, the SVM classifier appears more stable and accurate than the ED decision method.

2.2 Adaptive Volterra Filter

Volterra filters are commonly used to model nonlinear responses and compensate for nonlinear effects in IM/DD systems^[17]. An n -th order Volterra filter can be expressed as:

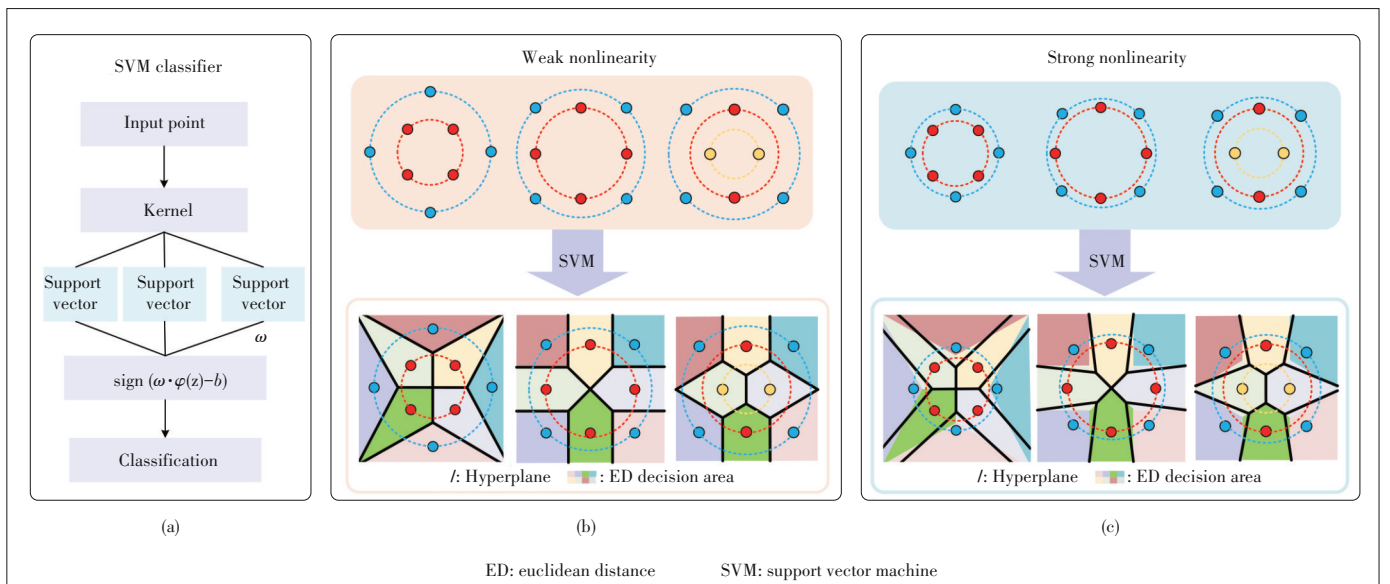
$$y(n) = \sum_{n=1}^N \left[\sum_{k_1=0}^{M-1} \dots \sum_{k_n=k_{n-1}}^{M-1} a_n(k_1, \dots, k_n) x(n - k_1) \dots x(n - k_n) \right], \quad (5)$$

where M represents the memory length and a_n is the n -th order Volterra kernels.

The coefficients of the second-order Volterra filter can be searched by using the LMS adaptive structure in Ref. [18], and the algorithm is described as

$$\begin{aligned} \mathbf{a}_1(k+1) &= \mathbf{a}_1(k) + \mu \mathbf{e}_k \\ [\mathbf{a}_2(k+1)] &= [\mathbf{a}_2(k)] + \mu \mathbf{e}_k \mathbf{x} \mathbf{x}^T \\ \mathbf{e}_k &= \mathbf{d}_k - \mathbf{y}_k, \end{aligned} \quad (6)$$

where μ controls the magnitude of the weight adjustment, \mathbf{x} is the $M \times 1$ input vector, $[\mathbf{a}_2]$ is a coefficients matrix containing the second-order kernel factors, and \mathbf{e}_k represents the error. In



▲ Figure 2. (a) Flow chart of SVM classifier, (b) nonlinear distortions of the three constellations and (c) their influences on hyperplanes of the SVM classifier

this work, the second-order LMS-based Volterra filter (LMS-VOT) is implemented to equalize distortions in the received signal and compare the performance with the SVM based scheme.

3 Simulation Setup

The PON system simulation is carried out in the VPItransmissionMaker™. In the simulation setup shown in Fig. 3(a), bandwidth limitations, dispersion, and nonlinearity of the fiber link are considered. At the transmitter (Tx) side, to simulate a bandwidth-constrained system, the electrical signal generated from Tx DSP is passed through a 25 GHz low-pass fourth-order Bessel filter before being input into the electro-absorption modulator (EAM). On the other branch, the laser generates a 228.33 THz continuous wave (CW) and also inputs it into the EAM. The transmission characteristic of EAM is determined by the manual defined nonlinear transfer curve in Fig. 3(b). From the curve we can find as the input voltage increases, the modulated output of EAM suffers from saturation influence and severe nonlinear distortions occur. Then the modulated optical signal is fed into a bandpass optical filter to generate a single sideband (SSB) signal. This operation can reduce the power decay caused by dispersion. For flexible control of the transmit power, the output signal from the filter is passed through an optical amplifier. And then the signal is transmitted to the optical distribution network (ODN) through a 20 km

long standard single mode fiber (SSMF) with an attenuation of 0.32E-3 dB/m. The output signal of the fiber is connected to two 1×8 splitters to simulate the multi-user network. And the followed attenuator (ATT) controls the link loss, together with the budget for other losses in the link, resulting in a total attenuation of 32 dB from the Tx to the receiver side (Rx). The current signal from the avalanche photodiode (APD) is converted into the voltage signal by a transimpedance amplifier (TIA). Afterward, the voltage signal is analyzed by off-line Rx DSP. Except for the above-mentioned parameters, the rest simulation parameters are summarized in Table 1.

In the Tx DSP, constellation shaped 8QAM symbols are generated and then oversampled to 4 samples per symbol. The orthogonal square-root-raised cosine (SRRC) shaping filter

▼ Table 1. Simulation parameters

Parameter	Value	Parameter	Value
Data rate	50 Gbit/s	Dispersion slope of SSMF	0.086E3 s/m ³
Signal format	shaped 8QAM CAP	Nonlinear index of SSMF	2.6E-20 m ² /W
Sample rate	200/3 GHz	Responsivity of APD	0.8 A/W
Filter type	Fourth-order Bessel	Dark current multiplied of APD	300E-9 A
Tx signal wavelength	1 310 nm	Avalanche multiplication of APD	8
Length of SSMF	20 km	Ionization coefficient of APD	0.4
Attenuation of SSMF	0.32E-3 dB/m	Transimpedance of TIA	1 000 Ω
Dispersion of SSMF	0.35E-5 s/m ²	Input equivalent noise of TIA	1.1E-6 A

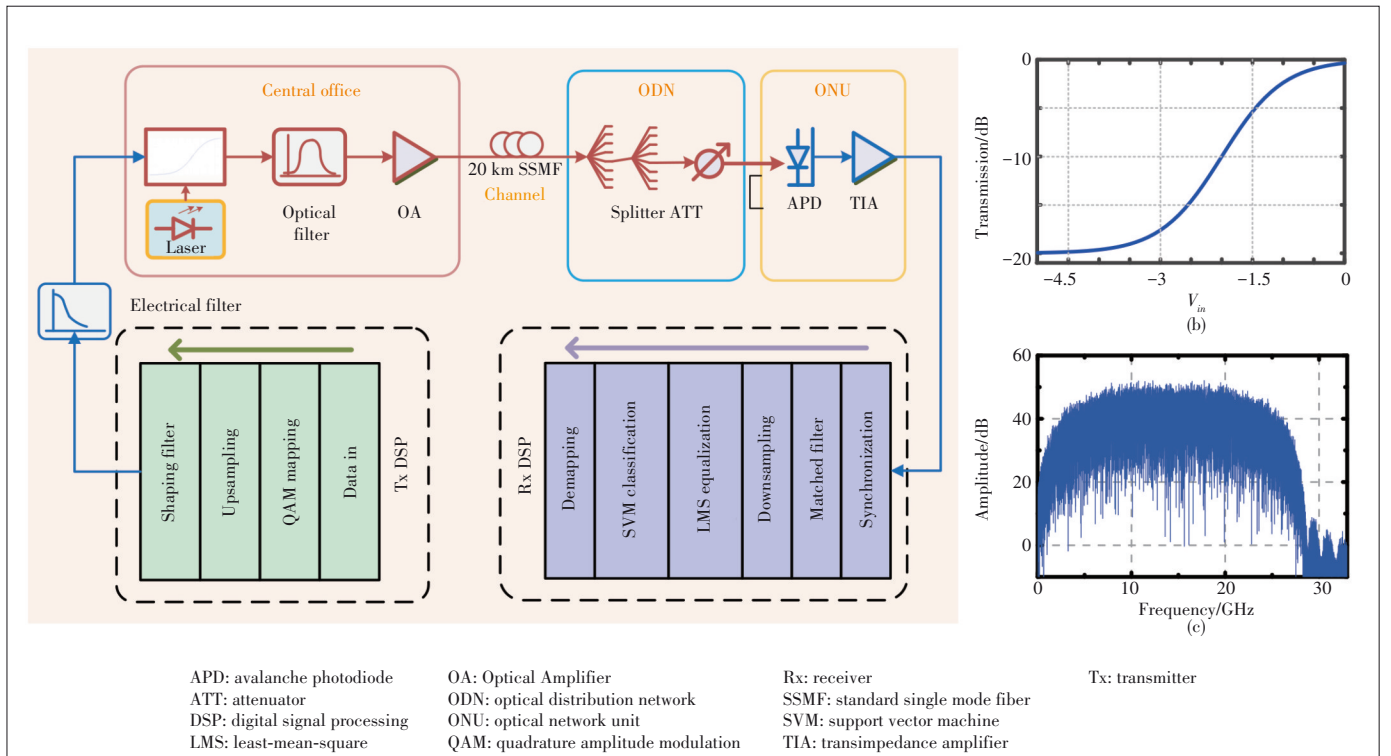
APD: avalanche photodiode

TIA: transimpedance amplifier

CAP: carrierless amplitude and phase

Tx: transmitter

SSMF: standard single mode fiber



▲ Figure 3. (a) Simulation setup of constellation shaped 8QAM PON system, (b) spectrum of the transmitted signal and (c) electro-absorption modulator (EAM) transmission characteristic

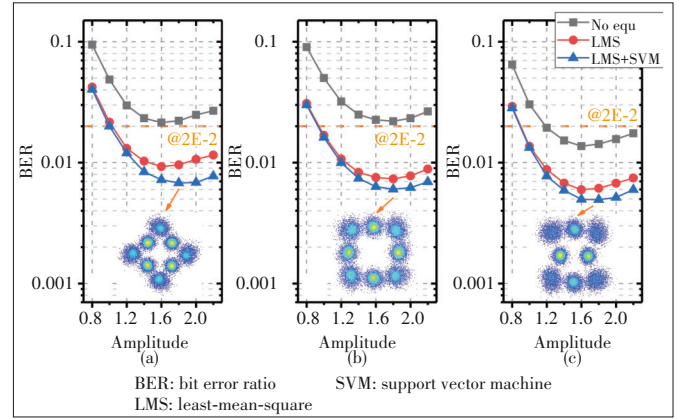
pairs containing I/Q channels with a variable roll-off are applied to get the carrierless amplitude and phase (CAP) modulated signal. Fig. 3(c) shows the electric spectrum of the modulated Tx signal. The Rx DSP consists of a synchronization module, matched SRRC filter pairs to extract the in-band signal, a down-sampler that generates one symbol for every four samples, a simple LMS equalizer, a multi-class SVM classifier, and a QAM decoder to convert the SVM output symbols into bitstreams for calculating the bit error ratio (BER) of the recovered signal.

Before launching the performance evaluation, the optimal operating state of the Tx signal is investigated by measuring the BER of Circular (4, 4) based 8QAM PON system under different roll-off of the shaping filter, bias of the laser, and linewidth of the laser. From results shown in Figs. 4(a) and 4(d), as the roll-off and bias increase, we can see the BER reaches the minimum and then rises. The maximal BER difference between LMS and LMS+SVM is 5.4×10^{-3} in Fig. 4(d). Similar results also can be observed in Fig. 4(b), where the trend suggests that the PON channel generates different degrees of fiber dispersions according to different wavelengths. To minimize the dispersion effect, we fix the wavelength of the laser at 1310 nm. Although the linewidth of the laser needs to be as lower as possible, practical low-cost applications cannot promise the narrowest linewidth. So taking the real condition and the above results into account, we set the appropriate roll-off, linewidth and bias as 0.7, 1E6 and -1.4. With these fixed parameters we conduct the rest evaluation work.

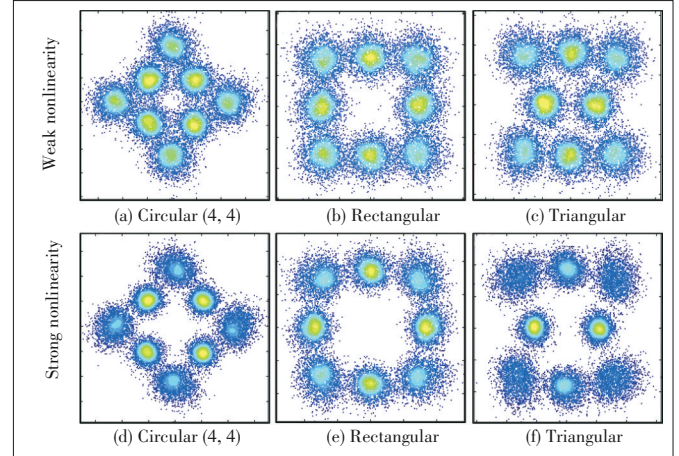
4 Results and Analysis

To present the nonlinearity distortion in the simulated system, we investigate the performance of BER versus amplitude of the Tx signal, as shown in Fig. 5. We fix the bias of the laser and then adjust the amplitude of the laser driver. As the amplitude increases, a turning point appears at the bottom of the performance curves of all the three shaped 8QAM constellations, showing that larger amplitude not only brings higher SNR but also induces more severe nonlinearity. From the three constellations shown in Fig. 5, corresponding to circled-

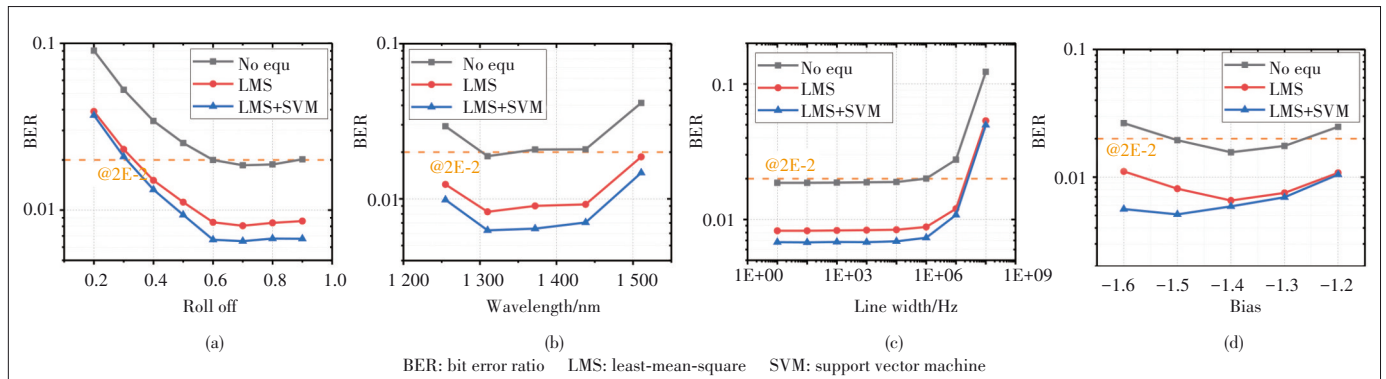
out optimal points, we can observe nonlinear influences of the points group at the outer ring is diffuse and their envelopes are elliptical but not circular. Fig. 6 shows the difference between strong nonlinearity and weak nonlinearity in three kinds of constellations. The warm color area is the place where plenty of points are converged while the cool color means the points have diverged. And by comparing the color of the outer ring with the inner ring, it is clear that those constellations under strong nonlinearity suffer more distortions. When the non-



▲ Figure 5. BER performance versus amplitude of the Tx signal (a) Circular (4, 4), (b) Rectangular and (c) Triangular



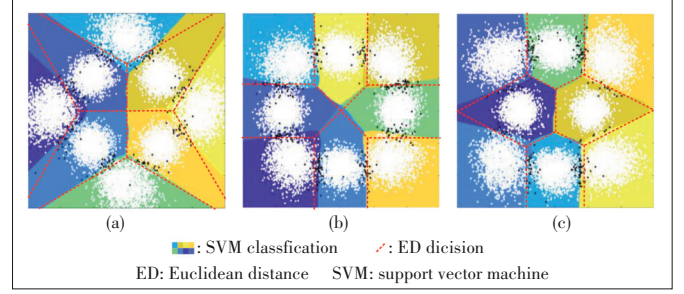
▲ Figure 6. Distortions under different levels of nonlinearity



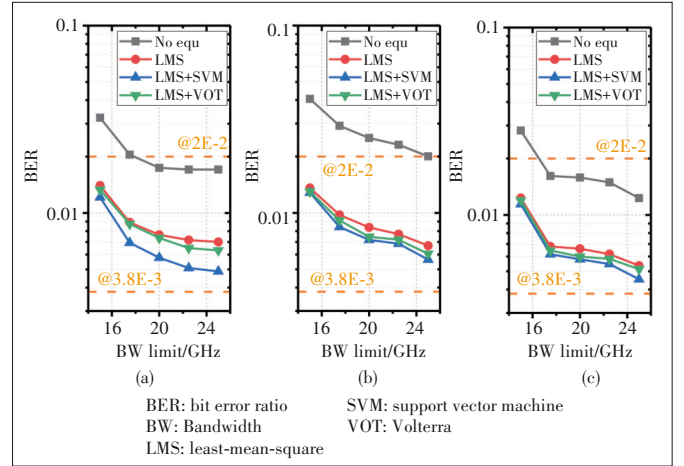
▲ Figure 4. BER of Circular (4, 4) versus (a) roll off of shaping filter, (b) wavelength of LD, (c) line width of LD and (d) bias of laser

linear impairments overcome the SNR gains, the system BER stops decreasing. By training the LMS equalizer with 2 000 samples of the waveform sequence, the equalized BER performance can be well below the 0.02 FEC threshold. However, as is shown in Fig. 7, when the constellation distortions occur, because the ED decision method will not change the decision boundaries which has been already decided as the GS coding completes, the performance can be further improved by using the SVM classifiers to redistribute the hyperplanes between distorted groups of constellation points. Moreover, the boundary changes between the SVM classifier and ED decision method are more obvious in the Circular (4, 4) constellation than the Rectangular and Triangular constellations. This phenomenon can be explained by the difference in the ratios mentioned in Section 2, the larger radius ratio of Circular (4, 4) results in a larger amplitude difference between the symbols on the outer ring and the inner ring. Taking the amplitude as the input of the function in Fig. 3(b), the nonlinear output differs as the input changes. Thus, if the amplitude difference is large, the nonlinear response is more apparent. As a result, Circular (4, 4) suffers more distortions and the hyperplanes appear more different from the ED decision boundaries than the other two constellations.

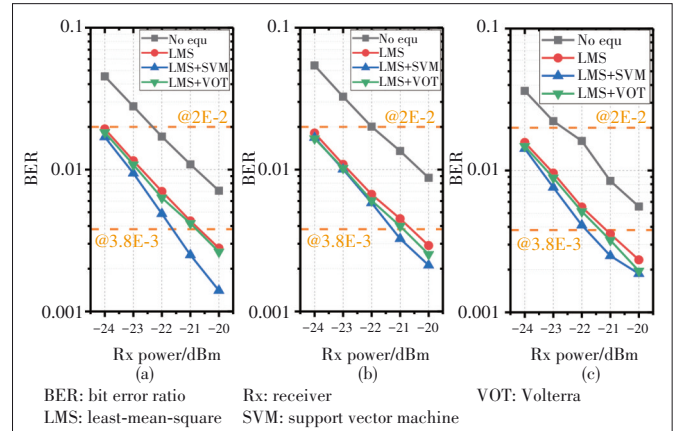
The results above mainly display the nonlinear influence on three kinds of constellations. The following part will discuss the performance of three equalization schemes on the BER, power budget, and complexity. First, we research the performance of BER versus bandwidth. In Fig. 8, as the bandwidth limitation increases, three shaped 8QAM signals all demonstrate better performance. The BER improvement after using SVM is remarkable in Circular (4, 4), indicating that it benefits more from the SVM classifier because of its stronger nonlinear distortions. The rectangular constellation has the worst performance in that the BER of the recovered signal is still greater than the 0.02 FEC threshold, when no equalization is applied. And the performance ranking of the three equalizers is LMS-SVM the first, LMS-VOT the second, and LMS the last. When the bandwidth reaches 25 GHz, the performance of three kinds of constellations is still unsatisfactory for they do not reach the hard-decision FEC (HD-FEC) threshold ($3.8\text{E-}3$). Therefore, we continue to study the BER performance versus the receiver sensitivity. Fig. 9 shows that the BER improves significantly as the received power increases. As the received power reaches -21 dBm, all kinds of constellations satisfy the HD-FEC threshold. The Triangular appears more suitable for transmitting in the PON channel for it meets the $3.8\text{E-}3$ threshold even without the assistance of the SVM classifier. But the SVM classifier helps Circular (4, 4) reach the lowest BER among all results at present, which suggests the superiority of the SVM classifier in the nonlinear circumstance. From Fig. 9 we can also get the receiver sensitivity as approximately -21.5 dBm because the BERs approach $3.8\text{E-}3$ with all three kinds of constellations at -21.5 dBm Rx power. Therefore, the



▲ Figure 7. The classification results of SVM and ED decision: (a) Circular (4, 4), (b) Rectangular and (c) Triangular



▲ Figure 8. BER performance versus bandwidth limitation of fiber system: (a) Circular (4, 4), (b) Rectangular and (c) Triangular



▲ Figure 9. BER performance versus received power: (a) Circular (4, 4), (b) Rectangular and (c) Triangular

received power is fixed to -21.5 dBm to analyze the power budget of the PON system in Fig. 10. The curve suggests that Circular (4, 4) achieves the lowest transmitting power requirements of 3.98 dBm. The BER performance gap between LMS-SVM and the other three methods is very significant in Circular (4, 4), which is explained by the larger radius ratio and thus more severe distortions. For Rectangular and Triangular, the transmitting power should increase to 10.79 dBm and 8.75 dBm separately so that the BERs can meet the HD-FEC threshold. It is meaningful that the Circular (4, 4) joint LMS-

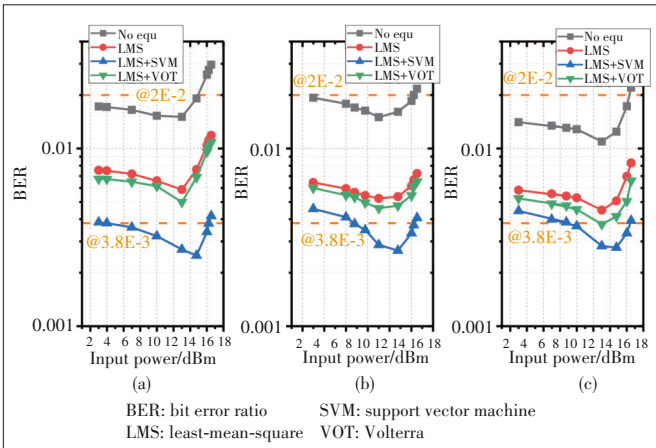
SVM solution has saved at least 4.77 dB of input power compared with the solutions transmitting the other two constellations. Due to fiber nonlinearity impairments, as the fiber input power increases, the BER performance of all of the three solutions is getting worse. The same maximum power budget of 37.52 dB is achieved after 20 km SSMF in all three solutions. In Figs. 9 and 10 we can also find that the Triangular constellation performs the best if all three constellations are just equalized by LMS, which may draw interest if the extremely low complexity in PON system is required.

Furthermore, we make a comprehensive complexity comparison of the three equalization methods and the computational costs are listed in Table 2 in terms of the multiplications and additions. The computational complexity differs at the training stage and the prediction stage because the training processes contain extra weights updating procedure. The LMS and the LMS-VOT equalizers process the waveform of the Rx signal while the SVM classifier deals with the signal constellations. So, the complexity of SVM depends on different parameters with the LMS and LMS-VOT algorithms. In Table 2, T_1 is the length of the training waveform sequence for LMS and LMS-VOT, T_2 is the number of the training symbols for SVM, N_s is the number of support vectors, d is the dimension of classification results, and M_1 and M_2 refer to the tap numbers of the first order and the second order adaptive filter. In this simula-

tion, $T_1 = 2000$, $T_2 = 800$, $d = 8$, $M_1 = M_2 = 15$, and N_s is a variable that varies as the hyperplanes adjust. Since in 8QAM constellations only a few points satisfy $f(x) = \pm 1$ in Eq. (2) and most of the constellation points locate far from the hyperplane, the typical value of N_s is much smaller than T_2 , approximately 10% of T_2 . Taking a specific value $N_s = 80$ into account, the computational complexity of SVM is $O(512\ 640)$ while the LMS-VOT algorithm contains 754 000 additions and 994 000 multiplications at the training stage. It needs to be addressed that the LMS-VOT just uses the first and the second order Volterra kernels. Further increasing the order of kernels will bring unacceptable computational costs for the PON system. After training every time in the prediction procedure, the complexity of the proposed SVM is $O(640)$, the same level as the LMS-VOT algorithm that makes 136 additions and 255 multiplications. The above analysis suggests that by limiting the number of the training symbols, the computational cost of the proposed linear SVM, together with the LMS equalizer, is well controlled at both stages compared with the classic LMS-VOT adaptive filter. Above all, the proposed LMS-SVM scheme promises better BER performance at a well-controlled computational complexity for the PON system.

5 Conclusions

Nonlinearity impairments and distortions have been bothering the bandwidth constrained PON system for a long time and limit the development of capacity in the PON system. To mitigate impairments accumulated in optical components and PON channels, we propose a low computational complexity and efficient constellation shaped 8QAM joint SVM scheme. On the transmitter side, three kinds of shaped 8QAM constellations are generated to resist the influence of noise and distortions. On the receiver side, simple multi-class linear SVM classifiers are utilized to replace complex equalization methods. The hyperplane generation process of SVM and the non-linear influence on hyperplane are discussed to explain why SVM is superior to the Euclidean distance decision method. Simulation results show that with the bandwidth of 25 GHz, overall bitrate of 50 Gbit/s, and under hard-decision FEC threshold, transmission can be realized by employing Circular (4, 4) shaped 8QAM joint SVM classifier at the maximum pow-



▲ Figure 10. BER performance versus fiber input power: (a) Circular (4, 4), (b) Rectangular and (c) Triangular

▼ Table 2. Computational complexity

Methods	Training		Prediction	
	Additions	Multiplications	Additions	Multiplications
LMS	$(M_1 + M_1 + 1)T_1$	$(M_1 + M_1 + 1)T_1$	M_1	M_1
LMS-VOT	$(2M_1 + \frac{M_2(M_2 + 1)}{2} + M_2^2 + 2)T_1$	$(2M_1 + M_2(M_2 + 1) + M_2^2 + 2)T_1$	$M_1 + \frac{M_2(M_2 + 1)}{2} + 1$	$M_1 + M_2(M_2 + 1)$
SVM ^[19]	$O(N_s^2 + N_s d T_2)$		$O(N_s d)$	

M_1 is the tap number of the linear part, M_2 is the tap number of the nonlinear part, T_1 is the length of the training sequence, T_2 is the number of the training symbols, N_s is the number of support vectors and d is the dimension of classification.

LMS: least-mean-square SVM: support vector machine VOT: Volterra

er budget of 37.5 dB. And at least 4.77 dB input power difference occurs between Circular (4, 4) and the other two constellations by using SVM, which indicates the Circular (4, 4) shaped 8QAM joint SVM classifier is more suitable to be transmitted in the PON system with lower input power and less nonlinear distortions.

References

- [1] IEEE. Physical layer specifications and management parameters for 25 Gbit/s and 50 Gbit/s passive optical networks: IEEE 802.3ca Task Force [S]. 2018
- [2] HOUTSMA V, VEEN DVAN. Optical strategies for economical next generation 50 and 100G PON [C]/Optical Fiber Communication Conference. OFC, 2019. DOI:10.1364/ofc.2019.m2b.1
- [3] JI H L, YI L L, LI Z X, et al. Field demonstration of a real-time 100-Gbit/s PON based on 10G-class optical devices [J]. Journal of lightwave technology, 2017, 35(10): 1914 – 1921. DOI: 10.1109/JLT.2016.2633482
- [4] HOUTSMA V, VEEN DVAN. Demonstration of symmetrical 25 Gbit/s TDM-PON with 31.5 dB optical power budget using only 10 Gbit/s optical components [C]/2015 European Conference on Optical Communication. IEEE, 2015: 1 – 3. DOI:10.1109/ECOC.2015.7341691
- [5] WEI J L, EISELT N, GRIESSER H, et al. Demonstration of the first real-time end-to-end 40-Gbit/s PAM-4 for next-generation access applications using 10-Gbit/s transmitter [J]. Journal of lightwave technology, 2016, 34(7): 1628 – 1635. DOI:10.1109/JLT.2016.2518748
- [6] IEEE. Ethernet amendment 10: media access control parameters, physical layers, and management parameters for 200 Gbit/s and 400 Gbit/s 802.3bs-2017: IEEE 802.3bs-2017 [S]. 2017
- [7] ZHANG J, YU J J, CHIEN H, et al. Demonstration of 100 Gbit/s/λ PAM-4 TDM-PON supporting 29 dB power budget with 50 km reach using 10 G class O-band DML transmitters [C]/Optical Fiber Communication Conference Post-deadline Papers. OSA, 2019. DOI:10.1364/ofc.2019.th4c.3
- [8] ZHANG J W, YU J J, LI F, et al. 11 × 5 × 93 Gbit/s WDM-CAP-PON based on optical single-side band multi-level multi-band carrierless amplitude and phase modulation with direct detection [J]. Optics express, 2013, 21(16): 18842. DOI: 10.1364/oe.21.018842
- [9] WEI J L, INGHAM J D, CUNNINGHAM D G, et al. Performance and power dissipation comparisons between 28 Gbit/s NRZ, PAM, CAP and optical OFDM systems for data communication applications [J]. Journal of lightwave technology, 2012, 30(20): 3273 – 3280. DOI:10.1109/JLT.2012.2213797
- [10] YIN S, HOUTSMA V, VEEN DVAN, et al. Optical amplified 40-Gbit/s symmetrical TDM-PON using 10-Gbit/s optics and DSP [J]. Journal of lightwave technology, 2017, 35(4): 1067 – 1074. DOI: 10.1109/JLT.2016.2614767
- [11] WANG C, DU J B, CHEN G Y, et al. QAM classification methods by SVM machine learning for improved optical interconnection [J]. Optics communications, 2019, 444: 1 – 8. DOI: 10.1016/j.optcom.2019.03.058
- [12] NIU W Q, HA Y, CHI N. Support vector machine based machine learning method for GS 8QAM constellation classification in seamless integrated fiber and visible light communication system [J]. Science China information sciences, 2020, 63(10): 202306. DOI: 10.1007/s11432-019-2850-3
- [13] SAIN S R. The nature of statistical learning theory [J]. Technometrics, 1996, 38(4): 409. DOI: 10.1080/00401706.1996.10484565
- [14] HSU C W, LIN C J. A comparison of methods for multiclass support vector machines [J]. IEEE transactions on neural networks, 2002, 13(2): 415 – 425. DOI: 10.1109/72.991427
- [15] JOACHIMS T. Training linear SVMs in linear time [C]/The 12th ACM SIG-KDD International Conference on Knowledge Discovery and Data Mining. ACM, 2006: 217 – 226. DOI: 10.1145/1150402.1150429
- [16] KEERTHI S S, DECOSTE D. A modified finite Newton method for fast solution of large scale linear SVMs [J]. Journal of machine learning research, 2005, 6(12):341–361
- [17] CHEN K Z, CHEN L W, LIN C Y, et al. 224-Gbit/s transmission for next-generation WDM long-reach PON using CAP modulation [C]/2016 Optical Fiber Communications Conference and Exhibition (OFC). IEEE, 2016: 1 – 3
- [18] STOJANOVIC N, KARINOU F, QIANG Z, et al. Volterra and Wiener equalizers for short-reach 100 G PAM-4 applications [J]. Journal of lightwave technology, 2017, 35(21): 4583 – 4594. DOI: 10.1109/JLT.2017.2752363
- [19] BURGESS C J C. A tutorial on support vector machines for pattern recognition [J]. Data mining and knowledge discovery, 1998, 2(2): 121 – 167. DOI: 10.1023/A: 1009715923555

Biographies

LI Zhongya is with the Department of Communication Science and Engineering, School of Information Science and Technology, Fudan University, China.

CHEN Rui is with the Department of Communication Science and Engineering, School of Information Science and Technology, Fudan University, China.

HUANG Xingang is a senior expert of technical pre-research of ZTE Corporation. He received the M.S. degree in physics from Xi'an Jiaotong University, China in 2008. He is engaged in the research of optical access technology, especially in WDM-PON, TWDM-PON, NG-EPON, 50 G PON.

ZHANG Junwen is with the Department of Communication Science and Engineering, School of Information Science and Technology, Fudan University, China.

NIU Wenqing is with the Department of Communication Science and Engineering, School of Information Science and Technology, Fudan University, China.

LU Qiuyi is with the Department of Communication Science and Engineering, School of Information Science and Technology, Fudan University, China.

CHI Nan (nanchi@fudan.edu.cn) is with the Department of Communication Science and Engineering, School of Information Science and Technology, Fudan University, China.



General Introduction of Non-Terrestrial Networks for New Radio

HAN Jiren, GAO Yin

(Algorithm Department, Wireless Product R&D Institute, ZTE Corporation, Shanghai 201203, China)

DOI: 10.12142/ZTECOM.2022S1010

<http://kns.cnki.net/kcms/detail/34.1294.TN.20220107.1631.002.html>, published online January 7, 2022

Manuscript received: 2021-07-02

Abstract: In the new radio (NR) access technology, non-terrestrial networks (NTN) are introduced to meet the requirement of anywhere and anytime connections from the world market. With the introduction of NTN, the NR system is able to offer the wide-area coverage and ensure the service availability for users. In this paper, the general aspects of NTN are introduced, including the NTN architecture overview, the impact of NTN on next-generation radio access network (NG-RAN) interface functions, mobility scenarios and other NTN related issues. The current progress in 3GPP Release 17 is also provided.

Keywords: NR; NTN; satellite; payload

Citation (IEEE Format): J. R. Han and Y. Gao, "General introduction of non-terrestrial networks for new radio," *ZTE Communications*, vol. 20, no. S1, pp. 72 – 78, Jan. 2022. doi: 10.12142/ZTECOM.2022S1000.

1 Introduction

In a non-terrestrial network (NTN), the satellite or airborne vehicle is able to perform as either a relay node or a base station in the wireless communication system. The NTN can provide much larger area coverage than a traditional terrestrial network; in addition, the NTN is able to ensure the connectivity in regions where current terrestrial networks are difficult or costly to cover, such as airplanes, vessels and remote rural areas^[1-2]. Therefore, the NTN could be an appropriate solution to complementing the current terrestrial network to provide the service for users in the specific regions. In January 2020, the 3rd Generation Partnership Group (3GPP) completed a study project for this purpose named "Solutions for NR to support non-terrestrial networks (NTN)". In addition, a new working project with the same name has started from August 2020. In this paper, we provide a review of NTN, NTN based next-generation radio access network (NG-RAN) architecture, the impact of NTN on NG-RAN interface protocol, and the current progress of the 3GPP Release 17 phase. At the end of the paper, conclusions are proposed.

2 NTN Overview and Scenarios

An NTN refers to a network or segment of a network using Radio Frequency (RF) resources on board a satellite or an unmanned artificial system (UAS) platform. In detail, the NTN architecture can be divided into two cases with transparent payload and regenerative payload respectively. And the NTN

reference scenarios can be classified into six cases^[3].

2.1 NTN Architecture

Typically, the NTN architecture comprises of the following elements:

- One or several satellite gateways that connect the NTN to a public data network;
- A feeder link or radio link between a satellite gateway and the satellite or the UAS platform;
- A service link or radio link between the user equipment (UE) and the satellite or the UAS platform;
- A satellite or a UAS platform which may implement either a transparent or a regenerative (with on board processing) payload. The satellite or the UAS platform typically generates several beams over a given service area bounded by its field of view. The footprints of the beams are typically of an elliptic shape. The field of view of the satellite or the UAS platform depends on the on board antenna diagram and the minimum elevation angle.
- Inter-satellite links (ISL) that optionally exist in a constellation of satellites. This will require regenerative payloads on board the satellites. The ISL may operate in RF or optical bands.
- UE is served by the satellite or the UAS platform within the targeted service area.

As shown in Fig. 1, a transparent payload is the payload that changes the frequency carrier of the uplink RF signal, filters and amplifies it before transmitting it on the downlink. Therefore, the waveform of the signal repeated by the transpar-

ent payload is not changed; in other words, the NTN with the transparent payload can be regarded as a relaying node at the network side.

As shown in Fig. 2, a regenerative payload is the payload that transforms and amplifies an uplink RF signal before transmitting it on the downlink. Further, the signal transformation is the digital processing of the signal, such as demodulation, decoding, re-encoding, re-modulation and filtering. With all these equivalent or similar functions as the base station, the NTN with the regenerative payload can be regarded as a base station at the network side.

In the NTN, there are several platforms with different attributes, and the different NTN platforms can provide different services based on their own attributes. Table 1 shows the details of these NTN platform types.

The geostationary earth orbit (GEO) satellite and UAS platform are used to provide continental, regional or local service because of the relatively fixed position with respect to a given earth point. While, the low-earth orbit (LEO) and medium-

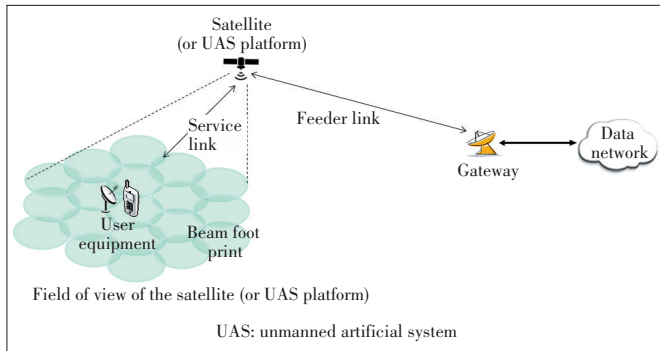
earth orbit (MEO) satellites are in the relatively moving positions with respect to a given earth point; hence, the constellation of the LEO and MEO satellites is used to provide services in both Northern and Southern hemispheres. In some cases, with appropriate allocation and planning, such as optimized orbit inclination, beams and ISL, the constellation is able to provide global coverage including the Polar Regions. However, the coverage of the high elliptical orbit (HEO) satellite is limited, so the HEO satellite system is not considered in this paper.

In addition, as the GEO satellite is served by the satellite gateway that is located across the fixed regional area covered by the GEO satellite, it can be assumed that the UE in a cell is served by only one satellite gateway, just as the normal case in the traditional terrestrial network. However, for the non-GEO satellite, it is served successively by one or several satellite gateways at a time. In this case, the system should ensure the continuity of service links and feeder links between the successive serving satellite gateways within the time duration.

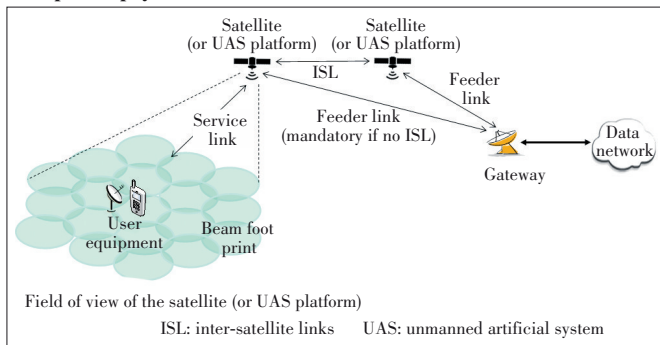
2.2 NTN Reference Scenarios

According to different criteria, the NTN system supporting UE access can be classified into six reference scenarios, which are shown in Table 2.

In short, considering the criteria, the first one is whether the satellite is a circular orbiting platform or a notional station keeping platform, i.e., the satellite could be LEO or GEO satellite. The second one is whether the satellite is with transparent payload or regenerative payload. The third one is whether the satellite beam is fixed or steerable, which results in moving or fixed beam foot print on the ground respectively.



▲ Figure 1. Typical scenario of non-terrestrial networks based on transparent payload



▲ Figure 2. Typical scenario of non-terrestrial networks based on regenerative payload

▼ Table 1. Types of NTN platforms

Platform	Altitude Range/km	Orbit	Typical Beam Footprint Size/km
LEO satellite	300 – 1 500	Circular around the earth	100 – 1 000
MEO satellite	7 000 – 25 000		100 – 1 000
GEO satellite	35 786	Notional station keeping position fixed in terms of elevation/azimuth with respect to a given earth point	200 – 3 500
UAS platform (including HAPS)	8 – 50 (20 for HAPS)		5 – 200
HEO satellite	400 – 50 000	Elliptical around the earth	200 – 3 500

GEO: geostationary earth orbit HAPS: High Altitude Platform Station HEO: high elliptical orbit LEO: low-earth orbit MEO: medium-earth orbit UAS: unmanned artificial system

3 NTN Based NG-RAN Architecture

The NG-RAN logical architecture described in TS 38.401 is used as baseline for NTN scenarios^[4]. The NTN based NG-RAN architecture can be divided into the transparent satellite based NG-RAN architecture and regenerative satellite based NG-RAN architecture.

3.1 Transparent Satellite Based NG-RAN Architecture

In this architecture, the satellite payload performs the function of frequency conversion and RF amplification in both downlink and uplink, which means that the satellite plays a role of a relay node in the network.

As shown in Fig. 3, the satellite repeats the NR-Uu radio in-

terface from the feeder link to the service link in the downlink communication and repeats the NR-Uu radio interface from the service link to the feeder link in the uplink communication. Thus, the satellite does not terminate the NR-Uu radio interface. The Satellite Radio Interface (SRI) on the feeder link is also the NR-Uu interface.

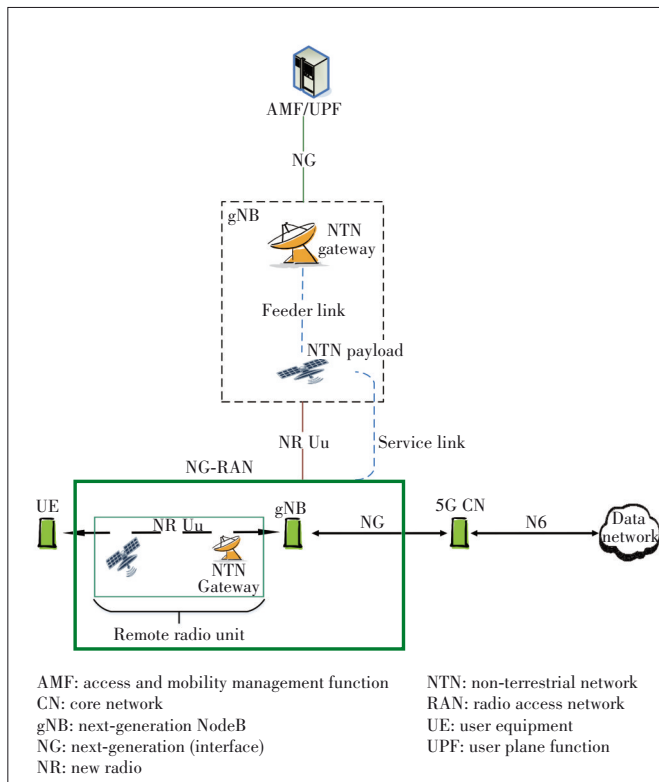
Furthermore, the NTN gateway receives the signal via NR-Uu from the satellite and transmits the signal to the “on ground” gNB in the uplink communication and vice versa. Hence, the function of the NTN gateway is just to forward the NR-Uu signal. Generally, different transparent satellites could be connected to the same gNB on the ground.

For the LEO satellite with transparent payload, the “on ground” gNB transceives the NR-Uu signal to/from the earth fixed NTN gateways in a planned and delicate way, e.g. via operations, administration, and maintenance (OAM) provision, and then the NTN gateway further transceives the NR-Uu signal to/from the target LEO satellites according to Ephemeris

▼ Table 2. Reference scenarios

Non-Terrestrial Access Network	Transparent Satellite	Regenerative Satellite
GEO based non-terrestrial access network	Scenario A	Scenario B
LEO based non-terrestrial access network: steerable beams	Scenario C1	Scenario D1
LEO based non-terrestrial access network: beams moving with the satellite	Scenario C2	Scenario D2

GEO: geostationary earth orbit LEO: low-earth orbit



▲ Figure 3. Transparent satellite, without gNB on board

information in a planned way. To be more specific, the Ephemeris information describes the orbital trajectory information or coordinates for the NTN vehicles, and such information is provided on a regular basis or upon demand to the gNB.

3.2 Regenerative Satellite Based NG-RAN Architecture

In this architecture, the satellite payload performs the function of regeneration of the signals from the earth, which means that the satellite plays a role of the whole or part of a base station.

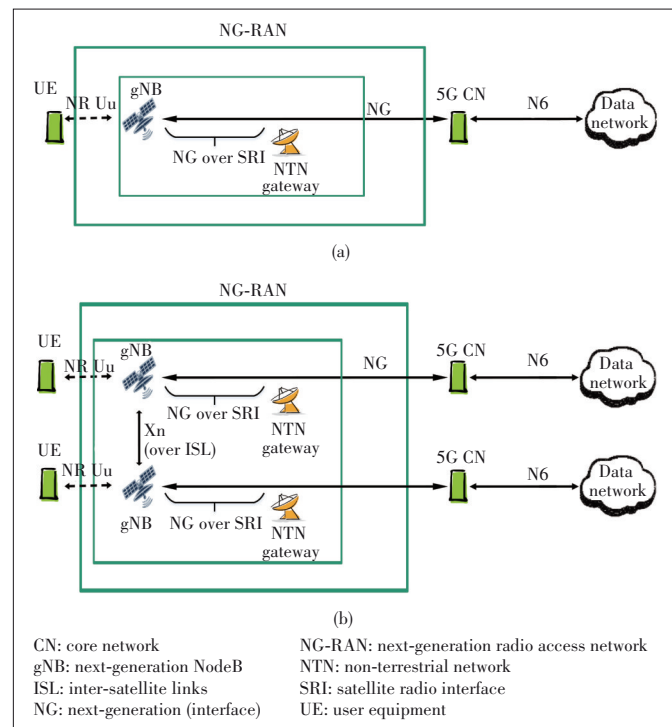
In detail, the regenerative satellites can be divided into the regenerative satellite with gNB on board and that with gNB-DU on board. Further, the regenerative satellite with gNB on board can be divided into the regenerative satellite with and without ISL.

3.2.1 Regenerative Satellite with gNB on Board

As shown in Fig. 4(a), the satellite performs the function of a gNB, and the SRI on the feeder link is the NG interface. And the NTN gateway is a Transport Network Layer (TNL) node.

As shown in Fig. 4(b), in addition to the features in Fig. 4(a), the satellite payload provides ISL between the satellites, and the ISL could be a radio interface, such as the Xn interface.

The UE served by a gNB on the satellite could access the 5G core network (CN) via ISL, which means the gNBs on the different satellites could be connected to the same 5GCN on the ground. If the satellite hosts more than one gNB, the same SRI will transport all the corresponding NG interface instances.



▲ Figure 4. Regenerative satellite with gNB on board: (a) without ISL; (b) with ISL

As the Xn could exist over the ISL, the interface management functions over Xn in the Terrestrial Network should also be applied on board, e.g. Xn setup, Xn reset, cell configuration information exchange.

3.2.2 Regenerative Satellite with gNB-DU on Board

For the regenerative satellite with gNB-DU on board as shown in Fig. 5, the difference with the case in Fig. 4(a) is that the gNB-CU is located on the ground and the SRI is the F1 interface.

Similar with the case in Fig. 4(b), the gNB-DU on different satellites could be connected to the same gNB-CU on the ground. If the satellite hosts more than one gNB-DU, the same SRI will transport all the corresponding F1 interface instances.

3.3 Multiple Connectivity with NTN Based NG-RAN

In this paper, we focus on the dual connectivity involving the terrestrial network based NG-RAN and the non-terrestrial networks based NG-RAN for UE. For the NTN based NG-RAN, the transparent and regenerative satellites with gNB or gNB-DU on board are considered. The combination of the two network access modes is able to meet the requirement of many communication scenarios (e.g. users in the highway, high speed train or the airplane) and improve the service performance^[5].

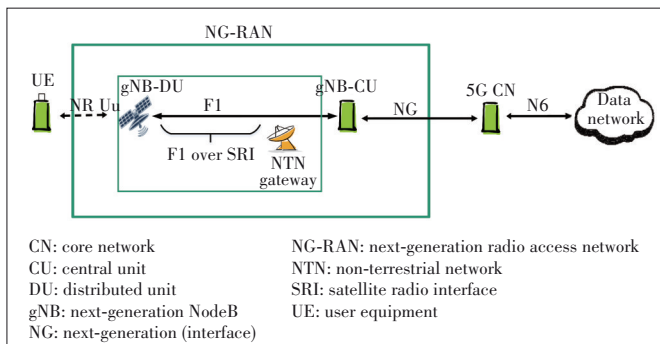
The UE could be served by one NTN based NG-RAN and one terrestrial network based NG-RAN at the same time (Access Mode 1). Meanwhile, the UE could also be connected by two NTN based NG-RANs at the same time (Access Mode 2).

To be more specific, Access Mode 1 can be further divided into the transparent satellite scenario and the regenerative satellite scenario, which are shown in Figs. 6(a) and 6(b) respectively.

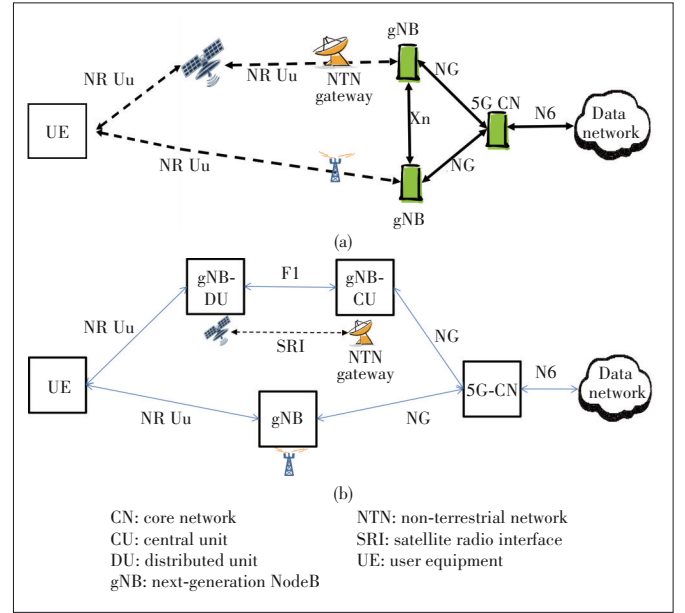
In Fig. 6(a), for the transparent satellite, the same gNB could serve the NR cells by both the terrestrial access network and the non-terrestrial access work. In Fig. 6(b), the regenerative satellite could be gNB or gNB-DU on board.

Access Mode 2 can also be further divided into the transparent satellite scenario and the regenerative satellite scenario, which are shown in Figs. 7(a) and 7(b) respectively.

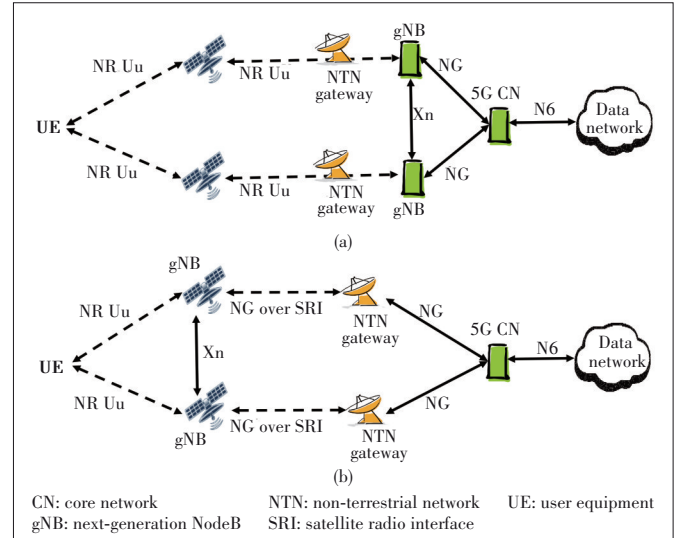
The case of the combination of two transparent satellites with either GEO or LEO is beneficial to provide services to the UE in rural areas. The LEO satellite can be used to pro-



▲ Figure 5. Regenerative satellite with gNB-DU on board



▲ Figure 6. Dual connectivity involving (a) transparent NTN-based NG-RAN and cellular NG-RAN and (b) regenerative NTN-based NG-RAN (gNB-DU) and cellular NG-RAN



▲ Figure 7. Multi-connectivity between (a) two transparent NTN-based NG-RANs and (b) two regenerative NTN-based NG-RANs (gNB on board)

vide the delay sensitive traffic, while the GEO satellite can be used to provide the additional bandwidth to meet the throughput requirements from users. The combination of the two regenerative satellites could bring similar benefits.

4 Impact of NTN on NG-RAN Architecture and Interface Protocol

4.1 Tracking Area Management

The concepts of registration and tracking areas of NTN are

similar to those in the NR terrestrial network. To be more specific, a tracking area (TA) corresponds to a fixed geographical area, which is used for UE access control, location registration, paging and mobility management. A registration area can comprise of one or several TAs.

As discussed in Section 2.2, for the NTN scenarios A, B, C1 and D1, the NTN cells are relatively fixed on the ground. Therefore, a TA could correspond to one or several NTN cells, and it can be applied in tracking area management and paging procedures. For the scenarios C1 and D1, the beam footprints of the LEO satellites are temporarily earth fixed, and the beam footprints over a given NTN cell on the ground are stationary within a time period before the satellites switch to another NTN cell. In this case, a TA could be assigned to each NTN cell, and the satellites should change the broadcast Tracking Area Code (TAC) between two successive NTN cells. For the NTN scenarios C2 and D2, the NTN cells are relatively moving on the ground, and some adaptations are needed in tracking area management and paging procedures. Two options can be considered as follows.

Option 1 is TA defined on the satellite. In this option, an NTN cell only has one Tracking Area Identity (TAI) per Public Land Mobile Network (PLMN) ID, which is the same as the terrestrial cell. However, for the NTN scenarios C2 and D2, as the LEO satellite moves around the orbit, the coverage of the TAI also changes. In this case, from the perspective of a stationary UE, the TAI changes accordingly.

Option 2 is TA defined on the ground. In this option, the TAI corresponds to a specific geographical area. In this case, an NTN cell may need to broadcast multiple TAIs per PLMN ID, which is not aligned with the common principle in the terrestrial network that one cell only has one TAI per PLMN ID.

As the details of this topic are still under study, the choice of the option should be further decided with the progress of the NTN work item in 3GPP.

4.2 Mobility Scenarios in Connected Mode

In an NTN, some mobility scenarios in a connected mode can be considered, including the intra-satellite handover, the inter-satellite handover and the inter-access handover. In detail, the intra-satellite handover is the case between cells served by the same satellite, the inter-satellite handover is the case between cells served by different satellites, and the inter-access handover is the case between the cellular access and

the satellite access. Based on the types of the serving satellites (i.e., with transparent or regenerative payload), the different types of the NTN handover are able to correspond with the applicable NG-RAN handover procedures in 3GPP, and the details are shown in Table 3.

4.3 Network Identities

As GEO satellites are relatively fixed with respect to a certain point on the ground, the current network identities in the terrestrial RAN, such as gNB IDs, cell IDs and TAC, could be reused.

While for the non-GEO satellites including LEO and MEO, as the satellites move across the geographical area of interest, their satellite beams also cover different parts of the area. Hence, the association between the logical cells and the physical satellite beams should be clarified.

If the association between the logical cells and the physical satellite beams is continuously reconfigured, the same network identities are also associated with the same geographical area. This scenario can be identified as “stationary identifiers on ground”. In this case, stationary UE on the ground will always be covered by the same cell identifier in the same position.

If the association between the logical cells and the physical satellite beams is fixed, the network identities will sweep across the coverage area with the satellite beams. This scenario can be identified as “moving identifiers on ground”. In this case, stationary UE on the ground will be covered by different cell identifiers in the same position. The multiple cells within one moving satellite will move together. Hence, the neighbor relations will keep unchanged with the satellite motion.

For both the cases, once a satellite moves out of the coverage, the corresponding cell network identifier will become unavailable in the coverage area, which could trigger the RAN interface (e.g. NG or Xn interface) setup and configuration update procedures. The Ephemeris information could help the RAN side to make the decision for the procedures.

Considering the impact on the interface protocol over NG and Xn, the access restriction for all types of NR RATs based on satellite constellations should be explicitly introduced, i.e., the NR for LEO, MEO, GEO and other SAT should be used as 3GPP access in 5G system. If supported, the access restriction should apply on initial access, i.e. the access and mobility

▼Table 3. NG-RAN procedures versus NTN handover scenarios

NTN Handover Scenario	Transparent Satellite	Regenerative Satellite (gNB on Board)	Regenerative Satellite (gNB-DU on Board)
Intra-satellite handover	Intra-gNB handover procedure or inter-gNB handover procedure	Intra-gNB handover procedure	Intra-gNB-CU mobility/intra-gNB-DU handover or inter-gNB-CU handover
Inter-satellite handover	Inter-gNB handover procedure or intra-gNB handover procedure	Inter-gNB handover procedure	Intra-gNB-CU mobility/inter-gNB-DU mobility or inter-gNB-CU handover
Inter-access handover		Inter AMF/UPF handover procedure or intra AMF/UPF handover procedure (out of RAN scope)	Intra-gNB handover procedure or inter-gNB handover procedure

AMF: access and mobility management function CU: central unit DU: distributed unit gNB: next-generation NodeB RAN: radio access network UPF: user plane function

management function (AMF) should be aware of the satellite access type; and the access restriction should also apply on the RAN mobility in a connected mode, i.e., the RAN node should be aware of the access restrictions.

From the aspect of RAN, only the serving NTN Uu cell ID (broadcast cell ID of the serving cell) and the broadcast TAC(s) would be available at initial access. As a consequence, it assumes that at initial access the gNB is typically not able to provide a Cell Global Identity (CGI) with location granularity to the User Location Information (ULI) similar to the ULI provided in terrestrial network; also at initial access, the CGI provided in the ULI may represent a geographical area spanning multiple TACs.

After Access Stratum (AS) security is setup, it assumes that the NG-RAN will be able to obtain UE's location information (e.g. Global Navigation Satellite System (GNSS) information), and thereby construct a CGI for the ULI, satisfying accuracy requirements comparable to those for terrestrial networks.

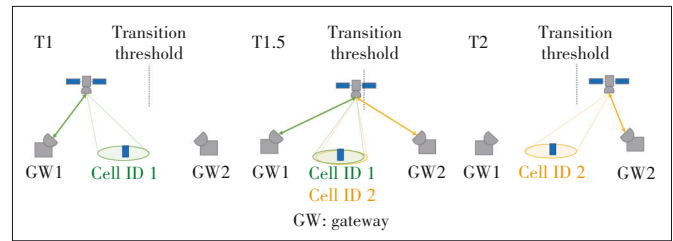
4.4 Feeder Link Switch-Over

During the satellite movement in the NTN, the switch-over of the feeder link between the different NTN gateways could not be avoided, especially for non-GEO satellites. The switch-over could happen when the satellite moves out of the vision of the current NTN gateway^[6]. In a nutshell, a feeder link switch-over is the procedure where the feeder link is changed from a source NTN Gateway to a target NTN Gateway for a specific NTN payload. The feeder link switch-over happens at the transport network layer.

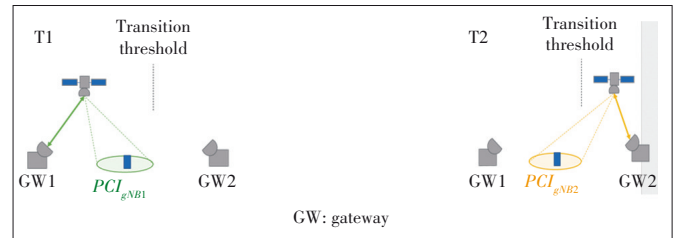
A feeder link switch-over may result in transferring the established connection for the affected UE between two gNBs. For soft feeder link switch-over, an NTN payload is able to connect to more than one NTN gateway during a given period, i.e., a temporary overlap can be ensured during the transition between the feeder links. For hard feeder link switch-over, an NTN payload only connects to one NTN gateway at any given time, i.e., a radio link interruption may occur during the transition between the feeder links. Figs. 8 and 9 show two kinds of feeder link switch-over.

In soft feeder link switch-over (Fig. 8), at time T1, the satellite is approaching the geographical location where the transition served by next gateway (GW) will happen. At time T1.5, the satellite is served by two GWs and at time T2, the transition to next GW is finished.

With the switch-over of a feeder link, the handling of the area covered by the satellite through this gateway (GW1) will move to another gateway (GW2). The UE served in this area that is connected through this GW will have to be handed over to the new GW. During the switch-over, the satellite will establish a connection with the new GW while maintaining the connection with the current GW within a short time period. It will setup new cells through the new GW to cover the area, allowing the UE located in the concerned area to be moved to the new cells before disconnecting the feeder link with the old



▲ Figure 8. Soft feeder link switch-over



▲ Figure 9. Hard feeder link switch-over

GW, without service interruption for the UE^[7].

In hard feeder link switch-over (Fig. 9), at time T1, the satellite stops to transfer the signaling from the serving GW1. At time T2, the satellite starts to transfer the signaling from the target GW2.

In case the satellite does not have two feeder links established at the same time, a hard switch-over must be performed to change the gateway. In this case there is no overlapping time between GW1 and GW2. For the switch-over, the gNB1 connected with GW1 will delete the old cell while the GW1 releases the feeder link and then the GW2 will establish a new feeder link, which will allow the gNB2 connected with GW2 to establish a new cell with the same coverage as the old cell. The UE served by the old cell should be moved to the new cell.

A potential non-UE-associated procedure could be introduced over Xn. With this procedure, the new gNB is able to get the information of the satellite it should be connected to and the served cell information from the old gNB. In this procedure, the satellite needs to connect two NTN gateways at the same time within a certain time period, which means that only the soft switch-over could be applied. To achieve a unified feeder link switch-over procedure for both the soft and hard switch-over, this procedure could be reused with some enhancements, e.g., introducing the ephemeris data and accurate time information as the assistance information to prepare and execute the hard switch-over. With the information, the new gNB on the ground could be aware of which LEO satellite it is connecting to via its NTN gateway at certain a time period. It is feasible for the new gNB to predict the LEO satellite which will connect to the NTN-GW in the future time. Thus, the new gNB could be aware of the scheduling of switch-over events to minimize the radio link interruption delay.

5 Current Progress in 3GPP Release 17

After August 2020, the 3GPP has started the work item of

the NTN, and it is agreed that only the transparent satellite is studied in Release 17^[8-9].

For network identities, the current NG-RAN identities are reused for NTN, including AMF name, NR Cell Global Identifier (NCGI), gNB ID, global gNB ID, TAI and Single Network Slice Selection Assistance Information (S-NSSAI). There is no need to identify the LEO satellite and NTN gateway. In addition, a cell ID provided to the 5GCN within the user location information corresponds to a fixed geographical area.

For the feeder link switch-over, the existing per-UE Xn and NG handover functions are used to support the switch-over. It is assumed that the information exchanged in existing handover procedures can be used for NTN purposes. 3GPP supports NTN with central coordination of switch-overs. In case of centrally coordinated switch-over, no signaling is needed on Xn/NG to coordinate the actual switch-over.

In addition, the existing paging mechanism in the terrestrial network can be reused for NTN and there is no need for enhancement on paging. The current Automatic Neighbor Relation (ANR) mechanisms are applicable for NTN. There is no need of enhancements for solving the Physical Cell Identity (PCI) conflict with satellites in Release 17.

6 Conclusions

In this paper, we introduce the NTN, including the NTN basic architecture and reference scenarios. The NTN based NG-RAN architectures with transparent satellite and regenerative satellite are also presented. In addition, we discuss the impact of NTN on NG-RAN architecture and interface protocol, and propose some solutions to different related issues. In the end, the current progress of 3GPP Release 17 is provided.

References

- [1] RINALDI F, H-LMAATTANEN, TORSNER J, et al. Non-terrestrial networks in 5G & beyond: a survey [J]. IEEE access, 2020, 8: 165178 - 1652008. DOI: 10.1109/ACCESS.2020.3022981
- [2] TIAN K B, YANG Z, ZHANG N. Prospects for the air-space-ground integrated network technology [J]. ZTE technology journal, 2021, 27(5): 2-6. DOI: 10.12142/ZTETJ.202105002
- [3] 3GPP. Solutions for NR to support non-terrestrial networks (release 16): 3GPP TR38.821 [S]. 2020
- [4] 3GPP. NG-RAN, architecture description (release 16): 3GPP TS 38.401 [S]. 2020
- [5] 3GPP. Study on new radio (NR) to support non-terrestrial networks (release 15): 3GPP TR38.811 [S]. 2020
- [6] Thales. On NTN feeder link switch over: 3GPP R3-205173 [R]. 2020
- [7] ZTE. Initial thoughts on NTN LEO feeder link switch-over: 3GPP R3-204666 [R]. 2020.
- [8] 3GPP. RAN3 chairman notes [C]/3GPP RAN3#111-eMeeting. 3GPP, 2021
- [9] 3GPP. Support non-terrestrial networks: R2-2100229, Stg 2 Running CR_38.300_NR-NTN-solutions [R]. 2021

Biographies

HAN Jiren (han.jiren@zte.com.cn) received the master degree in wireless communication systems from University of Sheffield, UK in 2016. He is a technology pre-research engineer at the Algorithm Department, ZTE Corporation. His research focuses on next generation radio access network.

GAO Yin received the master degree in circuit and system from Xidian University, China in 2005. Since 2005, she has been with the research center of ZTE Corporation and is engaged in the study of 4G/5G technology. She has authored about hundreds of proposals for 3GPP meetings and journal papers in wireless communications. From June 2021, she has been elected as the 3GPP RAN3 Chairman.

ZTE Communications Guidelines for Authors

Remit of Journal

ZTE Communications publishes original theoretical papers, research findings, and surveys on a broad range of communications topics, including communications and information system design, optical fiber and electro-optical engineering, microwave technology, radio wave propagation, antenna engineering, electromagnetics, signal and image processing, and power engineering. The journal is designed to be an integrated forum for university academics and industry researchers from around the world.

Manuscript Preparation

Manuscripts must be typed in English and submitted electronically in MS Word (or compatible) format. The word length is approximately 3 000 to 8 000, and no more than 8 figures or tables should be included. Authors are requested to submit mathematical material and graphics in an editable format.

Abstract and Keywords

Each manuscript must include an abstract of approximately 150 words written as a single paragraph. The abstract should not include mathematics or references and should not be repeated verbatim in the introduction. The abstract should be a self-contained overview of the aims, methods, experimental results, and significance of research outlined in the paper. Five carefully chosen keywords must be provided with the abstract.

References

Manuscripts must be referenced at a level that conforms to international academic standards. All references must be numbered sequentially in-text and listed in corresponding order at the end of the paper. References that are not cited in-text should not be included in the reference list. References must be complete and formatted according to *ZTE Communications* Editorial Style. A minimum of 10 references should be provided. Footnotes should be avoided or kept to a minimum.

Copyright and Declaration

Authors are responsible for obtaining permission to reproduce any material for which they do not hold copyright. Permission to reproduce any part of this publication for commercial use must be obtained in advance from the editorial office of *ZTE Communications*. Authors agree that a) the manuscript is a product of research conducted by themselves and the stated co-authors; b) the manuscript has not been published elsewhere in its submitted form; c) the manuscript is not currently being considered for publication elsewhere. If the paper is an adaptation of a speech or presentation, acknowledgement of this is required within the paper. The number of co-authors should not exceed five.

Content and Structure

ZTE Communications seeks to publish original content that may build on existing literature in any field of communications. Authors should not dedicate a disproportionate amount of a paper to fundamental background, historical overviews, or chronologies that may be sufficiently dealt with by references. Authors are also requested to avoid the overuse of bullet points when structuring papers. The conclusion should include a commentary on the significance/future implications of the research as well as an overview of the material presented.

Peer Review and Editing

All manuscripts will be subject to a two-stage anonymous peer review as well as copyediting, and formatting. Authors may be asked to revise parts of a manuscript prior to publication.

Biographical Information

All authors are requested to provide a brief biography (approx. 100 words) that includes email address, educational background, career experience, research interests, awards, and publications.

Acknowledgements and Funding

A manuscript based on funded research must clearly state the program name, funding body, and grant number. Individuals who contributed to the manuscript should be acknowledged in a brief statement.

Address for Submission

<http://mc03.manuscriptcentral.com/ztecom>

ZTE COMMUNICATIONS

中兴通讯技术(英文版)

ZTE Communications has been indexed in the following databases:

- Abstract Journal
- Cambridge Scientific Abstracts (CSA)
- China Science and Technology Journal Database
- Chinese Journal Fulltext Databases
- Index of Copernicus
- Ulrich's Periodicals Directory
- Wanfang Data
- WJCI 2021

Industry Consultants:

DUAN Xiangyang, GAO Yin, HU Liujun, LIU Xinyang,
LU Ping, SHI Weiqiang, WANG Huitao, XIONG Xiankui,
ZHU Fang, ZHU Xiaoguang

ZTE COMMUNICATIONS

Vol. 20 Supplement 1 (Issue 77)

Quarterly

First English Issue Published in 2003

Supervised by:

Anhui Publishing Group

Sponsored by:

Time Publishing and Media Co., Ltd.

Shenzhen Guangyu Aerospace Industry Co., Ltd.

Published by:

Anhui Science & Technology Publishing House

Edited and Circulated (Home and Abroad) by:

Magazine House of ZTE Communications

Staff Members:

General Editor: WANG Xiyu

Editor-in-Chief: JIANG Xianjun

Executive Editor-in-Chief: HUANG Xinming

Editorial Director: LU Dan

Editor-in-Charge: ZHU Li

Editors: REN Xixi, LU Dan, XU Ye, YANG Guangxi

Producer: XU Ying

Circulation Executive: WANG Pingping

Assistant: WANG Kun

Editorial Correspondence:

Add: 12F Kaixuan Building, 329 Jinzhai Road,
Hefei 230061, P. R. China

Tel: +86-551-65533356

Email: magazine@zte.com.cn

Website: <http://zte.magtechjournal.com>

Annual Subscription: RMB 80

Printed by:

Hefei Tiancai Color Printing Company

Publication Date: January 30, 2022

China Standard Serial Number: ISSN 1673-5188
CN 34-1294/TN

Publication Approval Number: 341294202201